



GIA imaging of 3D mantle viscosity based on paleo sea-level observations - Part I: Sensitivity kernels for an Earth with laterally varying viscosity

Journal:	<i>Geophysical Journal International</i>
Manuscript ID	GJI-22-0895
Manuscript Type:	Research Paper
Date Submitted by the Author:	27-Oct-2022
Complete List of Authors:	Lloyd, Andrew; Columbia University Lamont-Doherty Earth Observatory, Crawford, Ophelia; University of Cambridge, Department of Earth Sciences Al-Attar, David; University of Cambridge, Earth Sciences Austermann, Jacqueline; Columbia University Lamont-Doherty Earth Observatory Hoggard, Mark; Australian National University, Research School of Earth Sciences Richards, Frederick; Imperial College London, Department of Earth Science and Engineering Syvret, Frank; University of Cambridge, Department of Earth Sciences
Additional Keywords:	
Keywords:	Sea level change < GEODESY and GRAVITY, Rheology: mantle < TECTONOPHYSICS, Inverse theory < GEOPHYSICAL METHODS

SCHOLARONE™
Manuscripts

GIA imaging of 3D mantle viscosity based on paleo sea-level observations - Part I: Sensitivity kernels for an Earth with laterally varying viscosity

Andrew J. Lloyd^{*,1}, Ophelia Crawford², David Al-Attar², Jacqueline Austermann¹, Mark J. Hoggard³,
Fred D. Richards⁴, Frank Syvret²

- 16 1. Lamont Doherty Earth Observatory, Columbia University, Palisades, NY 10964, USA.
- 17 2. Bullard Laboratories, Department of Earth Sciences, University of Cambridge, Madingley Road, Cam-
18 bridge CB3 0EZ, UK.
- 19 3. Research School of Earth Sciences, Australia National University, Acton, ACT 0200, Australia.
- 20 4. Department of Earth Science and Engineering, Imperial College London, London SW7 2AZ, UK.

25 *andrewl@ldeo.columbia.edu

30 Summary

32 A key initial step in geophysical imaging is to devise an effective means of mapping the sensitivity of any
33 observation to the model parameters, that is to compute its Fréchet derivatives or sensitivity kernel. In
34 the absence of any simplifying assumptions and when faced with a large number of free parameters, the
35 adjoint method can be an effective and efficient approach to calculating Fréchet derivatives that requires just
36 two numerical simulations. In the Glacial Isostatic Adjustment (GIA) problem, these consist of a forward
37 simulation driven by changes in ice mass and an adjoint simulation driven by *fictitious* loads that are applied at
38 the observation sites. The theoretical requirements for this approach have been developed over the last decade.
39 Here, we generate the final pieces needed to image 3D mantle viscosity based on a dataset of paleo sea-level
40 observations. Developments include the calculation of viscosity Fréchet derivatives (i.e., sensitivity kernels)
41 for relative sea-level observations, a modification to the numerical implementation of the forward and adjoint
42 problem that permits application to 3D viscosity structure, and a recalibration of initial sea level that ensures the
43 forward simulation honors present-day topography. In the process of addressing these items, we build intuition
44 concerning how absolute sea-level and relative sea-level observations sense Earth's viscosity structure and the
45 physical processes involved. We discuss examples for the near field (Andenes, Norway), far field (Seychelles),
46 and edge of the forebulge of the Laurentide ice sheet (Barbados). Examination of these kernels: (1) reveals
47 why 1D estimates of mantle viscosity from far-field relative sea-level observations can be biased; (2) hints at
48 why an appropriate differential relative sea-level observation can provided a better constraint on local mantle
49 viscosity; and (3) demonstrates that sea-level observations have non-negligible 3D sensitivity to deep mantle
50 viscosity structure, which is counter to the intuition gained from 1D radial viscosity Fréchet derivatives. Finally,
51 we explore the influence of lateral variations in viscosity on relative sea-level observations in the Amundsen
52 Sea Embayment and at Barbados. These predictions are based on a new global 3D viscosity inference derived
53 from the shear-wave speeds of GLAD-M25 and an inverse calibration scheme that ensures compatibility with
54 certain fundamental geophysical observations. Use of the 3D viscosity inference leads to: (1) generally greater
55

1
2
3 25 complexity within the kernel; (2) an increase in sensitivity and presence of shorter length scale features within
4 26 lower viscosity regions; (3) a zeroing out of the sensitivity kernel within high-viscosity regions where elastic
5 27 deformation dominates; and (4) a shifting of sensitivity at a given depth to distal regions of weaker viscosity.
6 28 The tools and intuition built here provide the necessary framework to explore inversions for 3D mantle viscosity
7 29 based on paleo sea-level data.

8
9
10 30 **Keywords:**

11 31 Glacial Isostatic Adjustment, Paleo Sea level, 3D Mantle Viscosity Inference, Sensitivity Kernels, Adjoint
12 32 Method

1 2 33 1 Introduction 3 4 5

6 34 Geophysicist's have gone to great lengths to image Earth's interior using observations of seismic wave propa-
7 35 gation (e.g., Nolet, 2008; Tromp, 2019), gravitational (e.g., Sjöberg & Bagherbandi, 2017) and electromagnetic
8 36 (e.g., Tikhonov, 1950; Chave & Jones, 2012) fields, as well as its response to deformation by both internal
9 37 (e.g., Pollitz, 2001; Forte & Mitrovica, 1996) and external forces (e.g., moon and sun; Nakada & ichiro Karato,
10 38 2012; Lau *et al.*, 2017). In doing so, they provide constraints on physical parameters that fundamentally
11 39 control the behavior of our planet across a range of spatial and temporal scales. With advances in imaging
12 40 techniques, computational resources, and observational data sets, imaging of these parameters has evolved from
13 41 simple, spherically symmetric 1D models into increasingly complex 3D models. Despite more than a century
14 42 of research, imaging of Earth's viscous structure has been restricted to 1D radial models (e.g., Haskell, 1935;
15 43 Mitrovica, 1996; Lau *et al.*, 2016; Argus *et al.*, 2021). One of the best geophysical processes to exploit for
16 44 imaging mantle viscosity is Glacial Isostatic Adjustment (GIA), which is the viscoelastic deformation of the
17 45 solid Earth as well as changes to its gravitational field and rotational axis in response to the evolving surface
18 46 loads of the ice sheets and oceans. This process is most reliably constrained by observations of paleo sea level,
19 47 but the use of these observations to image 3D mantle viscosity has been hindered by a sparsity of data coverage,
20 48 a lack of appropriate standardisation procedures (Khan *et al.*, 2019), and perhaps most importantly, the absence
21 49 of an efficient inversion scheme.
22
23

24 50 The influence of 3D viscosity structure on GIA has been recognized for the past few decades (e.g., Gasperini
25 51 *et al.*, 1990; Whitehouse, 2018), but has seen an accelerated interest in recent years driven by a desire to better
26 52 understand the interactions between the solid Earth and the cryosphere (e.g., Kaufmann *et al.*, 2005; Gomez
27 53 *et al.*, 2015; Whitehouse *et al.*, 2019) or more broadly the hydrosphere (e.g., Wu, 2006; Austermann *et al.*,
28 54 2013; Li *et al.*, 2020; Bagge *et al.*, 2021). The degree of viscosity heterogeneity imaged by regional GIA
29 55 studies (e.g., Nield *et al.*, 2014, 2016; Barletta *et al.*, 2018; Austermann *et al.*, 2020) and inferred from seismic
30 56 tomography (e.g., Ivins *et al.*, 2021; Austermann *et al.*, 2021) suggests that Earth's viscous response occurs
31 57 over years to thousands of years and at length scales of tens to many thousands of kilometers. Numerical
32 58 simulations show that lateral viscosity variations can give rise to complex horizontal patterns of deformation
33 59 that cannot be reproduced by a spherically symmetric viscosity model unless the ice history is substantially
34 60 modified (Kaufmann *et al.*, 2005). Likewise, the 3D viscosity structure of subduction zones can influence
35 61 local relative sea level and profoundly impact its interpretation (Austermann *et al.*, 2013). These examples,
36
37
38
39
40
41
42
43
44
45
46
47
48
49
50
51
52
53
54
55
56
57
58
59
60

1
2
3 62 demonstrate the importance of accounting for lateral viscosity variations for improving the accuracy of GIA
4 63 model predictions, which will in turn improve estimates of surface to near-surface mass change using satellite
5 64 gravimetry (e.g., Groh *et al.*, 2012; van der Wal *et al.*, 2015; Barletta *et al.*, 2018), models of ice sheet dynamics
6 65 (e.g., Gomez *et al.*, 2015, 2018), and models of past to future sea level change (e.g., Gomez *et al.*, 2018; Pan
7 66 *et al.*, 2021).

8
9
10 67 A number of avenues exist to constrain Earth's 3D viscosity structure and can be broadly divided into those
11 68 that *infer* viscosity based on other physical parameters and those that *image* viscosity directly from observations.
12
13 69 Here we focus on the former and address the latter in Lloyd *et al.* (in prep). Inference-based approaches primarily
14
15 70 use seismic tomography models of shear-wave speed and convert them into temperature and viscosity using
16
17 71 constitutive flow laws and material parameters derived from laboratory experiments (e.g. Priestley & McKenzie,
18
19 72 2013; Yamauchi & Takei, 2016; Richards *et al.*, 2020; Austermann *et al.*, 2021; Ivins *et al.*, 2021). Although
20
21 73 such approaches benefit from the high resolution and enhanced spatial coverage of seismic tomography, they
22
23 74 also inherit the assumptions and uncertainties associated with the tomographic inversion and flow laws, leading
24
25 75 to a wide range of plausible mappings (Ivins *et al.*, 2021). For example, tomographic images depend upon
26
27 76 the choice of seismic observations, model parameterization, regularization (e.g., damping and smoothing),
28
29 77 resolution, and any simplifying assumptions, such as how attenuation is or is not included. Accounting for these
30
31 78 effects is nontrivial and, in many instances, impractical. The calibration scheme of Richards *et al.* (2020) seeks
32
33 79 to reduce these issues by using only those combinations of material parameters that yield models that satisfy
34
35 80 a number of well-known, independent solid Earth observations (e.g., thermal structure of oceanic lithosphere,
36
37 81 average adiabatic gradient within the convecting mantle, etc.). Other approaches are instead calibrated by fitting
38
39 82 estimates of upper mantle viscosity from regional GIA studies (e.g., Approach 1 and 2 in Ivins *et al.*, 2021) or
40
41 83 direct observations, such as solid Earth deformation, sea-level change, and satellite gravimetry (e.g., Approach
42
43 84 3 in Ivins *et al.*, 2021). Yet in all instances, assumptions must be made about the physical state of the mantle and
44
45 85 hence the origin of the seismic anomalies (e.g., temperature, composition, fluids, melt, grain size, etc.) as well
46
47 86 as the active deformation mechanisms (e.g., dislocation creep, diffusion creep, grain boundary sliding, etc.).

48
49 87 Despite great advancements in inference techniques in recent years, there is no guarantee that the resulting
50
51 88 3D viscosity structures will provide a better fit to GIA observations and indeed it may be significantly worse
52
53 89 (e.g., Bagge *et al.*, 2021). One explanation for this behavior are shortcomings of the 3D viscosity inference,
54
55 90 which may arise from deficiencies in the seismic tomography or other geophysical constraints as well as the
56
57 91 approach and assumptions used in making the inference, as discussed above. An alternative explanation is that

1
2
3 92 ice history models are *tuned* assuming Earth's viscosity structure varies with depth along (e.g., Peltier *et al.*,
4 93 2015; Caron *et al.*, 2017). As a result these models may overfit the GIA observations and map data misfit due
5 94 to solid Earth structure and rheology into ice history. Given these issues and the strong trade-off of these key
6 95 GIA parameters, one can expect deficiencies in both.

7
8
9
10 96 Rectifying these deficiencies using forward modeling or through search algorithms (e.g., Monte Carlo,
11 97 Bayesian Inference) common to GIA studies (e.g., Nield *et al.*, 2014; Barletta *et al.*, 2018; Lau *et al.*, 2016;
12 98 Caron *et al.*, 2017) is computationally impractical when adopting a 3D viscosity model, as they critically depend
13 99 on quickly solving the forward GIA problem many thousands of times. An alternative approach is to directly
14 100 invert observations for the desired model parameters (e.g., mantle viscosity) in order to minimize a suitable
15 101 misfit function. Doing so requires an efficient approach for determining an observation's 3D sensitivity to a
16 102 model parameter (i.e., its Fréchet derivative), which was lacking until the application of the adjoint method to
17 103 the GIA problem by Al-Attar & Tromp (2013) and Crawford *et al.* (2018). Through their work and others (e.g.
18 104 Kim *et al.*, 2022), it is becoming increasingly clear that observations that were previously assumed to capture the
19 105 global average viscosity of the mantle and used to image 1D profiles (e.g., Mitrovica & Peltier, 1993; Mitrovica
20 106 & Forte, 2004; Lau *et al.*, 2016) actually have spatially biased sensitivity, as suggested by Lau *et al.* (2018). For
21 107 example, the 3D viscosity Fréchet derivatives for the rate of change of the degree 2 zonal harmonic of Earth's
22 108 geopotential (J_2) shows that this observation is predominantly only sensitive to deep mantle structure in the
23 109 northern hemisphere (Kim *et al.*, 2022).

24
25 110 Building on the work of Al-Attar & Tromp (2013) and Crawford *et al.* (2018), we focus on addressing
26 111 the longstanding but fundamental question: How do paleo sea-level observations sense solid-Earth structure?
27
28 112 Over the course of this manuscript and its companion paper (Lloyd *et al.*, in prep), we lay the foundation for
29 113 imaging 3D mantle viscosity directly from GIA observations. In doing so, we will draw parallels to and borrow
30 114 from seismic tomography. We begin by reviewing the application of the adjoint method to the GIA problem,
31 115 presenting an extension of this work that allows for the inclusion of lateral viscosity variations, and discussing
32 116 the influence of 3D viscosity structure on the spatial and temporal behavior of viscosity sensitivity kernels for
33 117 sea-level measurements. We demonstrate the calculation of sensitivity kernels for an Earth with 3D viscosity
34 118 structure using an initial inference of steady-state 3D mantle viscosity that we generate by applying the approach
35 119 of Richards *et al.* (2020) and Austermann *et al.* (2021) to the global seismic tomography model GLAD-M25
36 120 (Bozdağ *et al.*, 2016; Lei *et al.*, 2020). We also present a recalibration of initial sea level using the adjoint method
37 121 that ensures that final sea level matches a target observation regardless of changes to the model parameters.

1
2
3 122 Finally, the methods, results, and intuition built herein are used to inform a companion paper (Lloyd *et al.*, in
4
5 123 prep) that explores strategies for imaging 3D mantle viscosity with synthetic paleo sea-level data.
6
7

8 124 **2 Review of the Rate Formulation of the Forward and Adjoint GIA Problem** 9

10
11 125 The first step towards data-driven inversions of GIA observations is to map the sensitivity of an observation
12
13 126 to the n -parameter model space, that is to calculate its Fréchet derivative with respect to the model parameter.
14
15 127 A simple, albeit brute-force, approach to determining this derivative is the finite-difference method. In this
16
17 128 approach, $n + 1$ individual GIA simulations are required to compute a single Fréchet derivative: one simulation
18
19 129 for the unperturbed problem and n additional simulations that perturb each of the model parameters in turn (e.g.,
20
21 130 Mitrovica & Peltier, 1991; Paulson *et al.*, 2005; Wu, 2006). Given that n is large for GIA simulations containing
22
23 131 3D viscosity structure, that these simulations are computationally expensive (e.g., Latychev *et al.*, 2005), and
24
25 132 that a formal inversion requires Fréchet derivatives to be computed for many thousands of observations, it is
26
27 133 clear that such an approach is impractical. Instead we follow the lead of seismic tomography (e.g., Tromp *et al.*,
28
29 134 2004; Fichtner *et al.*, 2006) and use the adjoint method to calculate Fréchet derivatives with just two numerical
30
31 135 simulations: a forward simulation driven by the ice history and a time reversed adjoint simulation driven by
32
33 136 *fictitious* loads applied at the observation sites and times (Al-Attar & Tromp, 2013; Crawford *et al.*, 2018).

34
35 137 In the rest of this section, we review the formulation of the forward and adjoint GIA problems and their key
36
37 138 assumptions. Although Al-Attar & Tromp (2013) and Crawford *et al.* (2018) only applied this formulation to
38
39 139 a 1D radial viscosity structure, we note that it is equally valid for any 3D viscosity structure. The difference
40
41 140 between the two cases is manifested in its numerical implementation and is discussed in Section 3.2. For a full
42
43 141 account of the derivation and numerical implementation of the forward and adjoint GIA equations, we refer the
44
45 142 reader to Al-Attar & Tromp (2013) and Crawford *et al.* (2018). Here, we focus on only those aspects that are
46
47 143 relevant for understanding the calculation of viscosity Fréchet derivatives (hereafter, *sensitivity kernels*), the
48
49 144 numerical implementation of laterally varying viscosity, and the ultimate goal of imaging 3D mantle viscosity.
50

51 145 **2.1 The Forward GIA Problem** 52

53
54 146 The approach taken here to solve the GIA problem differs from methods that rely on iteratively solving the
55
56 147 sea-level equation (e.g., Mitrovica & Milne, 2003; Kendall *et al.*, 2005). Instead, Al-Attar & Tromp (2013)
57
58 148 and Crawford *et al.* (2018) derive coupled evolution equations that embody the same physics as the sea-level
59
60

equation, but can be solved numerically with an explicit time-stepping scheme and are ideally suited for the adjoint method. Like other solutions of the GIA problem, the solid Earth is assumed to undergo quasi-static deformation, to be self-gravitating, and to be initially at rest and in hydrostatic equilibrium. Previously, it has been assumed to be spherical, isotropic, compressible, and composed of an elastic inner core, an inviscid fluid outer core, a viscoelastic mantle, and an elastic lithosphere. In our simulations, however, we allow the mantle and crust to deform viscoelastically and allow the lithosphere to be defined by the extent of high viscosity regions and the characteristics of the load changes (Section 3.4). In addition, we assume that deformation in viscoelastic regions is governed by a Maxwell rheology and neglect bulk viscosity, which are both common assumptions in GIA studies (Whitehouse, 2018), although it is worth noting that transient linear and nonlinear rheologies can also be implemented (as discussed in Crawford *et al.*, 2016).

Crawford *et al.* (2018) extended the work of Al-Attar & Tromp (2013) to include gravitationally self-consistent sea-level change with shoreline migration. This extension is achieved by assuming that the oceans and ice sheets are sufficiently thin that they can be represented as surface loads. Strictly speaking, the inclusion of ice sheets, non-global oceans, and continents violates the model's initial condition of hydrostatic equilibrium. Nevertheless, the expected departure from a hydrostatic pre-stressed field due to realistic lateral heterogeneity will be small, and so additional terms associated with the deviatoric pre-stress are neglected (Dahlen & Tromp, 1999). It is also assumed that the oceans remain in hydrostatic equilibrium and are interconnected, thus requiring their surface to lie along the same gravitational equipotential. Under the assumption that water mass is conserved between the oceans and ice sheets, the rate of sea-level change is

$$\dot{SL} = -\frac{1}{g}(\dot{\mathbf{u}} \cdot \nabla \Phi + \dot{\phi}) + \frac{1}{gA} \int_{\partial M} C(\dot{\mathbf{u}} \cdot \nabla \Phi + \dot{\phi}) dS - \frac{\rho_i}{\rho_w A} \int_{\partial M} (1 - C)\dot{I} dS, \quad (1)$$

where dots are used to denote time derivatives and the variables are defined in Table 1. The reduced weak-form of the forward GIA problem with gravitationally self-consistent sea-level change and shoreline migration is

$$\begin{aligned} \mathcal{A}(\dot{\mathbf{u}}, \dot{\phi} | \mathbf{u}', \phi') - \frac{\rho_w}{g} \int_{\partial M} \left[\dot{\mathbf{u}} \cdot \nabla \Phi + \dot{\phi} - \frac{1}{A} \int_{\partial M} C(\dot{\mathbf{u}} \cdot \nabla \Phi + \dot{\phi}) dS \right] C(\mathbf{u}' \cdot \nabla \Phi + \phi') dS \\ = \int_{M_S} 2\mu_0 \left[\dot{\mathbf{m}} : \mathbf{m}' + \frac{1}{\tau} (\mathbf{d} - \mathbf{m}) : (\mathbf{d}' - \mathbf{m}') \right] dV \\ - \rho_i \int_{\partial M} (1 - C)\dot{I}_c \left[\mathbf{u}' \cdot \nabla \Phi + \phi' - \frac{1}{A} \int_{\partial M} C(\mathbf{u}' \cdot \nabla \Phi + \phi') dS \right] dS. \quad (2) \end{aligned}$$

Table 1: Variables used in the forward and adjoint formalism.

Variable	Meaning	Variable	Meaning
Mathematical Symbols, Superscripts, Subscripts			
$\dot{*}$	Time derivative	∇	Gradient
$*'$	Test function	$*^\dagger$	Adjoint variable
\cdot	Dot product	:	Contraction
M_S	Union of the solid regions	dV	Volume integral
∂M	Surface	dS	Surface integral
Time Parameters			
t	Forward time	t^\dagger	Adjoint time ($t^\dagger = t_1 - t + t_0$)
t_0	Initial time (e.g., 26 ka)	t_1	Final time (e.g., 0 ka)
Ice-Sheet Parameters			
I	Ice thickness	ρ_i	Density of ice
I_0	Initial ice thickness	I_c	Current ice thickness
Sea-Level Parameters			
SL	Sea level	ρ_w	Density of water
C	Ocean mask	A	Area of Ocean
SL_0	Initial sea level		
Solid-Earth Parameters			
\mathbf{u}	Displacement	ϕ	Gravitational potential perturbation
Φ	Gravitational potential of the reference model	g	Magnitude of gravitational acceleration
μ_0	Unrelaxed shear modulus	\mathcal{A}	The elastodynamics of the system
η	Viscosity	τ	<i>Maxwell relaxation time</i>
\mathbf{m}	<i>Internal memory variable</i>	\mathbf{d}	Deviatoric strain tensor
τ	Deviatoric Stress		
Select Adjoint Parameters			
$\dot{h}_{SL,\mathbf{u},\phi}$	Adjoint loads, sea level, displacement, gravitation perturbation	K_{η,SL_0}	Sensitivity kernel, viscosity, initial sea level

Within this equation, \mathbf{m} is an *internal variable* used to simulate a Maxwell rheology, with the evolution of this term governed by

$$\dot{\mathbf{m}} + \frac{1}{\tau}(\mathbf{m} - \mathbf{d}) = \mathbf{0}. \quad (3)$$

Here the *internal variable* \mathbf{m} contains the memory of past deformation, in which the duration of this memory is controlled by the *Maxwell relaxation time*, τ , and is by extension related to viscosity, η . The derivation of these equations can be found in Al-Attar & Tromp (2013) and Crawford *et al.* (2018). We now focus on a few

1
2
3 173 key aspects of eqs. (1) and (2).

4
5 174 First, and foremost, eqs. (1) and (2) are a non-iterative formulation for gravitationally self-consistent sea-
6 level change with shoreline migration. The non-linearity of shoreline migration, due to the interplay of ocean
7 height and solid Earth deformation, is captured through dependence of the ocean function, C , on the ocean
8 height, SL , and the ice thickness, I . However, this rate formulation does not yet include rotation, which is the
9 subject of ongoing work. It is our expectation that rotation will have a minor and long wavelength effect on the
10 viscosity sensitivity kernels because it is composed primarily of a spherical harmonic degree-two and order-one
11 signal (e.g., Han & Wahr, 1989; Milne & Mitrovica, 1998). In addition, rotation is not required to develop
12 an adjoint based recalibration scheme for initial sea level nor is it required to explore inversion strategies for
13 imaging 3D mantle viscosity (Lloyd *et al.*, in prep).

14
15 183 Equation (2) forms the core of the forward GIA problem and consists of the elastodynamic terms within
16 $\mathcal{A}(\dot{\mathbf{u}}, \dot{\phi} | \mathbf{u}', \phi')$, the surface load changes due to the ice sheets and ocean that manifest within the second and
17 fourth integral terms, and the viscous response of the system within the third integral term. As written, all terms
18 containing the unknown deformation field components, $\{\dot{\mathbf{u}}, \dot{\phi}\}$, are on the left-hand side and the right-hand side
19 contains the integral terms that are readily calculated or known. Because these terms are linear with respect
20 to $\dot{\mathbf{u}}$ and $\dot{\phi}$, eq. (2) has the schematic form $\mathbf{Ax} = \mathbf{b}$, which means that the time-derivatives of the deformation
21 fields can be obtained by solving a set of linear equations. Finally, time derivatives of sea level and the *internal*
22 variables can be directly calculated from their stated evolution equations, and in this manner the whole system
23 can be time-stepped.

39 192 2.2 The Adjoint GIA Problem

40
41 193 Similar to the previous subsection, we will not review the full derivation of the adjoint GIA equations presented
42 in Crawford *et al.* (2018). Instead, we will go over the essential ideas in their derivation in a schematic manner.
43
44 195 Following this, we will state the form of the adjoint equations and briefly discuss their structure as well as
45 explain how the relevant sensitivity kernels are derived.

46
47 197 Let the vector, U , denote the state of the physical system and a vector, P the underlying model parameters.
48
49 198 The state vector, U is defined over an interval $t \in [t_0, t_1]$, while P may also have an explicit time-dependence.
50
51 199 We suppose that the forward problem governing the physics is posed as an initial-value problem

52
53
54
55
56
$$\dot{U} - g(U, P) - \mathcal{F} = 0, \quad U(t_0) = U_0, \quad (4)$$

1
2
3 200 where g is a given function of U and P , while \mathcal{F} describes the forcing of the system. This equation is assumed
4
5 201 to have a unique solution, U , for any appropriate value of P .

6
7 202 We also consider a scalar-valued *objective function* $F(U, P)$, which could be an observation (e.g., sea level
8
9 at a specific location and time) or the misfit between predictions and observations. The explicit dependence
10
11 204 of F on the model vector P would, in practice, be due to regularisation terms within a misfit. By solving the
12
13 205 forward problem, the state of the system U becomes an implicit function of the model parameters P , the initial
14
15 206 state U_0 , and the system forcing \mathcal{F} and can be written as $U = \hat{U}(P, U_0, \mathcal{F})$. The corresponding value of F then
16
17 207 depends on P and U_0 alone, and to show this we define the *reduced* functional

$$19 \quad \hat{F}(P, U_0) = F [\hat{U}(P, U_0, \mathcal{F}), P]. \quad (5)$$

22
23 208 Our goal is to differentiate the function, \hat{F} , with respect to the model parameters, P , and initial conditions,
24
25 209 U_0 . This is equivalent to differentiating $F(U, P)$ with respect to P subject to the constraint that U satisfies the
26
27 210 stated initial value problem. To do this, we apply the method of Lagrange multipliers, and so introduce the
28
29 211 *Lagrangian*

$$30 \quad \mathcal{L}(U, U', P, U_0, U'_0) \equiv F(U, P) - \int_{t_0}^{t_1} \langle \dot{U} - g(U, P) - \mathcal{F}, U' \rangle dt - \langle U(t_0) - U_0, U'_0 \rangle. \quad (6)$$

34
35 208 Here $\langle \cdot, \cdot \rangle$ denotes an appropriate inner product for state vectors, U' is a time-dependent Langrange multiplier
36
37 associated with the differential equation for U , and U'_0 is a time-independent Langrange multiplier linked to the
38
39 initial conditions. The Langrange multiplier theorem states that

$$41 \quad D_P \hat{F}(P, U_0) = D_P L(U, U', P, U_0, U'_0), \\ 42 \quad D_{U_0} \hat{F}(P, U_0) = D_{U_0} L(U, U', P, U_0, U'_0), \\ 43 \quad D_{\mathcal{F}} \hat{F}(P, U_0) = D_{\mathcal{F}} L(U, U', P, U_0, U'_0), \quad (7)$$

48
49 212 so long as the following conditions hold:

$$52 \quad D_{U'} L(U, U', P, U_0, U'_0) = 0, \quad D_{U'_0} L(U, U', P, U_0, U'_0) = 0, \quad D_U L(U, U', P, U_0, U'_0) = 0. \quad (8)$$

55
56 213 The first two conditions, stating that L is stationary with respect to the Langrange multipliers, simply require that

1
2
3 214 the state vector solves the given initial value problem. The final condition, however, gives rise to new equations
4 215 that must be satisfied by the Lagrange multipliers. To see this, we note that for any variation δU to the state
5 216 vector we must have
6
7

$$9 \quad \int_{t_0}^{t_1} \langle \delta U, \mathcal{H}' \rangle dt + \int_{t_0}^{t_1} \langle \delta U, \dot{U}' + [D_U g(U, P)]^* U' \rangle dt + \langle \delta U(t_0), U'(t_0) + U'_0 \rangle - \langle \delta U(t_1), U'(t_1) \rangle = 0, \\ 10 \quad (9)$$

11
12
13 217 where the first term involving \mathcal{H}' arises through variation of F with respect to U . Note that to isolate δU within
14 218 the second integral an integration by parts has been performed and the definition of the adjoint (indicated by the
15 219 superscript *) of a linear operator applied. In order for this to hold for arbitrary δU , we see that U' must satisfy
16
17 220 the following differential equation
18
19

$$22 \quad \dot{U}' + [D_U g(U, P)]^* U' + \mathcal{H}' = 0, \quad (10)$$

23
24
25 221 subject to the terminal condition $U'(t_1) = 0$, while we also have $U'_0 = U'(t_0)$.
26
27

28 222 As it is more usual to work with initial value problems, a new variable U^\dagger can be introduced through
29
30

$$31 \quad U^\dagger = \mathbb{T}U', \quad (11)$$

32
33 223 where we have introduced a *time reversal operator* by
34
35

$$36 \quad (\mathbb{T}U)(t) = U(t_1 - t + t_0). \quad (12)$$

37
38 224 Here we note that the terminal condition on U' at t_1 is mapped to an initial condition on U^\dagger at t_0 . Having made
39
40 225 this definition, it is easy to see that U^\dagger satisfies the differential equation
41
42

$$43 \quad \dot{U}^\dagger - \mathbb{T}[D_U g(U, P)]^* \mathbb{T}U^\dagger + \mathcal{H}^\dagger = 0, \quad (13)$$

44
45
46 226 where equivalently $\mathcal{H}^\dagger = \mathbb{T}\mathcal{H}'$. Closer examination of eq. (13) reveals that time is reversed for only
47
48 227 $[D_U g(U, P)]^*$ relative to all other terms, which all share a superscript † . In other words, the first appear-
49
50 228 ance of \mathbb{T} reverses the direction of time, while the second appearance returns the flow of time to its original
51
52 229 direction. Similarly, the initial condition is transformed to $U^\dagger(T_0) = 0$ and we also see that $U^\dagger(t_1) = U'_0$. It is
53
54 230 conventional to call U^\dagger the adjoint state vector, and the above equations the adjoint problem, which are driven
55
56
57

231 by the *fictitious* adjoint forcing, \mathcal{H}^\dagger . Finally, we note that the structure of the adjoint problem (eq. (13)) is very
 232 similar to that of the forward problem (eq (4)) and in such instances solutions for U^\dagger can often be obtained using
 233 the same numerical scheme as the forward problem.

Calculation of the derivative of \hat{F} with respect to P and/or U_0 requires us to solve: (1) the forward problem for the state vector U , and (2) the closely related adjoint problem for the adjoint state U^\dagger , with this latter problem depending on the state vector both through the adjoint force, H^\dagger , and for non-linear forward problems through the linear operator $D_{UG}(U, P)$. Having solved these problems, we can use eq. (7) to obtain the derivative of \hat{F} with respect to P , U_0 , or \mathcal{F} . For example, the first-order change in \hat{F} due to a perturbation δP to the model parameters, δU_0 to the initial conditions, and $\delta \mathcal{F}$ to the system forcing

$$\delta\hat{F} = \langle D_P F(U, P), \delta P \rangle + \int_{t_0}^{t_1} \langle [D_P g(U, P)]^* \mathbb{T} U^\dagger, \delta P \rangle \, dt + \langle U^\dagger(t_1), \delta U_0 \rangle . + \int_{t_0}^{t_1} \langle U^\dagger, \delta \mathcal{F} \rangle \, dt \quad (14)$$

240 Here the first term on the right-hand side typically arises due to regularisation and the second term contains the
 241 interaction of the forward and adjoint simulations. It is notable that the choice of objective function, F , enters
 242 into the adjoint problem only through the adjoint force \mathcal{H}^\dagger . This means that only minimal changes are required
 243 to apply the theory to new types of measurement or misfit.

Following from this mathematical schematic, the appropriate *Lagrangian* for the GIA problem (eq. 78 of Crawford *et al.*, 2018) is given by

$$\begin{aligned} \mathcal{L} = & F - \rho_w g \int_{\partial M} [SL(t_0) - SL_0] SL'(t_0) \, dS + \rho_i g \int_{\partial M} [I(t_0) - I_0] I'(t_0) \, dS \\ & + \int_{t_0}^{t_1} \mathcal{A}(\dot{\mathbf{u}}, \dot{\phi} | \mathbf{u}', \phi') - \int_{M_S} 2\mu_0 \left[\dot{\mathbf{m}} : \mathbf{m}' + \frac{1}{\tau} (\mathbf{d} - \mathbf{m}) : (\mathbf{d}' - \mathbf{m}') \right] \, dV - \rho_w g \int_{\partial M} S L S L' \, dS \\ & - \frac{\rho_w}{g} \int_{\partial M} \left[\dot{\mathbf{u}} \cdot \nabla \Phi + \dot{\phi} - \frac{1}{A} \int_{\partial M} C(\dot{\mathbf{u}} \cdot \nabla \Phi + \dot{\phi}) \, dS \right] [g S L' + C(\mathbf{u}' \cdot \nabla \Phi + \phi')] \, dS - \rho_i g \int_{\partial M} (\dot{I}_c - \dot{I}) I' \, dS \\ & + \rho_i \int_{\partial M} (1 - C) \dot{I}_c \left[\mathbf{u}' \cdot \nabla \Phi + \phi' - \frac{1}{A} \int_{\partial M} [g S L' + C(\mathbf{u}' \cdot \nabla \Phi + \phi')] \, dS \right] \, dS \, dt, \end{aligned} \quad (15)$$

where again variable descriptions can be found in Table 1. Here on the left-hand side the second term imposes the prescribed initial sea level, SL_0 , the third term imposes the prescribed ice thickness, I_0 , and the remainder is the time integrated weak-form of the forward GIA problem. Although all time-dependent variables are evaluated at time t , when working with the *Lagrangian* we will find it useful to introduce the adjoint state variables (eqs. (11) and (12)). In order to more easily recognize their time reversal we define the adjoint time, $t^\dagger = t_1 - t + t_0$, in which the subscripts 0 and 1 are the initial and final time of the forward simulation, respectively.

1
2
3 Crawford *et al.* (2018) derived the adjoint equations for the GIA problem using the third condition of eq (8)
4
5 and the introduction of the adjoint state variables (eqs. (11) and (12)). The resulting adjoint equations are solved
6
7 for unknowns ($SL^\dagger, \dot{\mathbf{u}}^\dagger, \phi^\dagger$), which are comparable the forward equations (eqs. (1) and (2)), and take the form
8

$$9 \quad SL^\dagger = -\frac{\dot{h}_{SL}^\dagger}{\rho_w g} - \frac{\dot{C}^\dagger}{g} \left[\dot{\mathbf{u}}^\dagger \cdot \nabla \Phi + \phi^\dagger - \frac{1}{A^\dagger} \int_{\partial M} [g SL^\dagger + C^\dagger (\dot{\mathbf{u}}^\dagger \cdot \nabla \Phi + \phi^\dagger)] dS \right], \quad (16)$$

12
13 and
14

$$15 \quad \mathcal{A}(\dot{\mathbf{u}}^\dagger, \phi^\dagger | \mathbf{u}', \phi') - \frac{\rho_w}{g} \int_{\partial M} \left[\dot{\mathbf{u}}^\dagger \cdot \nabla \Phi + \phi^\dagger - \frac{1}{A^\dagger} \int_{\partial M} C^\dagger (\dot{\mathbf{u}}^\dagger \cdot \nabla \Phi + \phi^\dagger) dS \right] C^\dagger (\mathbf{u}' \cdot \nabla \Phi + \phi') dS \\ 16 \\ 17 = \int_{M_S} \frac{2\mu_0}{\tau} (\mathbf{d}^\dagger - \mathbf{m}^\dagger) : \mathbf{d}' dV + \int_{\partial M} \left(\dot{\mathbf{h}}_\mathbf{u}^\dagger \cdot \mathbf{u}' + \dot{h}_\phi^\dagger \cdot \phi' \right) dS \\ 18 \\ 19 - \frac{1}{g} \int_{\partial M} \dot{h}_{SL}^\dagger \left[\mathbf{u}' \cdot \nabla \Phi + \phi' - \frac{1}{A^\dagger} \int_{\partial M} C^\dagger (\mathbf{u}' \cdot \nabla \Phi + \phi') dS \right] dS, \quad (17)$$

24
25 respectively. The adjoint internal variable satisfies
26

$$27 \quad \dot{\mathbf{m}}^\dagger + \frac{1}{\tau} (\mathbf{m}^\dagger - \mathbf{d}^\dagger) = \mathbf{0}, \quad (18)$$

32
33 much like the internal variable in the forward problem (eq. (3)).
34

35 A description of these variables are provided in Table 1, but we note that \dot{h}_*^\dagger are the adjoint loads, which
36
37 are equivalent to \mathcal{H}^\dagger in the mathematical schematic. In this work, only \dot{h}_{SL}^\dagger is nonzero because we consider
38
39 only measurements directly related to sea level and not, for example, those for either displacements or gravity.
40
41 In eq. (17), the adjoint sea-level load, \dot{h}_{SL}^\dagger , interacts with the test functions \mathbf{u}' and ϕ' , giving rise to two adjoint
42
43 loads that act on the solid Earth and the gravitational field. Finally, we have similarly written eq. (17) such that
44
45 the unknown components of the deformation field, $\{\dot{\mathbf{u}}^\dagger, \phi^\dagger\}$, are on the left-hand side and the right-hand side
46
47 contains the integral terms that are readily calculated or known.

48 Although the right-hand side of the reduced weak-form of the forward and adjoint equations (eqs. (2) and (17),
49
50 respectively) are different, both are of the form $\mathbf{A}\dot{\mathbf{x}} = \mathbf{b}$. Thus, solutions for the adjoint deformation field rate,
51
52 $\{\dot{\mathbf{u}}^\dagger, \phi^\dagger\}$, can be obtained using the same numerical scheme (Section 3.2), but the elements of \mathbf{b} will be different.
53
54 In so doing, we can readily calculate the adjoint deviatoric stress, similar to the forward problem. Obtaining
55
56 the adjoint sea level is, however, more challenging because eq. (16) is potentially singular and so cannot easily
57
58 be integrated. Crawford *et al.* (2018) presents a method for integrating this equation that circumvents these
59
60

1
2
3 268 singularities by introducing auxiliary variables.
4
5

6 269 As we have shown in the schematic example, by solving the forward equations (eqs. (1) and (2)) and adjoint
7 270 equations (eqs. (16) and (17)) we can use their results to calculate the desired derivative of \hat{F} with respect to
8 271 P (i.e., sensitivity kernel). In order to obtain the form of this derivative we must perturb the *Lagrangian* with
9 272 respect to the desired model parameter. For this study we require expressions for the sensitivity kernels for the
10 273 initial sea level, SL_0 , and viscosity, η .
11
12

13 274 Thus, by varying the Lagrangian in eq. (15) with respect to SL_0 and by introducing the adjoint state variables
14 275 (eq (11) and (12)) we find
15
16

$$17 \quad \langle D_{SL_0} \hat{F}, \delta SL_0 \rangle = \int_{\partial M} K_{SL_0} \delta SL_0 \, dS, \quad (19)$$

19 276 where we have defined the sensitivity kernel for initial sea level to be
20
21

$$23 \quad K_{SL_0} = \rho_w g SL_0^\dagger(t_1^\dagger). \quad (20)$$

25 277 Note that this sensitivity kernel depends only on the adjoint sea level at the final time, t_1^\dagger , of the adjoint simulation.
26
27

28 Likewise, we obtain the viscosity sensitivity kernel by recalling that $\tau = \eta/\mu_0$ for a Newtonian fluid and
29 30 differentiating eq. (15) with respect to η to find
31
32

$$33 \quad \langle D_\eta \hat{F}, \delta \eta \rangle = \int_{t_0}^{t_1} \int_{M_S} \frac{1}{2\eta} \boldsymbol{\tau} : \boldsymbol{\tau}^\dagger \delta \ln \eta \, dV \, dt \quad (21)$$

36 37 278 where $\boldsymbol{\tau} = 2\mu_0(\mathbf{d} - \mathbf{m})$ is the deviatoric stress, $\boldsymbol{\tau}^\dagger$ is the corresponding adjoint field, and $\delta \ln \eta = \frac{\delta \eta}{\eta}$ is a viscosity
38 279 perturbation. Therefore, the sensitivity kernel for a viscosity perturbation is
40
41

$$42 \quad K_{\delta \ln \eta} = \int_{t_0}^{t_1} \frac{1}{2\eta} \boldsymbol{\tau} : \boldsymbol{\tau}^\dagger \, dt. \quad (22)$$

44 45 280 We see that $K_{\delta \ln \eta}$ depends on the interaction of the forward and adjoint deviatoric stresses for the full duration
46 281 of the simulations. Finally, we note that both sensitivity kernel equations (eq. (20) and (22)) are equivalent to
47 282 those determined by Al-Attar & Tromp (2013) and Crawford *et al.* (2018).
48
49
50
51
52
53
54
55
56
57
58
59
60

1
2 **283 3 Methods**
3
4
5

6 Previous viscosity sensitivity kernels for sea-level observations have been presented for a 1D radial viscosity
7 structure and have only considered observations of sea level at a given instant in time (Crawford *et al.*, 2018),
8 which for clarity we refer to these observations as absolute sea level. With regards to the former, Earth's
9 viscosity structure is actually laterally heterogeneous, and this heterogeneity influences solid Earth deformation
10 and by extension the structure of the viscosity sensitivity kernels. Regarding the latter, observations of paleo
11 sea level are always made and reported relative to present-day sea level (e.g., Khan *et al.*, 2019) and thus are
12 in reality a measure of the change in sea level between that time, t_{obs} , and present day, t_p . We note that these
13 relative sea-level observations serve as the building blocks for related paleo sea-level observations including the
14 rate of sea-level change, the timing of sea-level highstands or transgressions (e.g., Nakada & Lambeck, 1989),
15 as well as relative sea-level curves and spatiotemporal fields (e.g., Creel *et al.*, 2022).
16
17

18 Although understanding how these more complex observations sense Earth's viscosity structure is important,
19 we focus here on the more fundamental observations of absolute and relative sea level, their relationship, and
20 the influence of 3D viscosity structure. Thus, we must derive the adjoint loads required to calculate sensitivity
21 kernels for observations of relative sea level (Section 3.1) and incorporate 3D viscosity structure into both the
22 forward and adjoint GIA simulations (Section 3.2). In order to genuinely compare sensitivity kernels based on
23 different combinations of Earth structure and ice history, we also require an approach to ensure the forward GIA
24 simulation converges to the same final sea level regardless of the prescribed physical parameters (Section 3.3).
25
26 Finally, we end Section 3 by providing all the remaining details on the forward and adjoint simulation setup
27 (Section 3.4) including the construction of a new 3D viscosity inference based on the seismic tomography model
28 GLAD-M25 (Section 3.5; Bozdağ *et al.*, 2016; Lei *et al.*, 2020).
29
30

31 **304 3.1 Adjoint Loads for Sea-level Observations**
32
33

34 Thus far, we have not directly addressed the form of the *fictitious* adjoint loads that drive the adjoint GIA
35 simulations and allow us to calculate sensitivity kernels for observations related to the solid Earth, gravity, or
36 sea level. The adjoint loads associated with these observations are obtained by taking the first order perturbation
37 of the scalar-valued function, $F(\mathbf{u}, \phi, SL)$, with respect to the forward variables and can be schematically written
38 as
39
40

$$\delta F = \int_{t_0}^{t_1} \int_{\partial M} (\dot{\mathbf{h}}_{\mathbf{u}} \cdot \delta \mathbf{u} + \dot{h}_\phi \delta \phi + \dot{h}_{SL} \delta SL) \, dS \, dt, \quad (23)$$

1
2
3 where $\dot{\mathbf{h}}_{\mathbf{u}}$, \dot{h}_{ϕ} , and \dot{h}_{SL} are the Fréchet derivative of F with respect to \mathbf{u} , ϕ , and SL , respectively. Note that these
4 Fréchet derivatives are defined to be the time-derivative of some underlying functions, $\mathbf{h}_{\mathbf{u}}$, h_{ϕ} , and h_{SL} . This
5 is done so as to maximize the symmetry between the forward and adjoint problems. We now derive the adjoint
6 loads for observations of absolute sea level and relative sea level. Although the former is presented by Crawford
7 et al. (2018), we begin by rederiving it here in order to demonstrate how these two types of observations are
8 related, but also how they differ in the information they convey.
9

10 Following Crawford et al. (2018) as well as our generalized discussion of the adjoint method (Section 2.2)
11 we can determine the adjoint loads by schematically perturbing the scalar-valued functional F with respect to
12 the state variables U . For an observation of absolute sea level at a given location and time, $SL(\mathbf{x}_{obs}, t_{obs})$, this
13 leads to

$$\delta F = \int_{t_0}^{t_1} \int_{\partial M} \delta SL(\mathbf{x}, t) \delta(\mathbf{x} - \mathbf{x}_{obs}) \delta(t - t_{obs}) dS dt \quad (24)$$

24 where $\delta(\mathbf{x} - \mathbf{x}_{obs})$ is a delta function that is 1 at the observation site and 0 elsewhere. From this we see that the
25 necessary functions defining the Fréchet derivatives are
26

$$\dot{\mathbf{h}}_{\mathbf{u}} = \mathbf{0}, \quad \dot{h}_{\phi} = 0, \quad \dot{h}_{SL} = \delta(\mathbf{x} - \mathbf{x}_{obs}) \delta(t - t_{obs}), \quad (25)$$

32 and this is what is required by eqs. (16) and (17) for an absolute sea-level observation at a given point in space
33 and time.
34

35 We now undertake a similar procedure, but begin with the definition of relative sea level
36

$$RSL(\mathbf{x}_{obs}, t_{obs}) = SL(\mathbf{x}_{obs}, t_{obs}) - SL(\mathbf{x}_{obs}, t_p), \quad (26)$$

43 where t_p is the present-day time, which is synonymous with t_1 in our study. Again, we perturb F with respect
44 to the state variables U , which for a relative sea-level observation results in
45

$$\delta F = \int_{t_0}^{t_1} \int_{\partial M} [\delta SL(\mathbf{x}, t) \delta(\mathbf{x} - \mathbf{x}_{obs}) \delta(t - t_{obs}) - \delta SL(\mathbf{x}, t) \delta(\mathbf{x} - \mathbf{x}_{obs}) \delta(t - t_p)] dS dt \quad (27)$$

51 From this it readily follows that the necessary functions are now
52

$$\dot{\mathbf{h}}_{\mathbf{u}} = \mathbf{0}, \quad \dot{h}_{\phi} = 0, \quad \dot{h}_{SL} = \delta(\mathbf{x} - \mathbf{x}_{obs}) \delta(t - t_{obs}) - \delta(\mathbf{x} - \mathbf{x}_{obs}) \delta(t - t_p). \quad (28)$$

1
2
3 Examining eq. (28), we see that it is composed of two *fictitious* loads of equal magnitude and opposite signs,
4 which are applied at times t_{obs} and t_p . Moreover, by comparing eqs. (28) and (25), we see that the former
5 fundamentally consists of two absolute sea-level adjoint loads, which implies that the sensitivity kernels for
6 relative sea-level observations can be obtained in one of two ways: (1) by using both adjoint loads in a single
7 adjoint simulation, or (2) by using each adjoint load in an independent adjoint simulation and then taking the
8 difference of the resulting absolute sea-level sensitivity kernels (i.e., $K_{SL}(\mathbf{x}_{obs}, t_{obs}) - K_{SL}(\mathbf{x}_{obs}, t_p)$). This
9 property of superposition, which is routinely exploited in seismic tomography (e.g., Tape *et al.*, 2007; Bozdağ
10 *et al.*, 2016; Lloyd *et al.*, 2020; Lei *et al.*, 2020), is of critical importance and will be exploited in our companion
11 paper to image 3D viscosity using paleo sea-level observations.
12
13
14
15
16
17
18
19
20
21
22
23
24
25
26
27
28
29
30
31
32
33
34
35
36
37
38
39
40
41
42
43
44
45
46
47
48
49
50
51
52
53
54
55
56
57
58
59
60

337 3.2 Numerical Implementation of 3D Viscosity

338 The introduction of lateral viscosity heterogeneity adds some complexity to solving the forward and adjoint
339 GIA equations using a pseudo-spectral method, which was previously identified and solved by Martinec (2000).
340 This complexity occurs in the first integral term on the right-hand side of eqs. (2) and (17), which describes
341 the viscous response of the system. Prior to addressing this complexity, we briefly outline our numerical
342 implementation as it provides full context for the required modification.

343 As in Crawford *et al.* (2018), we numerically solve eqs. (2) and (17) by representing scalar, vector, and tensor
344 fields within and on the solid Earth using generalized spherical harmonics to capture their angular dependence
345 (Gelfand & Shapiro, 1956; Burridge, 1969), while their depth dependence is described by a 1D radial mesh
346 of spectral-elements that each consist of five Gauss-Lobatto-Legendre interpolation points. Using these basis
347 functions, eqs. (2) and (17) both decouple into spheroidal and toroidal subsystems, in which the latter are not
348 excited by radial surface loads for a laterally homogeneous Earth. However, unlike in the viscoelastic loading
349 problem of Al-Attar & Tromp (2013), the two spherical harmonic components (radial and consoildal) and the
350 gravitational perturbation do not decouple for each spherical harmonic degree- l and order- m . This is because the
351 ocean load (i.e., the second integral term on the left-hand side of eqs. (2) and (17)) depends on the entire $\dot{\mathbf{u}}$ and
352 $\dot{\phi}$ fields. Therefore, instead of solving the simple form $\mathbf{A}_l \dot{\mathbf{x}}_{lm} = \mathbf{b}_{lm}$ for each l , we must solve the more complex
353 form $\mathbf{A}_l \dot{\mathbf{x}}_{lm} + \mathbf{g}_{lm}(\dot{\mathbf{x}}) = \mathbf{b}_{lm}$, which requires an iterative solution (see Appendix B of Crawford *et al.*, 2018). We
354 assume the solution for the deformation field, $\{\dot{\mathbf{u}}, \dot{\phi}\}$, has converged when the difference in subsequent solutions
355 is less than 1.0% of the difference between the final and initial solution. Finally, for completeness, recall that the
356 sea-level rate, $\dot{S}L$, is obtained directly from eq. (1) and the adjoint sea-level rate, $\dot{S}L^\dagger$, is obtained from eq. (16)

1
2
3 357 following a change of variables, which is described in Crawford *et al.* (2018).
4
5

6 358 With this context, we now return to the matter of implementing lateral viscosity heterogeneity within the
7 forward and adjoint GIA simulations, which is also discussed in Crawford (2019). Here, we focus on the viscous
8 response as it appears in the reduced weak-form of the forward GIA problem, eq. (2), but note that a similar
9 integral term also appears in the adjoint GIA problem, eq. (17). These integral terms are identical up to the
10 exchange of the forward and adjoint variables ($\{\mathbf{m}, \mathbf{d}\} \leftrightarrow \{\mathbf{m}^\dagger, \mathbf{d}^\dagger\}$), and thus, are evaluated in an identical
11 manner. When working with a 1D radial viscosity structure we are required to evaluate
12
13 363

$$\int_0^{R_\oplus} \int_{\partial M_r} 2\mu(r) \left[\dot{\mathbf{m}} : \mathbf{m}' + \frac{1}{\tau(r)} (\mathbf{d} - \mathbf{m}) : (\mathbf{d}' - \mathbf{m}') \right] dS dr = \int_0^{R_\oplus} \frac{2\mu(r)}{\tau(r)} \int_{\partial M_r} (\mathbf{d} - \mathbf{m}) : \mathbf{d}' dS dr \quad (29)$$

14
15
16 364 where $\mu(r)$ and $\tau^{-1}(r)$ have been brought outside of the inner integral. Recalling that all the fields are expanded
17 using generalized spherical harmonics, the necessary angular integrals can be trivially evaluated using the
18 appropriate orthogonality relations.
19
20

21 In contrast, if viscosity varies laterally, we have to consider the more complicated expression
22
23

$$\begin{aligned} \int_0^{R_\oplus} \int_{\partial M_r} 2\mu(r) & \left[\dot{\mathbf{m}} : \mathbf{m}' + \frac{1}{\tau(r, \theta, \varphi)} (\mathbf{d} - \mathbf{m}) : (\mathbf{d}' - \mathbf{m}') \right] dS dr \\ &= \int_0^{R_\oplus} 2\mu(r) \int_{\partial M_r} \frac{1}{\tau(r, \theta, \varphi)} (\mathbf{d} - \mathbf{m}) : \mathbf{d}' dS dr, \end{aligned} \quad (30)$$

24
25
26 367 Evaluation of this integral term requires a pseudo-spectral approach (e.g., Kendall *et al.*, 2005) where certain
27 operations are performed within the spatial domain (e.g., multiplication) and others in the spectral domain (e.g.,
28 differentiation), with fast transformations used to pass fields between these two domains.
29
30

31 Despite only radial load changes at the surface due to evolving ice sheets and oceans, the introduction of
32 lateral viscosity heterogeneity gives rise to forces that now excite toroidal modes. We note, however, that even
33 in a laterally homogeneous Earth, the adjoint GIA problem can also excite toroidal modes through the presence
34 of surface tractions in the adjoint load, which for example occurs for observations of horizontal solid Earth
35 deformation. Thus, in either case we can obtain the full deformation field, $\{\dot{\mathbf{u}}, \dot{\phi}\}$ or $\{\dot{\mathbf{u}}^\dagger, \dot{\phi}^\dagger\}$, by now solving
36 two coupled sets of linear equations
37
38

$$\mathbf{A}_l^s \dot{\mathbf{x}}_{lm}^s + \mathbf{g}_{lm}(\dot{\mathbf{x}}) = \mathbf{b}_{lm}^s, \quad (31)$$

39
40 376 and
41
42

$$\mathbf{A}_l^t \dot{\mathbf{x}}_{lm}^t = \mathbf{b}_{lm}^t, \quad (32)$$

1
2
3 where the superscripts s and t denote the spheroidal and toroidal subsystems, respectively. The vector $\dot{\mathbf{x}}_{lm}^s$
4 contains the unknown spheroidal components, $\langle \dot{U}_{lm}, \dot{V}_{lm}, \dot{\phi}_{lm} \rangle$, while the unknown toroidal component, \dot{W}_{lm} ,
5 is contained within the vector $\dot{\mathbf{x}}_{lm}^t$. In alignment with the above discussion, we solve eq. (31) iteratively and
6 eq. (32) directly. In turn, solutions to these systems of equations can be mapped back into the more familiar
7 spherical coordinate system (see Appendix B of Crawford *et al.*, 2018, or Appendix C of Dahlen & Tromp,
8 1999). Thus, by adopting these changes, we can now solve the forward and adjoint GIA problem subject to
9 either a 3D viscosity structure or surface tractions at any given instant in time.
10
11

12 Although not exclusive to the inclusion of lateral viscosity heterogeneity, the common presence of low
13 viscosity regions in 3D viscosity models has important consequences for the time evolution of the forward and
14 adjoint GIA equations. Inspection of eqs. (1), (2), (16), and (17) reveal that the deformation field, $\{\dot{\mathbf{u}}, \dot{\phi}\}$, and
15 sea-level rate, $\dot{S}L$, depend only on the current state of the system. Thus, an explicit time-stepping scheme is
16 straightforward to implement and we, as in Al-Attar & Tromp (2013) and Crawford *et al.* (2018), use the second
17 order Runge-Kutta method (Press *et al.*, 1986) and set the time step to be approximately half the minimum
18 *Maxwell relaxation time*, τ , which is a suitable choice for an explicit method (Bailey, 2006). Nevertheless, since
19 mantle viscosity values as low as $\sim 10^{18}$ Pa·s have been reported or inferred in some regions (e.g. Whitehouse
20 *et al.*, 2019; Russo *et al.*, 2022, and Supp. Figure S2) and require time steps of much less than a year, it is clear
21 that explicit time-stepping schemes are not ideal for simulations spanning tens of thousands of years or more.
22 Future improvements to our numerical implementation might be obtained through use of implicit time-stepping
23 schemes.
24
25

396 3.3 Recalibration of Initial Sea Level using the Adjoint Method

40
41 Predictions of past or future sea level and topography – whether Earth's viscosity structure is laterally ho-
42 mogeneous or variable – should result in a realistic final topography that matches the observed present-day
43 topography. This well-known problem within the GIA community is commonly addressed by iteratively updat-
44 ing the prescribed initial sea level by subtracting the difference between the predicted and observed final sea level
45 until the desired accuracy is achieved (e.g., Kendall *et al.*, 2005). Here, we take a different approach and use
46 the adjoint method along with gradient based optimization (as suggested by Crawford *et al.*, 2018). Moreover,
47 we will find this approach useful in future work that simultaneously updates multiple model parameters (e.g.,
48 mantle viscosity and initial sea level; Lloyd *et al.*, in prep). For now, we focus on the basics of recalibrating the
49 initial sea level for any set of Earth and ice history models.
50
51
52
53
54
55
56
57
58
59
60

1
2
3 406 In our approach, each iteration, i , begins with a forward GIA simulation that is initiated in part by the current
4
5 407 initial sea level and is followed by a misfit calculation using the function
6
7
8

$$\mathcal{J}^i = \frac{1}{2} \int_{\partial M} \left[SL_{prd}^i(\mathbf{x}, t_p) - SL_{obs}(\mathbf{x}, t_p) \right]^2 dS. \quad (33)$$

9
10
11 408 Here $SL_{prd}(\mathbf{x}, t_p)$ and $SL_{obs}(\mathbf{x}, t_p)$ are the predicted and observed sea level, respectively, at position $\mathbf{x} \in \partial M$
12
13 409 and at the present day, t_p . We next calculate the adjoint loads in the same manner as in Section 3.1, but now by
14
15 410 perturbing eq. (33) with respect to SL_{prd} and obtaining
16
17
18

$$\dot{h}_{SL} = \left[SL_{prd}^i(\mathbf{x}, t_p) - SL_{obs}(\mathbf{x}, t_p) \right] \delta(t - t_p), \quad (34)$$

19
20
21 411 where again \dot{h}_u and \dot{h}_ϕ are 0. Comparing eq. (34) and eq. (25), we see these sea-level adjoint loads are
22
23 412 nearly identical with the exception that the former is defined globally and is weighted by the difference between
24
25 413 the predicted and observed present-day sea level. It is this weighted adjoint load that drives the adjoint GIA
26
27 414 simulation in the recalibration and, due to these weights, we now obtain the gradient of the misfit function with
28
29 415 respect to the initial sea-level, $D_{SL_0}\mathcal{J}^i$, through eq. (20).
30
31

32
33 416 Note that the equation for the sensitivity kernel for a model parameter, K_* , also holds for the gradient of the
34
35 417 misfit function with respect to that parameter, $D_*\mathcal{J}$, and that their difference arises from the values of the adjoint
36
37 418 state variables. For example, the initial sea-level sensitivity kernel, K_{SL_0} , (eq. (20)) depends upon the adjoint
38
39 419 sea level at the final adjoint time, t_1^\dagger , and for the same adjoint simulation setup, its value is solely dependent on
40
41 420 the characteristics of the adjoint load. We also point out that the use of the adjoint sea level at the final adjoint
42
43 421 time is consistent with the equations of Crawford *et al.* (2018), but not the manuscript text where they state
44
45 422 that only the elastic adjoint problem needs to be solved. Although this statement is mathematically incorrect, it
46
47 423 will lead to reasonable results if an appropriate step length is used since it essentially replicates the traditional
48
49 424 approach, as described in Kendall *et al.* (2005). Nevertheless, in this study, we perform the entire adjoint GIA
50
51 425 simulation when calculating either the sensitivity kernel or gradient for the initial sea level.
52
53

54
55 426 With the gradient in hand, we can determine the search direction and step length necessary to find a new
56
57 427 initial sea level that minimizes the misfit function (eq. (33)). Empirically we have determined that greater misfit
58
59 428 reduction and a better overall match to the present-day sea-level can be obtained through a low-pass filtering
60
61 429 strategy that gradually retains higher-degree information within the gradient. Here filtering is done in the
62
63 spherical harmonic domain by applying a one-sided Hanning taper as a function of degree- l , which has weights
64
65

1
2
3 431 of

$$w(l) = \begin{cases} 1, & 0 \leq l < l_c \\ \frac{1}{2} \left[1 - \cos \left(\pi \frac{l_{max}-l}{l_{max}-l_c} \right) \right], & l_c \leq l \leq l_{max}, \\ 0, & \text{otherwise} \end{cases} \quad (35)$$

11 432 where l_{max} is the maximum spherical harmonic degree and l_c is the cut-off degree (i.e., corner frequency). In
 12 433 the example of Section 4.2 we set l_c to 60 when smoothing is applied to the gradient. We will discuss these
 13 434 choices further in Section 4.2. For now, we need only distinguish the smoothed or, in more general terms,
 14 435 preconditioned gradient as $PD_{SL_0}\mathcal{J}^i$, where P is an arbitrary preconditioning operator.

18 436 The gradient, $D_{SL_0}\mathcal{J}^i$, and preconditioned gradient, $PD_{SL_0}\mathcal{J}^i$, is used to determine the search direction
 19 437 and we do so using the method of steepest decent (Cauchy, 1847). In addition, we have also explored using the
 20 438 conjugate gradient method (Polak & Ribiere, 1969), but leave the discussion of this algorithm to the companion
 21 439 paper (Lloyd *et al.*, in prep). In the steepest decent method, the search direction, ψ^i , is equal to the negative of
 22 440 the preconditioned gradient. Thus, updates to the initial sea level, SL_0 , can be obtained using

$$SL_0^{i+1} = SL_0^i + \alpha\psi^i, \quad (36)$$

32 441 where α is the step length for which we seek the optimum value that minimizes the misfit (eq. (33)).

34 442 We determine the optimal step length for α by assuming that the misfit along the projection of the search
 35 443 direction forms a parabola, similar to the approach used by Tape *et al.* (2007) for seismic tomography. Given
 36 444 that at $\alpha = 0$ we already have the misfit, \mathcal{J}^i , and can readily obtain the slope of this parabola by calculating
 37 445 the directional derivative along the search direction (i.e., $\langle D_{SL_0}\mathcal{J}^i, \psi^i \rangle$), we need only determine the misfit for
 38 446 a trial step length. Here, this length is taken to be twice the x -intercept of the line described by the misfit and
 39 447 slope at $\alpha = 0$, and is

$$\alpha_t = 2 \frac{\mathcal{J}^i}{\langle D_{SL_0}\mathcal{J}^i, \psi^i \rangle}. \quad (37)$$

48 448 The resulting initial sea-level, $SL_0^i + \alpha_t\psi^i$, is then used to perform another forward GIA simulation and we again
 49 449 calculate the misfit, $\mathcal{J}_{\alpha_t}^i$. With these pieces of information, we can now determine a unique quadratic curve and
 50 450 its minimum

$$\alpha = \frac{\langle D_{SL_0}\mathcal{J}^i, \psi^i \rangle \alpha_t^2}{2 (\mathcal{J}^i - \mathcal{J}_{\alpha_t}^i + \langle D_{SL_0}\mathcal{J}^i, \psi^i \rangle \alpha_t)}, \quad (38)$$

56 451 which is a suitable step length that can be used to obtain the new initial sea-level, SL_0^{i+1} , using eq. (36). In

1
2
3 452 the above procedure it is critical to distinguish between the gradient, $D_{SL_0}\mathcal{J}^i$, and preconditioned gradient,
4 453 $PD_{SL_0}\mathcal{J}^i$, since a failure to do so may cause the parabolic assumption to break down resulting in an ineffective
5 454 estimate of the optimal step length. The degree to which this occurs depends on the extent that the gradient is
6 455 modified by preconditioning. Finally, this procedure is iteratively repeated until the convergence criteria is met.
7
8 456 For recalibration of initial sea level, we choose the convergence criterium to be $|SL_{prd}^i(\mathbf{x}, t_p) - SL_{obs}(\mathbf{x}, t_p)| <$
9 457 0.5 m $\forall \mathbf{x} \in \partial M$, based on the GIA benchmark study of Martinec *et al.* (2018).
10
11
12
13
14

15 458 **3.4 Forward and Adjoint GIA Simulation Setup** 16

17
18 459 Throughout this work, we perform forward and adjoint GIA simulations at spherical harmonic degree 64 and
19 460 for a duration of 26 kyr (i.e., 26 ka to 1950 CE) using a spatially filtered version of the ICE6G(VM5a) ice history
20 461 model (Figure 1; Argus *et al.*, 2014; Peltier *et al.*, 2015). For the solid Earth structure, we use the 1D elastic
21 462 and density structure of PREM (Dziewonski & Anderson, 1981), as well as either a filtered and truncated 3D
22 463 viscosity structure (Figure 2) or its 1D radial representation (Section 3.5, Supp. Figure S4). Our 3D viscosity
23 464 structure is based on the shear-wave speed model of GLAD-M25 (Bozdag *et al.*, 2016; Lei *et al.*, 2020) and its
24 465 creation will be discussed in detail in Section 3.5. Nevertheless, a couple of pertinent details are relevant to
25 466 the setup of the forward and adjoint GIA simulations. For example, both viscosity models extend to Earth's
26 467 surface and thus, our simulations do not formally include an elastic lithosphere. The extent of high viscosity
27 468 regions in combination with the characteristics of load changes instead determine which regions are dominated
28 469 by elastic deformation. In this manner, simulations containing lateral viscosity variations also include effects
29 470 due to changes in lithospheric thickness.
30
31

32
33 471 Given the low resolution (i.e., spherical harmonic degree 64) of the forward and adjoint GIA simulations
34 472 in comparison to the resolution of the input fields (e.g., 3D viscosity structure, surface topography, and ice
35 473 thickness), we spatially filter these data sets to avoid aliasing and minimize the Gibbs phenomenon due to the
36 474 truncation of the spherical harmonic series at degree 64. This low-pass filtering is achieved by applying a
37 475 one-sided Hanning taper as a function of degree- l (eq. (35)) to each of the fields in the spectral domain. Unlike
38 476 our previous application of eq. (35), l_c is set equal to 0, such that degree-0 (i.e., the spherical mean) is the only
39 477 degree to retain its original amplitude.
40
41

42
43 478 As noted in Section 3.2, the simulations use an explicit time-stepping scheme and this time step is approxi-
44 479 mately one half of the smallest *Maxwell relaxation time*. In the case of our 1D viscosity structure, this time step
45 480 is 50 years, while for our initial inference of 3D viscosity structure (Supp. Figure S2), the required time step
46
47
48
49
50
51
52
53
54
55
56
57
58
59
60

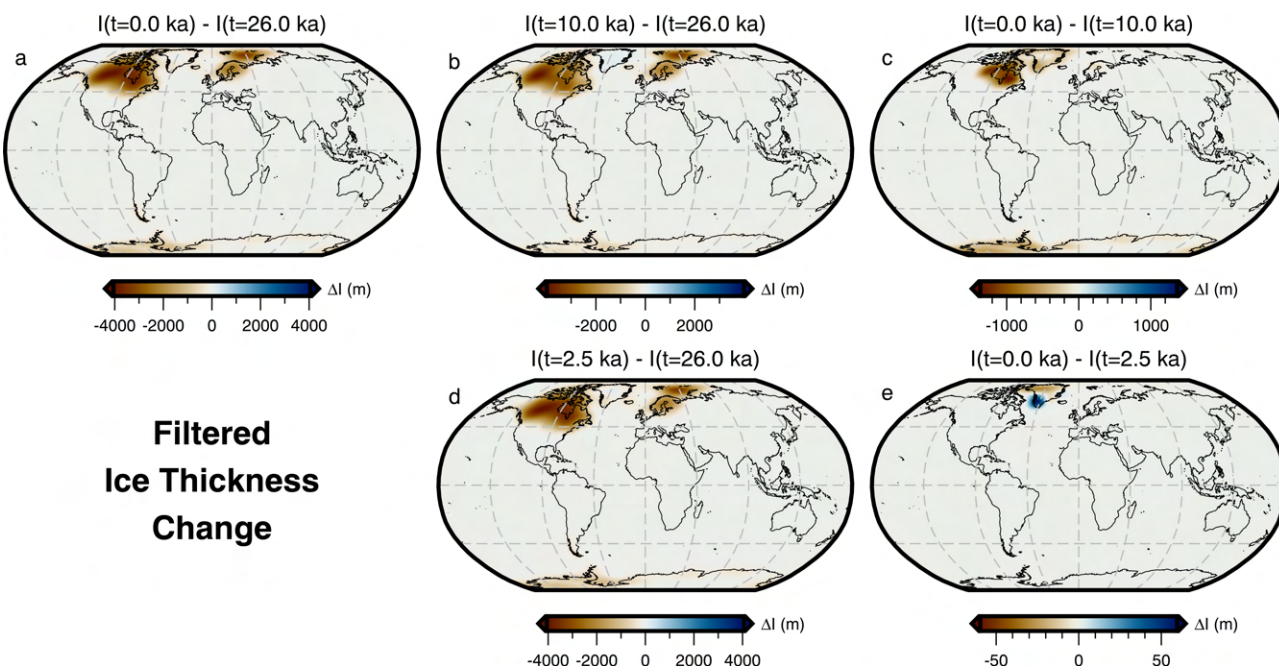


Figure 1: **Filtered ice thickness change.** Maps of the filtered ice thickness change based on the ICE6G(VM5a) ice history model (Argus *et al.*, 2014; Peltier *et al.*, 2015) between (a) 26-0 ka, (b) 26-10 ka, (c) 10-0 ka, (d) 26-2.5 ka, and (e) 2.5-0 ka. Panels *a*, *b*, and *c* are most appropriate for understanding the load changes associated with absolute sea level observations at 10 and 0 ka and the relative sea-level spanning 10-0 ka (Sections 4.3 and 4.4). Likewise, panels *a*, *d*, and *e* are most appropriate for understanding the load changes associated with absolute sea level observations at 2.2 and 0 ka and the relative sea-level spanning 2.2-0 ka (Section 4.4).

would be approximately 0.05 years. For the latter, a single forward or adjoint simulation, using OpenMP on a single compute node, would take approximately two weeks and require more than a terabyte of memory to store the needed forward variables for the viscosity kernel calculation. Unfortunately, the above filtering does not sufficiently increase the minimum *Maxwell relaxation time* for our computational resources. Therefore, given the exploratory nature of this study, the high memory requirements and computational time on a single compute node, we have chosen to limit the minimum viscosity to 2×10^{19} Pa·s, ensuring that a time step of 1 year is sufficient and subsequently each simulation requires only 18 hours. Admittedly this leads to a slight shift in the global average viscosity, but it does minimize further degrading the structure of the 3D viscosity inference, as would occur if we applied a more aggressive filter to achieve the same ends.

It is worth mentioning that work is actively underway to address these various computational limitations through algorithmic improvements in solving the forward and adjoint problems. In this manner, we expect the cost of the calculation to be substantially reduced while also allowing for increased spatial resolution.

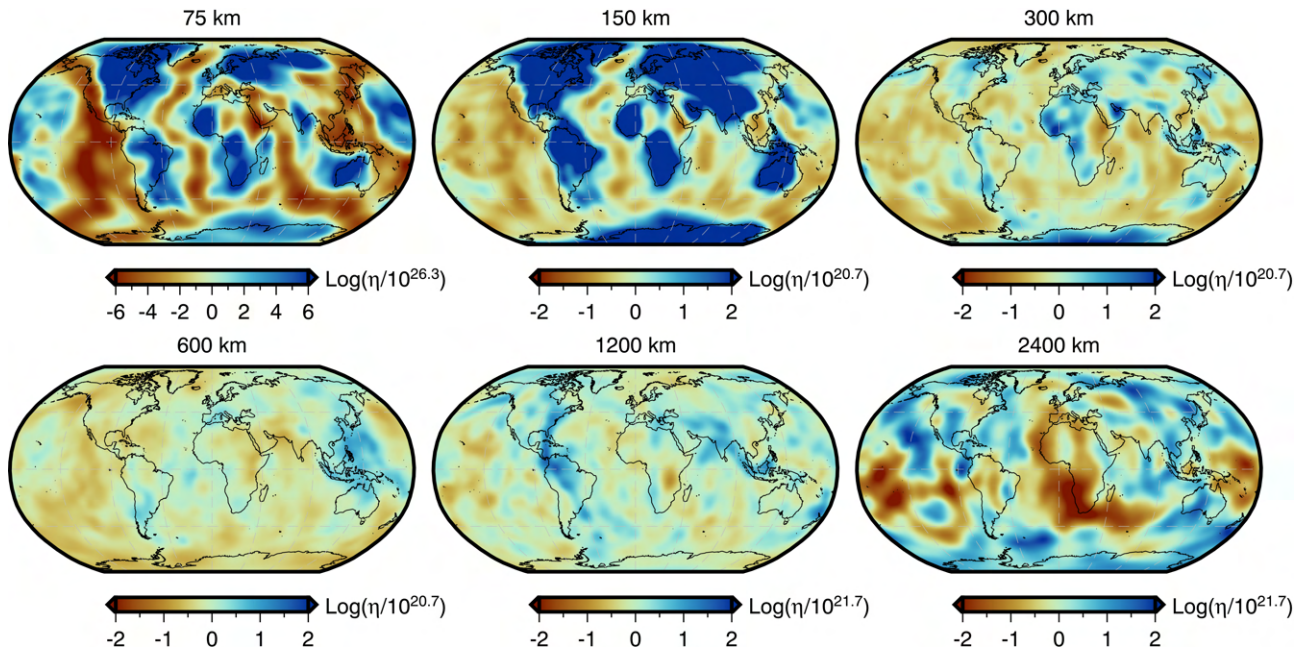


Figure 2: **Filtered and truncated 3D viscosity structure.** Depth slices through the filtered and truncated version of our inferred 3D viscosity model (Supp. Figure S2). Viscosity anomalies at each depth are relative to the 1D radial model described at the end of Section 3.5 and shown in Supp. Figure S4. This 3D model is used in the forward and adjoint simulations of Section 4.2 to determine a target present-day sea level for recalibration of the initial sea level. It is also used in Section 4.4 to explore the effect of 3D structure on viscosity sensitivity kernels.

3.5 An Inference of 3D Mantle Viscosity from GLAD-M25

We construct a new inference of 3D mantle viscosity based on a similar approach to Austermann *et al.* (2021) and using the Voight average shear-wave speeds of GLAD-M25 (Supp. Figure S1; Bozdağ *et al.*, 2016; Lei *et al.*, 2020). GLAD-M25 is the second generation of the global adjoint tomography model (Bozdağ *et al.*, 2016), whose starting point consists of the S362ANI seismic model of Kustowski *et al.* (2008) combined with crustal structure from CRUST2.0 (Bassin, 2000). Its construction over the course of 25 iterations minimizes the phase misfit of three-component body and surface waves (periods of 17–25 and 40–250 seconds, respectively) as well as reflections and overtones from 1480 earthquakes. This minimisation is achieved using gradient-based optimization in combination with the adjoint method and the computational package SPECFEM3D_GLOBE (Komatitsch & Tromp, 2002a,b), which allows for accurate and efficient calculation of both synthetic three-component seismograms and the gradient of the misfit function with respect to the model parameters. Although a formal assessment of the model’s resolution remains a challenge, point-spread function tests (Fichtner & Trampert, 2011) and comparisons with other global and regional tomography models suggest that GLAD-M25

1
2
3 506 is beginning to close the gap between global and regional studies in densely sampled areas (Lei *et al.*, 2020).
4
5 507 Nevertheless, we acknowledge that the absence of surface waves at periods less than 40 seconds suggests that
6
7 508 the uppermost mantle may be less well resolved than in other global upper mantle tomography models (e.g.,
8
9 509 Schaeffer & Lebedev, 2013).

10 510 Our inference of 3D mantle viscosity consists of three components: 1) an inverse calibration scheme for
11 the upper mantle (Richards *et al.*, 2020), 2) a traditional inference for the transition zone and lower mantle
12 (Austermann *et al.*, 2021), and 3) a merging of the two domains, which includes near surface corrections and
13 additional rheological constraints. In all instances, we relate shear wave speeds to steady-state diffusion creep
14 viscosity or viscosity perturbations by way of temperature. In so doing, we account for both linear anharmonic
15 (Kumazawa & Anderson, 1969) and non-linear anelastic (Cammarano *et al.*, 2003; Karato, 1993) effects, with
16 the latter being more pronounced in warm regions where temperatures approach the solidus. Failure to account
17 for anelasticity can lead to overestimates of absolute mantle temperatures and, by extension, underestimates of
18 absolute mantle viscosity by an order of magnitude (Austermann *et al.*, 2021). Furthermore, we assume that
19 shear wave speed variations relative to a reference model are due to temperature alone. Although this assumption
20 is incorrect, it is common (e.g. Cammarano *et al.*, 2003; Priestley & McKenzie, 2006, 2013; Richards *et al.*,
21 2020) and perhaps reasonable to assume that temperature effects dominate at global scales given uncertainties
22 in material properties of the mantle (e.g., composition, grain size, and melt fraction; Schutt & Lesher, 2006;
23 Connolly & Khan, 2016; Dannberg *et al.*, 2017; Debayle *et al.*, 2020) and the rheological mechanisms controlling
24 anelasticity (Jackson & Faul, 2010; Yamauchi & Takei, 2016). Equally important uncertainties arise from the
25 tomographic models, whose imaged wave speeds are influenced by the inverse problem setup (e.g., choice
26 of parameterization, regularization, and simplifying assumptions), the seismic phases of interest and their
27 sensitivity to Earth structure, as well as the spatial and temporal distribution of sources (e.g., noise, earthquakes,
28 etc.) and seismic stations. To manage and minimize these uncertainties, in at least the upper mantle, we use the
29 inverse calibration scheme of Richards *et al.* (2020).
30
31

47 530 The inverse calibration scheme of Richards *et al.* (2020) is rooted in the experimentally derived anelastic
48 parameterisation of Yamauchi & Takei (2016), which includes the effect of pre-melting (Takei *et al.*, 2014). It
49 531 also follows the methodological philosophy of Priestley & McKenzie (2013) that any mapping of one mantle
50 532 parameter to another should satisfy a range of average mantle properties for which there exists independent
51 533 constraints. Thus, given a suite of experimentally determined parameters (Table 2) that capture the dependence
52 534 of anelasticity on frequency and homologous temperature, we can determine a set of globally averaged mantle
53 535 constraints. Thus, given a suite of experimentally determined parameters (Table 2) that capture the dependence
54 536 of anelasticity on frequency and homologous temperature, we can determine a set of globally averaged mantle
55 537 constraints. Thus, given a suite of experimentally determined parameters (Table 2) that capture the dependence
56 538 of anelasticity on frequency and homologous temperature, we can determine a set of globally averaged mantle
57 539 constraints. Thus, given a suite of experimentally determined parameters (Table 2) that capture the dependence
58 540 of anelasticity on frequency and homologous temperature, we can determine a set of globally averaged mantle
59 541 constraints. Thus, given a suite of experimentally determined parameters (Table 2) that capture the dependence
60 542 of anelasticity on frequency and homologous temperature, we can determine a set of globally averaged mantle

1
2
3 536 material properties that satisfy existing independent constraints.
4
5
6
7
8
9

Table 2: Experimentally determined anelasticity parameters (left) from Yamauchi & Takei (2016) and the globally averaged mantle material properties (right) determined by the inverse calibration scheme of Richards *et al.* (2020).

Experimentally Determined Parameters		Globally Averaged Mantle Material Properties	
Variable	Value	Variable	Value
A_B	0.664	μ_0	80.82 GPa
α_B	0.38	$\frac{\partial \mu}{\partial T}$	-0.02 GPa·°C ⁻¹
τ'_P	6×10^{-5}	$\frac{\partial \mu}{\partial P}$	2.292
$\beta(\varphi)$	~ 0	$\log_{10} \eta_r$	23.301 ($\log_{10}(\text{Pa}\cdot\text{s})$)
$\Delta_{\text{poro}}(\varphi)$	~ 0	E_a	545 kJ·mol ⁻¹
γ	5	V_a	9.633×10^{-7} m ³ ·mol ⁻¹
T'_{η}	0.94	$\frac{\partial T_s}{\partial z}$	0.8634 °C·km ⁻¹
$\lambda\varphi$	~ 0		

22
23
24
25 537 In our mapping, as in Richards *et al.* (2020), we make use of four independent constraints and evaluate
26 each with a L2 misfit function that is weighted by uncertainties and is appropriately normalized by the sample
27 size. The observations consist of shear wave speeds from oceanic regions of GLAD-M25 that are stacked
28 with respect to lithospheric age and depth relative to sea level, as well as inferences of mantle properties
29 (temperature, attenuation, and bulk viscosity). Sampling of these observations is performed in an identical
30 manner to Richards *et al.* (2020) unless otherwise stated. The first constraint compares the oceanic stack of
31 shear-wave speed to those predicted by the plate cooling model of Richards *et al.* (2018), in which we assume an
32 ambient potential temperature of 1333°C and an equilibrium plate thickness of 133 km. Second, we require the
33 inferred temperature between 225–400 km depth beneath oceanic regions to be isentropic on average (i.e., both
34 adiabatic and reversible) and to follow the 1333°C isentrope (Shorttle *et al.*, 2014). Third, the inferred average
35 attenuation structure obtained from the relationships of Yamauchi & Takei (2016) must converge to the 1D
36 attenuation structure of QL6 (Durek & Ekström, 1996) beneath old oceanic lithosphere. Finally, we require that
37 the average of the inferred steady-state diffusion creep viscosity between 225–400 km depth be approximately
38 3×10^{20} Pa·s (Lau *et al.*, 2016). These four misfit functions are subsequently combined using weighting factors
39 of 10, 1, 2, and 2, respectively, in order to calculate total misfit.
40
41
42
43
44
45
46
47
48
49
50
51
52
53
54
55
56
57
58
59
60

To determine the optimal set of globally averaged mantle material properties that satisfy the above constraints,
we initially perform a coarse parameter sweep in order to bound the global minimum. The parameter set with
the lowest misfit value is then chosen as the starting point in a conjugate gradient scheme (Powell, 1964; Press

1
2
3 555 *et al.*, 1986) that seeks to further converge on the global minimum. The resulting parameters can be found in
4
5 556 Table 2 and are used to convert upper mantle shear-wave speeds of GLAD-M25 into temperature and absolute
6
7 557 steady-state diffusion creep viscosity down to 400 km depth.

8 558 At greater depths, we lack sufficient observational constraints to apply the inverse calibration scheme
9
10 559 of Richards *et al.* (2020) and must fall back on more traditional approaches. Here, we follow Austermann
11
12 560 *et al.* (2021) and convert shear-wave speed variations relative to the 1D radial average of GLAD-M25 into
13
14 561 temperature variations about a quasi-steady state mantle geotherm (Schuberth *et al.*, 2009). The anharmonic
15
16 562 component of this conversion assumes a pyrolytic mantle composition and makes use of the Perple_X Gibbs
17
18 563 free-energy minimization software (Connolly, 2005) along with the thermodynamic database of Stixrude &
19
20 564 Lithgow-Bertelloni (2011). An anelastic correction is made based on the 1D attenuation model Q5, associated
21
22 565 relationships from Cammarano *et al.* (2003), and a mantle solidus from Andrault *et al.* (2011). Finally, these
23
24 566 temperature variations are mapped to viscosity variations following Steinberger & Calderwood (2006).

25 567 We now merge these two domains in order to produce a spherical 3D viscosity model of the mantle and
26
27 568 crust that has a high viscosity lid, an average viscosity of 5×10^{20} Pa·s in the sublithospheric upper mantle, and
28
29 569 an average viscosity of 5×10^{21} Pa·s in the lower mantle. In doing so, we address the fact that GLAD-M25's
30
31 570 topology geometrically includes ellipticity, surface topography and internal seismic discontinuities (e.g., the
32
33 571 Moho; Bozdağ *et al.*, 2016; Lei *et al.*, 2020), as well as the fact that updates to the model may cause crust
34
35 572 or mantle wave speeds to exceed the extent of the *a priori* prescribed and fixed Moho. Representing crustal
36
37 573 viscosities requires identifying the depth extent of a *crust-like* region, which we take to be the maximum of
38
39 574 either the Moho prescribed by the starting model of GLAD-M25 (i.e., CRUST2.0; Bassin, 2000) or the depth of
40
41 575 the minimum temperature inferred by the inverse calibration scheme. For the top of the *crust-like* region, we
42
43 576 simply ignore the topography present in GLAD-M25 and define the upper surface to coincide with present-day
44
45 577 sea level. We identify the Lithosphere-Asthenosphere Boundary (LAB) to be the 1175°C isotherm, similar to
46
47 578 Austermann *et al.* (2021), and find that the spherical average depth of this boundary is ~ 100 km. Furthermore,
48
49 579 the volumetrically averaged viscosity of the mantle lithosphere is ~ 1.8×10^{26} Pa·s and it is this value that we
50
51 580 assign to the *crust-like* region. Thus, the volumetric average of the entire lithosphere remains unchanged, with
52
53 581 constant viscosities within the crust and laterally variable ones within the lithospheric mantle.

54 582 Within the sublithospheric upper mantle, we transition from using the inverse calibration scheme of Richards
55
56 583 *et al.* (2020) to the more traditional approach of Austermann *et al.* (2021) at 400 km depth. At this depth, we
57
58 584 average the two viscosity inferences assuming a reference viscosity of 5×10^{20} Pa·s (or ~ 20.699 in logarithmic

space) for the traditional approach. It is this reference viscosity that we wish to be the volumetrically averaged viscosity of the sublithospheric upper mantle extending from the LAB down to 670 km depth, similar to Austermann *et al.* (2021). However, unlike in their 3D viscosity inference, we impose this condition differently. We calculate the volumetric average viscosity of the sublithospheric upper mantle (~ 20.928 in logarithmic space) and apply a uniform shift of -0.229 in log space in order to satisfy this constraint. Finally, within the lower mantle (i.e., 670–2891 km depth), absolute viscosity is determined assuming a reference viscosity of 5×10^{21} Pa·s, which is also the adopted average viscosity of the lower mantle.

The resulting 3D viscosity inference is shown in Supp. Figure S2 and the entire model including temperatures may be found in the supplementary materials. Likewise, estimates of LAB depth based on the 1175°C isotherm are provided and shown in Supp. Figure S3. This separation is done to avoid confusion with the filtered and truncated 3D viscosity model (Figure 2) that is derived from the initial inference and used in the forward and adjoint GIA simulations. Our treatment of the mantle and crust as entirely viscoelastic is a departure from traditional GIA models that invoke an elastic lid (which implies knowledge of the effective elastic thickness of the lithosphere). Constraining this thickness remains challenging and its meaning varies across geophysical disciplines (e.g., Lau *et al.*, 2020). Instead, we believe a more elegant approach is to avoid defining the elastic thickness and instead allow the degree of elastic versus viscous deformation to be determined by material properties interacting with the geometry and time scale of surface load changes.

As a final step, we construct a comparable 1D radial viscosity model based on this 3D viscosity inference (Supp. Figure S4). This model consists of a 100 km-thick, high-viscosity ($\sim 1.8 \times 10^{26}$ Pa·s) lid, a sublithospheric upper mantle (100–670 km depth) viscosity of 5×10^{20} Pa·s, and a lower mantle (670–2891 km depth) viscosity of 5×10^{21} Pa·s. We use this model in all forward and adjoint GIA simulations herein that adopt a 1D viscosity model.

4 Results and Discussion

4.1 Forward Simulations of Sea-Level Change

The total sea-level change from 26 ka to 1950 CE predicted by forward GIA simulations and driven by the filtered ICE6G(VM5a) ice history model (Section 3.4) is shown in Figure 3. This figure includes the results that adopt both the filtered and truncated 3D viscosity model (Figure 2) and its 1D radial representation (Section 3.5). As expected, the largest total sea-level change occurs near the former Laurentide and Fennoscandian ice sheets,

1
2
3 613 in which peak sea-level fall reaches ~ -800 m over the course of 26 kyr for the 1D viscosity model (Figure 3b).
4
5 614 In contrast, adoption of our 3D viscosity model results in peak sea-level fall of ~ -700 m and ~ -500 m within
6 615 the footprint of the Laurentide and Fennoscandian ice sheets, respectively (Figure 3a). The difference in total
7 616 sea-level change in these two simulations is shown in Figure 3c and is equivalent to the difference in their final
8 617 sea level because they use the same initial sea level obtained from the filtered ICE6G(VM5a) ice history. Thus,
9 618 for later clarity we refer to the results in Figure 3c as the difference in final sea level.
10
11
12
13

14 619 In the near field, which includes the ice sheets and their forebulge, we observe higher sea level within
15 620 the footprint of the former Laurentide and Fennoscandian ice sheets, as well as within coastal regions of East
16 621 Antarctica and Greenland for the 3D viscosity model (Figure 3c). As expected, sea level is generally lower at the
17 622 peripheries of these regions within the forebulge. In contrast, we find lower sea level within West Antarctica and
18 623 central Greenland, and where a clear forebulge exists, higher sea level is observed. These differences in final sea
19 624 level in part reflect the relative stiffness of our 3D viscosity structure with respect to its 1D radial representation.
20
21 625 In our 3D viscosity model, the Canadian Shield, Fennoscandian Shield, Greenland, and East Antarctic Shield
22 626 are all underlain by an overall stiffer mantle, which reflects their thick, cold, in some cases cratonic lithosphere
23 627 and their long-term tectonic stability. As a result of the stiffer mantle, these regions experience less solid
24 628 Earth deformation in response to ice-mass change. Thus, areas of net ice-mass loss experience lower uplift
25 629 and subsidence, leading to higher sea level within the footprint of the ice sheets and lower sea level within
26 630 the forebulge. Within areas of net ice-mass gain (e.g., central Greenland) deformation is similarly muted, but
27 631 the direction of deformation and by extension sea-level change is opposite. In contrast, the mantle underlying
28 632 West Antarctica is weaker in our 3D viscosity structure relative to its 1D radial representation, which reflects
29 633 the warmer mantle and thinner lithosphere that are characteristic of tectonically active regions, and therefore
30 634 undergoes greater deformation. Regions of net ice-mass loss (e.g., West Antarctica) experience greater solid
31 635 Earth uplift (i.e., lower sea level) directly beneath and greater solid Earth subsidence (i.e., higher sea level) at
32 636 their peripheries. Finally, we note that a similar pattern is observed in Patagonia and reflects regional ice-mass
33 637 loss and a weaker mantle, although this feature is of insufficient amplitude to be visible in Figure 3c.
34
35

36 638 In the far field (i.e., beyond the extent of forebulges), sea level is generally higher by up to 10 m in the open
37 639 ocean for the 3D viscosity model relative to its 1D radial representation. As for the near field, final sea-level
38 640 differences in the far field arise, in part, due to the difference in viscous structure and by extension lithospheric
39 641 thickness between the two viscosity models. For example, greater sea-level rise is observed in the open ocean
40 642 when adopting our 3D viscosity model because the underlying mantle is weaker relative to our 1D viscosity
41
42
43
44
45
46
47
48
49
50
51
52
53
54
55
56
57
58
59
60

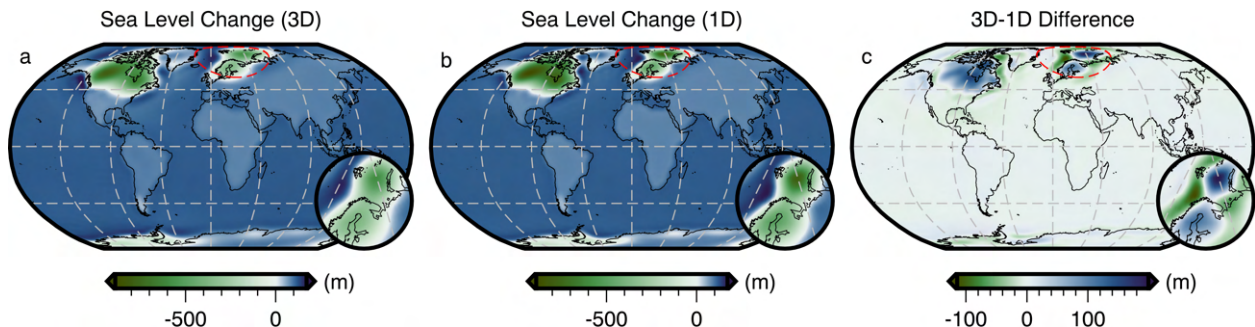


Figure 3: **Predicted sea-level change from 26 ka to 1950 CE for different viscosity structures under the assumption of consistent initial sea level.** (a) Result for filtered and truncated 3D viscosity structure (Figure 2); blue colors indicate sea-level rise and green colors indicate sea-level fall; red dashed line shows location of inset zoom over Fennoscandinavia plotted in lower right. (b) Same for 1D viscosity structure (Section 3.5). (c) Difference in total sea-level change at 1950 CE between 3D and 1D viscosity structures. Here, blue (green) colors indicate greater (lesser) sea level relative to the 1D simulation results.

model. Meanwhile, a more complex pattern with a similar magnitude is observed along coastal regions and often includes a switch in polarity across the coastline that reflects variations in the magnitude of continental levering. A detailed examination of the influence of 3D structure on continental levering is beyond the scope of this work and we refer the reader to Austermann *et al.* (2021).

Although much of the difference in final sea level shown in Figure 3c is due to the viscosity contrast between our 3D viscosity model and its 1D radial representation, a component is also due to our assumption of the same initial sea level for both simulations. As a result of their different viscoelastic properties, some regions, particularly marine-based sectors of the ice sheets, are subject to alternative histories of ocean loading and unloading, solid Earth deformation, and gravitational changes. Quantifying this contribution requires determination of an initial sea level for each individual simulation that will yield a consistent sea-level (i.e., topography) prediction at the final timestep. Thus, we now turn our attention to recalibration of the initial sea level.

4.2 An Example of Initial Sea-level Recalibration

Following the procedure laid out in Section 3.3, we perform an initial sea-level recalibration. We have chosen to take the final sea level predicted by the forward GIA simulation using the filtered and truncated 3D viscosity model as the *observed* present-day sea level and we iteratively invert for the initial sea level that is required to match this observation for simulations that use the 1D viscosity model. We find that this inversion converges rapidly over the course of 4-5 iterations, during which the greatest misfit reduction ($\geq 90\%$) occurs in the

1
2
3 661 first iteration (Figure 4a). Neglecting to implement a suitable smoothing strategy, however, leads the inversion
4 662 to become easily trapped in local minima that are related to instabilities in the vicinity of the former marine
5 663 ice sheets. For such an inversion without smoothing, this behaviour results in differences between predicted
6 664 and observed final sea level of $\sum \pm 25$ m to the north of Fennoscandia and $\sum \pm 10$ m in Hudson Bay and the
7 665 Northwestern Passages of North America (Figure 5c). These instabilities dominate the highest degrees of our
8 666 spherical harmonic basis functions and likely arise from their truncation above $l_{max} = 64$.
9
10
11
12
13

14 667 In order to avoid these numerical instabilities, as well as to improve the fit of the predicted and *observed*
15 668 present-day sea level, we employ the smoothing described in Section 3.3 within a two stage inversion procedure.
16
17 669 In the first stage, we apply a one-sided Hanning taper to the initial sea-level kernel (eq. (20)) and set l_c equal
18 670 to 60 (eq. (35)). As in the example without smoothing, the inversion initially converges rapidly and achieves
19 671 a similar degree of misfit reduction over 4-5 iterations (Figure 4a), but now the maximum difference between
20 672 the predicted and *observed* present-day sea level is reduced to ~ 1.5 m (Figure 4b). Figure 6c shows that there
21 673 remains some ringing artifacts radiating from points of highly localised discrepancy that have peak amplitudes
22 674 of ~ 1 m and are associated with the truncation of the spherical harmonic transformation. To further reduce these
23 675 discrepancies and artifacts, we perform a second stage of the inversion that includes higher degree information.
24
25 676 We now use the full, unfiltered initial sea-level kernel and, over the course of another 4 iterations, the misfit
26 677 decreases by a further two orders of magnitude and the maximum difference between the predicted and *observed*
27 678 present-day sea level decreases to 0.38 m, thereby satisfying our convergence criteria (Figure 6). Although
28 679 minor ringing artifacts persist, this second stage of the inversion procedure reduces their maximum amplitude
29 680 to only ~ 0.05 m. Thus, we now have a new initial sea level that, when used with our 1D viscosity model,
30 681 predicts present-day sea level that is consistent with that of the original forward GIA simulation for the filtered
31 682 and truncated 3D viscosity model.
32
33

34 683 Using results from the forward GIA simulation that adopts the 1D viscosity model and the recalibrated initial
35 684 sea-level (SL_0^7), we can now decompose the difference in final sea level for our two original forward simulations
36 685 (shown in Figure 3c) into a component that is due to the different viscosity models versus that arising from our
37 686 assumption of the same initial sea level (SL_0^0). The contribution of the former is shown in Figure 7b and has
38 687 been obtained by differencing the total sea-level change predicted by the forward simulation with 3D viscosity
39 688 (Figure 3a) and the 1D case using the recalibrated initial sea level (Figure 7a). Note that this difference is
40 689 equivalent, within numerical accuracy, to that between the two initial sea levels (SL_0^0 and SL_0^7). The amplitude
41 690 of the 3D-minus-1D difference in sea-level change for the recalibrated initial sea level (i.e., Figure 7b) is more
42
43
44
45
46
47
48
49
50
51
52
53
54
55
56
57
58
59
60

1
2
3 subdued within and near former marine ice sheets in comparison to that for simulations that use the same initial
4 sea level (i.e., Figure 3c). For example, the difference in the total sea-level change within the marine portion of
5 the former Fennoscandian ice sheet has decreased from ~ 200 to ~ 170 m. This difference, and others shown
6 in Figure 7c, reflects changes in the history of loading and unloading of the oceans, including their viscoelastic
7 response, resulting from the recalibration of initial sea level. The overall pattern of 3D-minus-1D sea-level
8 change, nevertheless, remains similar and our prior discussion in Section 4.1 on the influence of relative changes
9 in viscosity therefore remains valid.
10
11

12 Through this example, we have demonstrated the success of the initial sea-level recalibration based on the
13 adjoint method and gradient based optimization, which can be implemented in more complex inversions that
14 also update other model parameters (e.g., mantle viscosity; Lloyd *et al.*, in prep). Although we focused here on
15 results obtained using the method of steepest decent, we also tested the conjugate gradient method and found it
16 produced consistent results (Figure 4). In all instances, the degree of success of the inversion relied on a suitable
17 smoothing strategy that assimilates and matches longer wavelength spherical harmonic degree structure first and
18 then systematically introduces higher degree structure in latter iterations. This approach is similar to that taken
19 in adjoint seismic tomography (e.g., Zhu *et al.*, 2015; Lloyd *et al.*, 2020), where progressively shorter period
20 waveforms are assimilated in later iterations. In our inversion strategy, however, we have chosen to control
21 the length scale of new information by low-pass filtering the gradient as opposed to filtering the predicted and
22 observed data (e.g., Zhu *et al.*, 2015; Lloyd *et al.*, 2020). Finally, armed with two suitably calibrated initial sea
23 levels (SL_0^0 and SL_0^7), we can now explore viscosity sensitivity kernels for sea-level observations in order to
24 understand how these data will likely inform inversions for 3D mantle viscosity.
25
26

40 41 42 43 44 45 46 47 48 49 50 51 52 53 54 55 56 57 58 59 59 60 711 4.3 Viscosity Sensitivity Kernels for Sea-level Observations

712 We begin by examining viscosity sensitivity kernels that relate changes in sea-level observations to viscosity
713 perturbations within the solid Earth. We recall that these kernels are calculated following eq. (22) and that they
714 are a linear approximation of the Fréchet derivative relative to the assumed viscosity structure, in which the
715 range of their validity has been explored by Crawford *et al.* (2018) and Tromp & Mitrovica (2000). We consider
716 two types of sea-level observations and hence two types of viscosity sensitivity kernels. First, an absolute
717 sea-level point measurement at a given time, t_{obs} , which was initially discussed by Crawford *et al.* (2018).
718 Second, a relative sea-level point measurement that again dates from a given time, t_{obs} , but is now defined as the
719 difference in sea level between t_{obs} and present day, t_p , and therefore reflects the change in sea level between
720

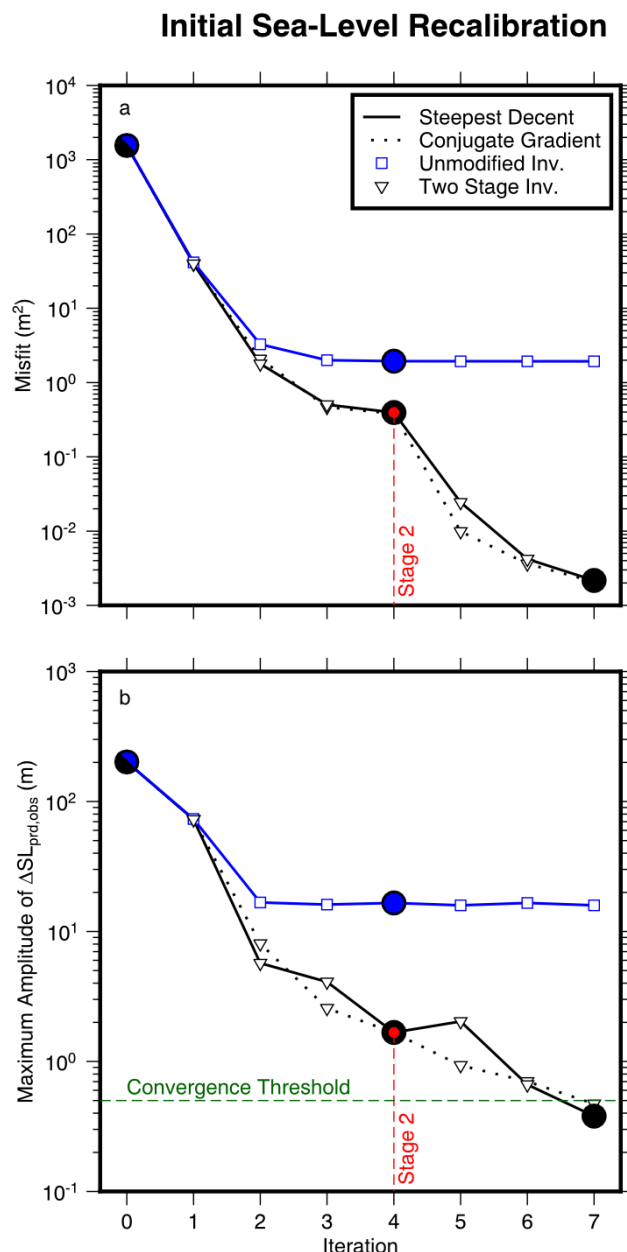


Figure 4: **Evolution of the misfit and convergence for initial sea-level recalibration.** (a) Misfit as a function of iteration number. Blue line = unmodified recalibration procedure where no smoothing is applied to the gradient; black lines = two-stage recalibration procedure where gradient is initially smoothed for four iterations (i.e., prior to red line) using eq. (31) with $l_c = 60$, before switching to the full unsmoothed gradient thereafter; solid versus dashed lines = steepest decent versus conjugate gradient minimisation; large blue and black circles indicate iterations shown in Figures 5 and 6, respectively. (b) Same for convergence test (i.e., maximum amplitude of the difference between observed and predicted final sea level). Green dashed line = convergence threshold of 0.5 m, beyond which iterations terminate. Of the three inversion strategies, the two-stage procedure using steepest decent is preferred (i.e. solid black line).

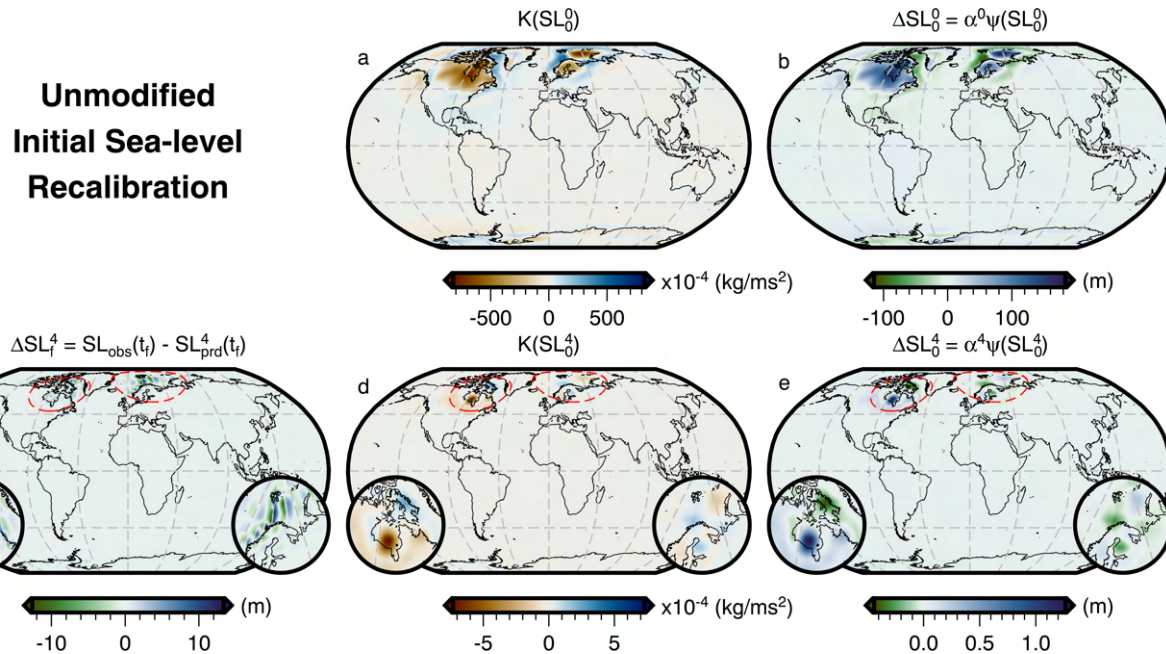


Figure 5: **Unmodified initial sea-level recalibration.** (a) Initial sea-level sensitivity kernel for the first iteration. (b) Update to initial sea level for the first iteration. (c) Difference between observed (i.e., target) present-day sea level and prediction after four iterations (N.B. equivalent plot for the first iteration appears in Figure 3c). Red dashed lines demarcate locations of 30°-wide inset zooms over Canada and Fennoscandia plotted in lower left and right, respectively, which show the features that ultimately cause the inversion to fail to converge. (d) Initial sea-level sensitivity kernel for the fourth iteration. (e) Update to initial sea level for the fourth iteration. The corresponding misfit and convergence evolution of this procedure are shown by the blue line in Figure 4.

these two times. This latter type generally corresponds to observations made in the field, since elevations of paleo sea-level indicators are measured relative to present-day sea level. We note that both absolute sea level and relative sea level are spatially variable fields. Calculation of kernels for relative sea level only requires a change to the adjoint load (Section 3.1) and thus, eq. (22) remains unchanged. Furthermore, we point out that the viscosity sensitivity kernel for a relative sea-level observation can also be constructed by differencing the sensitivity kernels for two absolute sea-level observations (i.e., $K_{SL}(\mathbf{x}_{obs}, t_{obs}) - K_{SL}(\mathbf{x}_{obs}, t_p)$; Section 3.1).

In order to explore how relative sea-level measurements might sense Earth's viscosity structure and how these sensitivities differ from those of absolute sea-level measurements, we examine the viscosity sensitivity kernels in three settings: (1) in the near field of the Fennoscandian ice sheet at Andenes, Norway, (2) on the forebulge of the Laurentide ice sheet at Barbados, and (3) in the far field at the Seychelles. To aid with intercomparison of the kernels, we consider ages of 10 ka and 0 ka for the absolute sea-level observations and 10-0 ka for the relative sea-level observation. For further simplicity, we adopt our 1D viscosity model (Section 3.5), its newly determined initial sea level (SL_0^7), and perform the forward and adjoint GIA simulations

1
2
3
4
5
6
7
8
9
10
11
12
13
14
15
16
17
18
19
20
21
22
23
24
25
26
27
28
29
30
31
32
33
34
35
36
37
38
39
40
41
42
43
44
45
46
47
48
49
50
51
52
53
54
55
56
57
58
59
60

Two Stage Initial Sea-level Recalibration

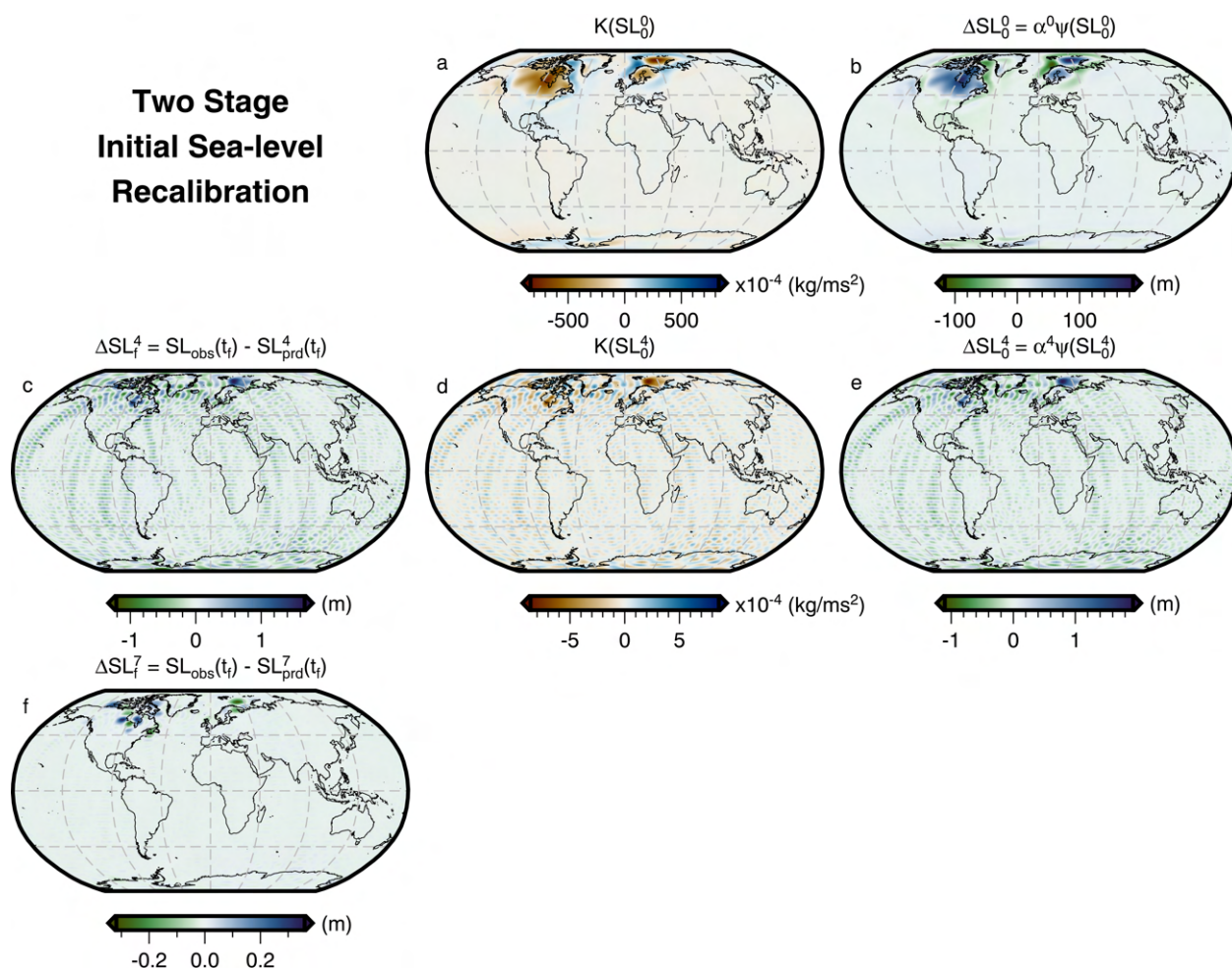


Figure 6: **Two-stage initial sea-level recalibration.** Panels are similar to Figure 5, but show results from the two-stage recalibration procedure (corresponding to the solid black line in Figure 4). In the first four iterations, this inversion applies a low-pass filter to the initial sea-level kernel to exclude information from the highest spherical harmonic degrees. Thereafter, this filter is removed and the solution satisfies our convergence criterion by iteration seven. Panel (f) shows the difference between the observed (i.e., target) and predicted present-day sea level following convergence.

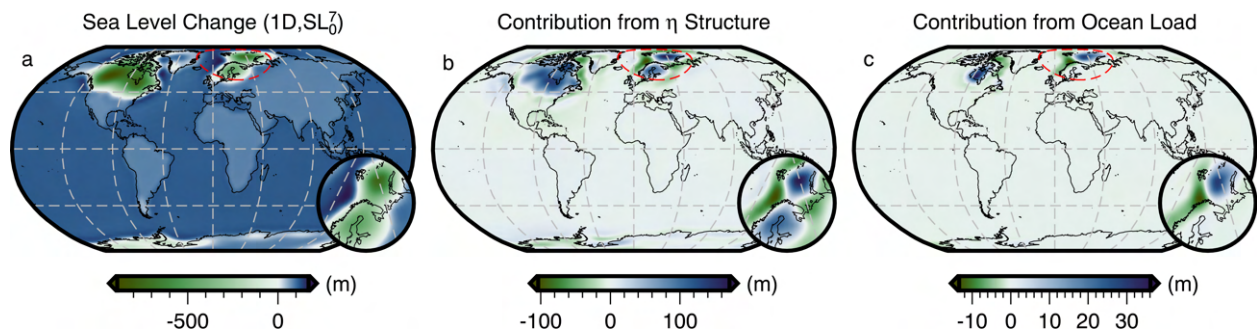


Figure 7: Influence of lateral viscosity variations and incorrect estimation of initial sea level on predictions of sea-level change. (a) Total sea-level change from 26 ka to 1950 CE for a simulation using the 1D viscosity structure and the recalibrated initial sea level, SL_0^7 . (b) Contribution to the difference in final sea level from Figure 3c that is solely due to adopting the filtered and truncated 3D versus 1D viscosity structure. This field is obtained by differencing the sea-level change in Figures 3a and 7a, and is equivalent to $SL_0^0 - SL_0^7$. (c) Contribution to the difference in final sea level from Figure 3c that is solely due to use of an incorrect initial sea level. This latter contribution adversely affects use of sea-level observations to image mantle structure and can be robustly minimised using our recalibration procedure.

as described in Section 3.4. Due to rotational symmetry of the 1D solid Earth structure, differences in the viscosity kernel for each site only reflect its location with respect to the evolving ice sheet and oceans. In comparison to Crawford *et al.* (2018), who showed sensitivities at discrete instances in time, we examine these kernels in their time-integrated form to provide a complete picture of the total sensitivity of these sea-level observations to Earth's viscosity structure. Moreover, from a geophysical imaging perspective, it is this time-integrated kernel that we relate to an observation or misfit. Thus, we will focus on building intuition about how the dominant physical processes are encoded within the viscosity sensitivity kernel, as well as how the definition of the sea-level observation influences kernel structure and its dependency on various physical processes. In turn, this intuition will guide how we invert paleo sea-level observations for 3D viscosity structure and how we interpret the resulting images in our companion study.

Critical to decoding these kernels is the ability to interpret their meaning. For absolute sea-level observations, positive (negative) kernel values indicate that an increase in viscosity at that location within the Earth leads to an increase (decrease) in sea level at the observation site. For relative sea-level kernels, changes to viscosity affect both sea level at the time the observation was encoded and sea level at the present. This factor can lead to the cancellation of similarly sensed regions and will highlight processes that lead to differences in the sea-level signal between the time of the sea-level observation and the present. In terms of the behavior of relative sea level, a positive (negative) kernel value indicates that an increase in viscosity at that location within the Earth

1
2
3 750 will increase (decrease) relative sea level at the observation site. However, the link between relative sea-level
4 751 kernels and corresponding relative sea-level change is more obscure since it depends on the size and timing of
5 752 the surface load changes (i.e., ice sheet and ocean) relative to t_{obs} and t_p , and whether sea level has risen or
6 753 fallen over this time window.
7
8

9
10 754 A few characteristics appear to be ubiquitous to the viscosity sensitivity kernels for absolute sea-level and
11 755 relative sea-level observations (Figures 8–10). With regards to absolute sea-level observations, some of these
12 756 characteristics were originally reported by Crawford *et al.* (2018), but are listed here for completeness. First,
13 757 the amplitude of the viscosity sensitivity kernels for near-field observation sites are 10 to 100 times greater
14 758 than those for far-field observation sites. Second, there is sensitivity throughout all depths of the mantle. At
15 759 shallow depths, peak sensitivities are concentrated beneath the observation site as well as beneath those regions
16 760 experiencing significant surface load changes due to the evolving ice sheets and redistribution of the oceans.
17
18 761 These regions of sensitivity broaden with depth. As we approach the core-mantle boundary, far-field observation
19 762 sites often have *visible* global coverage, while near-field observation sites have higher amplitude sensitivities that
20 763 are spatially restrictive. Nevertheless, the surface integral of the 3D sensitivity kernel at a given depth in the deep
21 764 mantle is typically small compared to shallower depths, which is consistent with past studies that determined 1D
22 765 radial sensitivity kernels for mantle viscosity (e.g., Mitrovica & Peltier, 1991; Paulson *et al.*, 2005; Wu, 2006;
23 766 Crawford *et al.*, 2018). It is only when the corresponding 3D viscosity sensitivity kernels are calculated that
24 767 one realizes the intuition gained from their 1D counterparts can be misleading. Instead, 3D sensitivity kernels
25 768 for both absolute sea-level and relative sea-level observations have non-negligible sensitivities within the deep
26 769 mantle and possess unique patterns that reflect the location of the observation site with respect to the surface
27 770 load changes. Therefore, there exists great promise for imaging not just the upper portion of the mantle's 3D
28 771 viscosity structure, but also its deepest depths. Although these generalizations are broadly correct, there are
29 772 some deviations and finer-scale structure within the kernels whose origin is not easily discerned. Nevertheless,
30 773 the structure of the kernels reflects physical processes that influence the behavior of sea level at the observation
31 774 site, which we will now discuss for three different settings.
32
33

50 775 4.3.1 Viscosity Sensitivity Kernels for Andenes, Norway

51
52

53 776 In our first example we consider a sea-level observation site at Andenes, Norway, where local sea-level has fallen
54 777 over the last 10 kyr of the simulation. Figure 8 shows depth slices at 75, 600, and 2400 km through the viscosity
55 778 sensitivity kernels for absolute sea-level observations at 10 and 0 ka, as well as for a relative sea-level observation
56
57

1
2
3 779 covering the period 10-0 ka. These kernels are dominated by high-amplitude features that reflect the nearest
4 regions of ice mass change. More distant load changes, such as the shrinking Laurentide ice sheet, generate
5 sensitivities within the underlying mantle that have a similar magnitude to those observed in kernels for far-field
6 observations at the same location (e.g., Seychelles; Figure 10). Although these low amplitude sensitivities are
7 present within the kernel and may have relevance for imaging, we will focus on higher amplitude features at
8 each depth and begin our discussion with the sea-level observations at 10 and 0 ka.
9
10
11
12
13

14 785 Within the lithosphere, the maximum amplitude of the kernel is small relative to underlying regions of the
15 sublithospheric mantle (Figure 8). This reflects the high viscosity of the lithosphere ($\sim 1.8 \times 10^{26}$ Pa·s), which
16 essentially behaves elastically at the time-scale of the simulation, and thus has a negligible effect on absolute
17 sea-level observations if its viscosity is perturbed. For both absolute sea-level observations, there is a general
18 pattern of positive kernel values beneath Andenes extending to the southeast and negative kernel values to the
19 northwest that reach a peak amplitude greater than 1000×10^{-20} m⁻² at 300 km depth and persist down to
20 ~ 550 km. Further to the northwest, the kernel again becomes positive, though its amplitude is much smaller.
21
22

23 792 Across this region, the structure of the viscosity sensitivity kernels for absolute sea-level observations reflect
24 a number of linked processes. First, the positive kernel region beneath and to the southeast, underlying the
25 former Fennoscandian ice sheet, indicates that an increase to viscosity there will lead to an increase in absolute
26 sea level at Andenes. This relationship follows from the fact that a stiffer mantle in this region will lead to
27 slower uplift during deglaciation and hence higher absolute sea level. Second, the negative kernel region to
28 the northwest indicates an increase in viscosity there will decrease absolute sea level at Andenes. We suggest
29 that this is because stiffer viscosity modifies behavior of the forebulge, reducing its amplitude and increasing its
30 width either side of the hinge point. As a result, the solid Earth at Andenes will become higher and absolute sea
31 level will decrease. Lastly, the transition back to positive kernel values further to the northwest again indicates
32 that an increase in viscosity here will result in an increase in absolute sea level at Andenes. We speculate that
33 this is because a stiffer mantle beneath this region would lead to less subsidence of the ocean basin, with the
34 formerly accommodated water mass now redistributed over the global ocean leading to an increase in absolute
35 sea level at Andenes.
36
37

38 805 From ~ 550 to 670 km depth (i.e., the base of the transition zone) the dominant features within the viscosity
39 sensitivity kernels for the absolute sea-level observations flips polarity. Here, the kernels are negative beneath
40 Andenes, while the surrounding area is now positive (Figure 8). The negative region of the kernel, which
41 indicates that an increase in viscosity there decreases sea level at Andenes, underlies the former Fennoscandian
42
43
44
45
46
47
48
49
50
51
52
53
54
55
56
57
58
59
60

1
2
3 809 ice sheet and naturally possesses the greatest local uplift at these depths. Based on our reasoning for shallower
4 810 depths, a negative kernel value beneath the ice sheet initially seems puzzling. We suggest that this behaviour
5 811 occurs due to coupling of the lower viscosity (5×10^{20} Pa·s) upper mantle and transition zone with the higher
6 812 viscosity (5×10^{21} Pa·s) lower mantle, which is a consequence of the boundary condition that the change in
7 813 displacement, \mathbf{u} , across a solid–solid boundary is $\mathbf{0}$ (eq. 2.14 Al-Attar & Tromp, 2013) (i.e., a void cannot form).
8 814 In part to satisfy this boundary condition vertical uplift above the 670 km viscosity discontinuity must decrease,
9 815 relative to that predicted for an Earth model with a uniform viscosity of 5×10^{20} Pa·s, in order to match the
10 816 deformation at the top of the higher viscosity lower mantle. Increasing mantle viscosity just above 670 km depth
11 817 reduces the viscosity contrast and reduces the needed reduction in vertical uplift required to satisfy the boundary
12 818 condition. The negative sensitivities between ~ 550 -670 km depth demarcates the region where an increase
13 819 in viscosity will allow for greater overall uplift of the solid Earth and hence lower absolute sea level. This
14 820 interpretation is consistent with the kernels switching back to positive at and below 670 km depth (Figure 8),
15 821 where a decrease in viscosity (i.e., a reduction of the viscosity contrast) leads to a decrease in absolute sea level
16 822 at Andenes. At this same depth and surrounding the negative region, the kernel is positive. Although subsidence
17 823 due to forebulge collapse does occur to the northwest of Andenes, we find vertical deformation associated with
18 824 this process dissipates by ~ 325 km depth and, at deeper depths, is characterized by low amplitude uplift.
19 825 Thus, we suggest that positive kernel values within the transition zone reflect the longer wavelength load change
20 826 associated with deglaciation of the Fennoscandian ice sheet rather than forebulge collapse. From this standpoint,
21 827 an increase in viscosity in this positive kernel region will reduce solid Earth uplift and increase absolute sea
22 828 level.

39 829 Finally, at depths of 670 km and greater (Figure 8) the viscosity sensitivity kernel beneath northern Europe
40 830 is again positive, indicating that an increase in viscosity there will increase absolute sea level at Andenes. The
41 831 amplitude of the kernel is smaller due to the higher viscosity of the lower mantle (eq. (22)) and greater distance
42 832 from the surface load change. The latter is a result of attenuation, which also more strongly dissipates the higher
43 833 spherical harmonic degrees of deformation. Thus, deformation in the lower mantle beneath northern Europe is
44 834 controlled by the lower spherical harmonic degree components of the shrinking Fennoscandian ice sheet. By
45 835 increasing the viscosity beneath northern Europe, the extent of solid Earth uplift due to unloading of the ice
46 836 sheet is reduced and hence absolute sea level at Andenes increases. In contrast, the kernels are negative beneath
47 837 northern North America. Through similar logic, an increase in viscosity there will increase absolute sea level
48 838 above that region, thereby siphoning water mass from other parts of the global ocean and, in turn, decreasing

1
2
3 839 absolute sea level at Andenes.
4
5

6 840 We next turn our attention to the viscosity sensitivity kernel for a relative sea-level observation spanning
7 841 10-0 ka and begin by addressing the relationship between absolute and relative sea level change and their
8 842 sensitivity kernels. We recall that sea level has fallen over the final 10 kyr of the simulation, such that relative
9 843 sea level is positive. Focusing directly beneath Andenes at 75 km depth the kernel is negative indicating that
10 844 an increase in viscosity there will decrease relative sea level at the observation site. But how is this achieved?
11
12 845 To understand this we recall that this kernel for a relative sea-level observation is equivalent to the difference
13 846 between the kernels for absolute sea-level observations at 10 and 0 ka. Within this same region of the mantle
14 847 both kernels are positive indicating that an increase in viscosity there will increase absolute sea level at the
15 848 observation site. Furthermore, $K_S L(t = 10 \text{ ka}) < K_S L(t = 0 \text{ ka})$ and for the same increase in viscosity the
16 849 change in absolute sea level at 0 ka is greater than that at 10 ka. When sea level has fallen this behavior
17 850 decreases the offset between absolute sea level spanning 10-0 ka and also decreases the relative sea level, which
18 851 is consistent with the interpretation of the kernel for relative sea level.
19
20

21 852 Focusing now on the structure of the Andenes example, we see that general structure of the kernel is similar
22 853 to the kernels for an absolute sea-level observation, but their polarities are flipped (Figure 8). This pattern
23 854 indicates that, in most regions, the absolute sea-level observation at 0 ka has greater sensitivity to mantle
24 855 viscosity than the sea-level observation at 10 ka. One notable exception is observed beneath the northern
25 856 marine-based portion of the Fennoscandian ice sheet at 600 km depth. Here, kernels for both types of sea-level
26 857 observations are negative and hence the kernel for a sea-level observation at 10 ka has a greater amplitude. This
27 858 difference occurs because the ice sheet disappeared from this region prior to 10 ka (Figure 1b) and illustrates
28 859 that the amplitude of the kernel for sea-level observations is greater when the time between the surface load
29 860 change and observation time is smaller. In contrast, immediately southeast of Andenes, a localised region at
30 861 600 km depth does change polarity in the kernel for relative sea level due to further ice mass loss occurring
31 862 after 10 ka (Figure 1c). These effects demonstrate the importance of details within the spatiotemporal history
32 863 of loading in influencing the structure of both types of kernel.
33
34

35 864 **4.3.2 Viscosity Sensitivity Kernels for Barbados**
36
37

38 865 In our second example, we consider an observation at Barbados, which lies at the edge of the forebulge of the
39 866 Laurentide ice sheet. Given its proximity to the ice sheet, it seems natural to assume that sea-level observations
40 867 here are sensitive to many of the same deformational processes as the site at Andenes. The change in relative
41
42

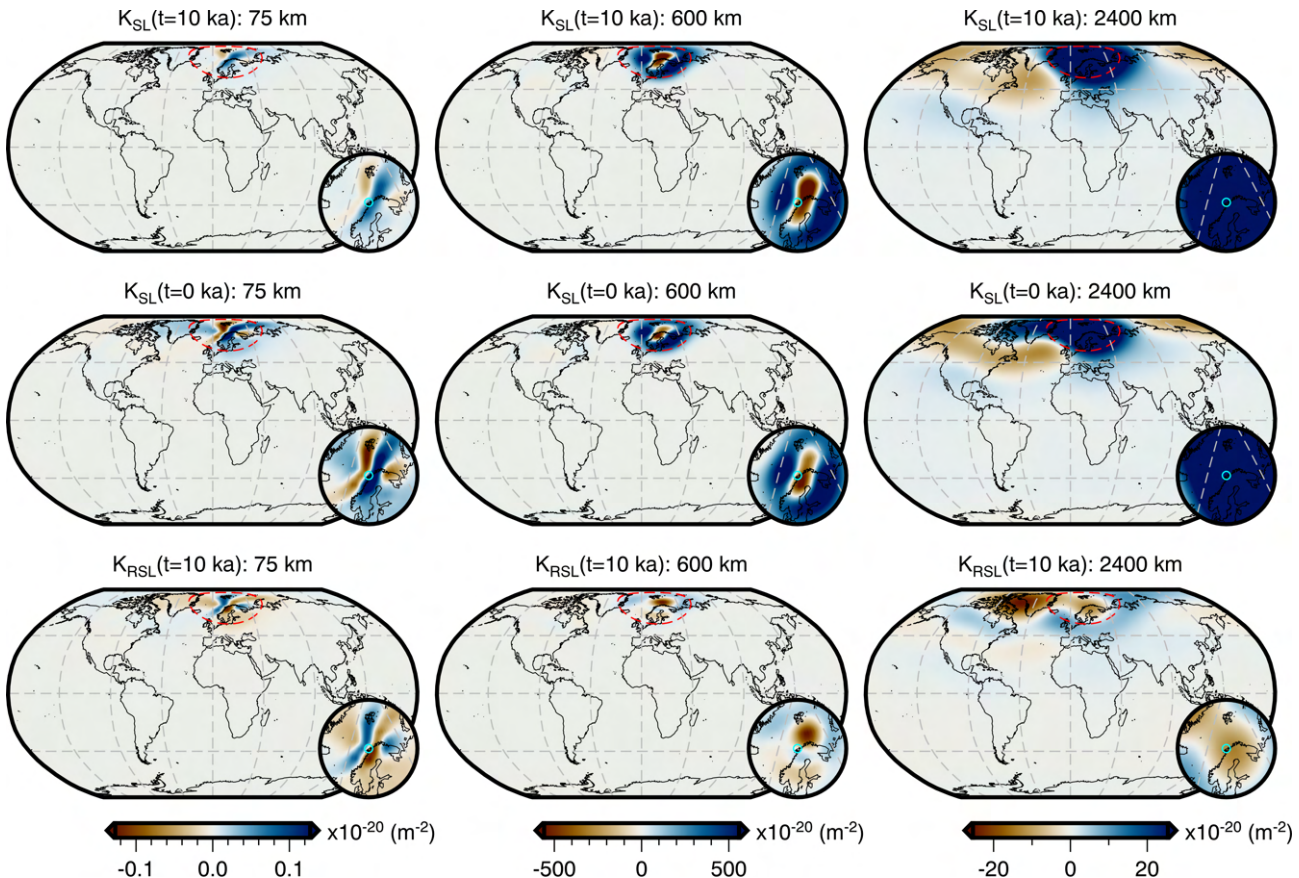


Figure 8: Comparison of viscosity sensitivity kernels for sea-level and relative sea-level observations at Andenes, Norway. Slices at 75, 600, and 2400 km depth through the viscosity sensitivity kernels for (top row) a sea-level observation at 10 ka, (middle row) a sea-level observation at 0 ka, and (bottom row) a relative sea-level measurement at 10 ka. The inset map, centered on the observation site (cyan circle), has a width of 30° and its extent is shown by the red dashed line the main map. The color scale for each column is chosen to symmetrically span the full range of relative sea-level viscosity sensitivity kernel and thus, regions of the sea-level sensitivity kernels may be saturated.

1
2
3 868 location, however, results in these processes and perturbations to the underlying mantle viscosity structure
4 869 influencing sea level at Barbados in a different manner. Figure 9 shows that sensitivity to mantle viscosity is
5 870 focused beneath the observation site and the closest regions of surface load change (i.e., the Laurentide ice
6 871 sheet), with minor sensitivity beneath the Fennoscandian ice sheet. Peak amplitudes of the sensitivity kernels
7 872 for Barbados are an order of magnitude smaller than those of Andenes. This amplitude difference will require
8 873 careful attention when imaging viscosity using sea-level data.
9
10
11
12
13

14 874 The structure of the viscosity sensitivity kernel for the two absolute sea level observations at 10 and 0 ka
15 875 is more complex in Barbados than Andenes and correspondingly more difficult to interpret. Positive kernel
16 876 values at 150 km and 600 km depth are predominantly observed beneath the former Laurentide ice sheet and
17 877 north of Barbados (Figure 9), indicating that an increase in viscosity there will raise absolute sea level at
18 878 Barbados. We speculate that, for areas around the periphery of the former Laurentide ice sheet, a stiffer mantle
19 879 in these regions will lead to slower forebulge subsidence, which causes absolute sea level to be higher elsewhere,
20 880 including Barbados. High positive kernel values along the transect from Barbados to the Laurentide ice sheet
21 881 might indicate that a differently shaped forebulge, due to a stiffer mantle, can result in deeper water depths at
22 882 Barbados. At these depths, the kernel is near zero or negative beneath Barbados itself (Figure 9), indicating that
23 883 an increase in viscosity will reduce subsidence of the solid Earth in response to the increased ocean load from
24 884 deglaciation. Hence, absolute sea level will be lower if the upper mantle is stiffer directly beneath Barbados.
25 885 This interpretation is consistent with Austermann *et al.* (2013), who showed that a high-viscosity slab in the
26 886 Caribbean subduction zone reduces local sea level.
27
28
29
30
31
32
33
34
35
36
37

38 887 Finally, at 2400 km depth, deformation is again dominated by long-wavelength load changes, which will be
39 888 dominated by the shrinking Laurentide ice sheet. Here, the sensitivity kernel has a positive kernel value directly
40 889 between the Laurentide ice sheet and Barbados and is ringed by negative kernel values (Figure 9). This feature
41 890 reflects the geometry of the load change and the observation site. While its full nature is unclear, we note that
42 891 the boundary from positive to negative kernel values nearest Barbados corresponds to a change from uplift to
43 892 subsidence of the solid Earth at this depth in the forward simulation.
44
45
46
47
48

49 893 We next turn our attention to the viscosity sensitivity kernel for a relative sea-level observation spanning
50 894 10–0 ka in Barbados. We begin again by exploring the relationship between absolute and relative sea level
51 895 change and their sensitivity kernels. In this example, sea level has risen at the observation site (i.e. relative sea
52 896 level is negative) between 10 ka and 0 ka in this simulation. Directly beneath Barbados at 150 km depth the
53 897 sensitivity kernel for the relative sea-level observation is negative indicating that an increase in viscosity there
54
55
56
57
58
59
60

1
2
3 898 will decrease relative sea level. At this same location the kernels for absolute sea level observations are also
4 899 negative with $K_{SL}(t = 10 \text{ ka}) < K_{SL}(t = 0 \text{ ka})$. Thus, for the same viscosity increase the absolute sea level
5 900 observation at 10 ka will decrease more than at 0 ka, increasing the offset of the absolute sea level spanning
6 901 10-0 ka. Given this behavior along with the fact that sea level is rising the relative sea level at the observation
7 902 site will become more negative (i.e. decrease), consistent with the interpretation of the kernel for the relative
8 903 sea-level observation.
9
10

11 904 At depths of 150, 600, and 2400 km, we find that amplitudes across the footprint of the former Laurentide
12 905 ice sheet are more uniform for a given depth in comparison to the two sensitivity kernels for absolute sea-level
13 906 observations (Figure 9). At 150 km depth, there is a stronger change in polarity at continent-ocean boundaries
14 907 along the northeastern United States and northern South America, which we suggest relate to forebulge collapse
15 908 and continental levering, respectively. Meanwhile at 600 km depth, we observe an intriguing pattern of negative,
16 909 positive, and then negative kernel values in the vicinity of Barbados, which is roughly orthogonal to the great
17 910 circle path connecting Barbados to Hudson Bay and likely relates to the dynamics of forebulge collapse. At
18 911 2400 km depth, we note that the amplitude of the viscosity sensitivity kernel is only a factor of two smaller than
19 912 that observed at 150 km depth. As we will see in the next example, this pattern of nonnegligible sensitivity to
20 913 deep mantle viscosity structure is a ubiquitous feature of these sensitivity kernels.
21
22

33 914 4.3.3 Viscosity Sensitivity Kernels for Seychelles 34

35 915 In our final example, we consider a far-field observation site in the Seychelles where sea level has risen during
36 916 the final 10 kyr of the forward GIA simulation. Figure 10 shows images of the viscosity sensitivity kernels
37 917 at depths of 300, 600, and 2400 km for the two absolute sea-level observations at 10 km and 0 ka, as well as
38 918 for a relative sea-level observation spanning the period 10-0 ka. We observe two distinct groups of kernels for
39 919 observations that are located at far-field sites. The first is characterized by a significant continental region lying
40 920 between the observation site and the dominate region of ice mass change, such that there is no appreciable ocean
41 921 load change within this intermediate region. As a result a more diffuse sensitivity pattern develops similar
42 922 to that observed in the Seychelles example (Figure 10). The second group occurs for observation sites, such
43 923 as Tahiti, where the intervening region is predominantly ocean basin. These kernels exhibit an approximately
44 924 linear, high-amplitude zone of sensitivity between the site and locations of ice-mass change (e.g. Crawford *et al.*,
45 925 2018), which is reminiscent of *banana-doughnut* kernels in seismology (Dahlen *et al.*, 2000). While we have
46 926 not provided an example of this second group here, we point out that our kernel for Barbados has some similar
47
48

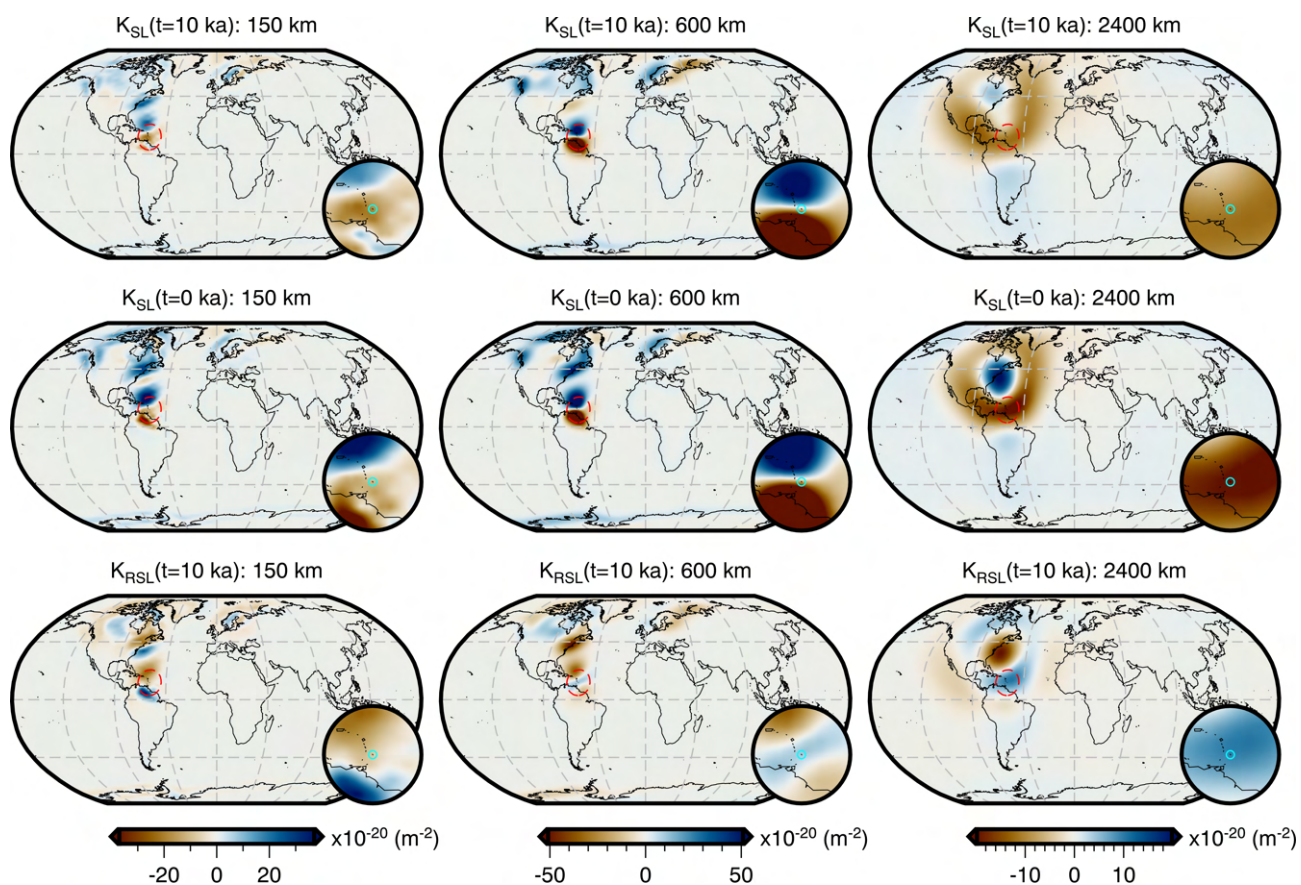


Figure 9: Comparison of viscosity sensitivity kernels for absolute sea-level and relative sea-level observations at Barbados. Panels same as Figure 8; width of inset map is 20° .

features (Figure 9).

Within the viscosity sensitivity kernel for absolute sea-level measurements at 10 and 0 ka, there are again a number of local features that reflect a range of deformational processes. First, the negative kernel value at all depths beneath the Seychelles reflects the fact that, during deglaciation, the ocean load increases and a stiffer mantle therefore results in less subsidence and lower absolute sea level, similar to Barbados. Furthermore, the negative kernel values beneath the observation site are observed throughout the mantle, suggesting that coupling between the upper and lower mantle has limited influence on the behavior of sea level at this site, in contrast to the Andenes example. We speculate that this aspect occurs because the load change due to the ocean, though long wavelength, is small in amplitude relative to that of the Fennoscandian ice sheet. Meanwhile, to the east of the Seychelles and beneath the ocean, the sensitivity kernel is positive at 300 km depth (Figure 10), indicating that an increase in viscosity there will increase absolute sea level. This relationship suggests that a stiffer mantle in this region will result in less subsidence of the solid Earth due to the rising oceans, with the

1
2
3 939 corresponding reduction in local ocean capacity raising absolute sea level at the observation site. Further to
4 940 the west, we see a positive-to-negative polarity change at 300 km depth crossing from offshore to onshore east
5 941 Africa (Figure 10). This pattern reflects the influence of continental levering on the behavior of sea level at the
6 942 Seychelles, with an increase in viscosity causing deformation across the coastline to become lower amplitude
7 943 and longer wavelength. We suggest that the Seychelles are sufficiently close to the east African shoreline to
8 944 sense this reduction in offshore subsidence during the deglaciation, raising the solid Earth and reducing absolute
9 945 sea level at the observation site.

10
11 946 The upper mantle and transition zone kernels for absolute sea-level observations at both 10 and 0 ka
12 947 have similar amplitudes within the vicinity of the ice sheets, with the highest values occurring beneath their
13 948 peripheries. We argue that this sensitivity pattern is related to ocean siphoning (Mitrovica & Milne, 2003), in
14 949 which a higher viscosity leads to slower subsidence of the peripheral bulges and hence higher absolute sea level
15 950 in the far field. Additionally, the kernel at 0 ka exhibits a negative anomaly beneath Hudson Bay. This area is
16 951 rebounding in response to glacial unloading and, following the demise of the Laurentide ice sheet, continuing
17 952 uplift will push water out of Hudson Bay and cause absolute sea level to rise in the far field.

18
19 953 Figure 10 also shows the viscosity sensitivity kernel for a relative sea-level measurement in the Seychelles
20 954 dating from 10 ka. Although this kernel does exhibit differences in polarity in some locations, the more
21 955 intriguing feature is its loss of sensitivity in some regions of the mantle. For example, at 300 km depth, there
22 956 is a reduction in regional sensitivity to viscosity and the observation is restricted to sensing viscosity structure
23 957 locally beneath the observation site and near the coastline of east Africa. This behaviour occurs because the
24 958 evolution of the local ocean load leads to similar sensitivities for absolute sea-level observations at 10 and
25 959 0 ka except for a slight westward (i.e., inland) shift of the coastline due to shoreline migration. Thus, it is
26 960 near this region that *visible* sensitivities are found, indicating the relative sea level in the Seychelles at 10 ka is
27 961 more sensitive to shoreline migration than continental levering. Similarly at 300 and 600 km depth, there is a
28 962 reduction in the spatial extent of sensitivities at the peripheries of the ice sheets. We conclude from this that
29 963 the relative sea-level measurement is less sensitive to forebulge deformation and associated ocean siphoning
30 964 than its constituent sea-level observations. Through these two examples, we have demonstrated that absolute
31 965 sea-level versus relative sea-level observations from the same location and time period can have quite distinct
32 966 sensitivities to deformational processes and thus regions of mantle viscosity.

33
34 967 To finish, we return to a striking characteristic of the viscosity sensitivity kernels for both types of far-field
35 968 sea-level observations, which is that similar amplitude sensitivities are found beneath both the region of the

1
2
3 969 observation site and the regions of ice mass change, even when the two are antipodal. This simple observation
4 970 has two profound consequences for the use of far-field relative sea-level data to constrain mantle viscosity and,
5 971 by extension, ice history. First, for a laterally heterogenous Earth, their use will lead to an estimate that blends
6 972 local and distal viscosity structure. Such biases in 1D estimates of mantle viscosity have been shown in forward
7 973 analyses (e.g., Lau *et al.*, 2018), but the sensitivity kernels in Figure 10 quantitatively illustrate the reasons for
8 974 this behaviour. From the perspective of a local relative sea-level dataset, one cannot simply disentangle the
9 975 influence of the local viscosity structure, which controls the relative local distribution of the ocean load, from
10 976 the viscosity structure beneath the changing ice sheet and forebulge regions, which dominates the change in total
11 977 water mass in the observation region. Furthermore, from the perspective of a global far-field relative sea-level
12 978 dataset, this bias is exacerbated by the fact that the mantle underlying regions of ice mass change is sampled
13 979 by every observation, while the mantle beneath the far-field may only be sampled by a handful of observations.
14
15 980 An important consequence is that 1D estimates of mantle viscosity are biased towards the viscosity structure
16 981 underlying regions of significant load change, such as the Laurentide and Fennoscandian ice sheets.

17
18 982 Second, the sensitivity kernels in Figure 10 hint at a means to minimize sensitivity to distal mantle structure,
19 983 while preserving sensitivity to local structure. We can envision this by imagining that a second observation exists
20 984 on the northern coast of Madagascar. While its kernel will locally appear quite different, the difference in distal
21 985 regions will be minor and thus, by differencing kernels (i.e., differencing the relative sea-level measurements),
22 986 sensitivity is minimized to distal mantle structure whilst being locally enhanced. This thought experiment
23 987 demonstrates the power of differential relative sea-level measurements for constraining local mantle rheology
24 988 (e.g., Nakada & Lambeck, 1989).

40 41 989 **4.4 The effect of 3D viscosity on relative sea-level observations**

42
43 990 Now that we have gained some insight into the nature of viscosity sensitivity kernels for absolute sea-level and
44 991 relative sea-level observations on a 1D radial Earth, we turn our attention to exploring the effects of lateral
45 992 variability in viscosity. Through two examples, we investigate the influence of geodynamic features including
46 993 hotspots, slabs, and variable lithospheric thickness, which are likely to be characterized by variations in viscosity
47 994 structure. Although these sources of viscosity heterogeneity influence the sensitivity kernels for both types of
48 995 sea-level observations (e.g., Figures 11 and 12 and Supp. Figures S7, S8 and S9, S9), we focus on those for
49 996 relative sea-level observations since they form the foundation of the paleo sea-level record and will be used to
50 997 invert for 3D mantle structure in our companion study (Lloyd *et al.*, in prep). Nevertheless, by accounting for

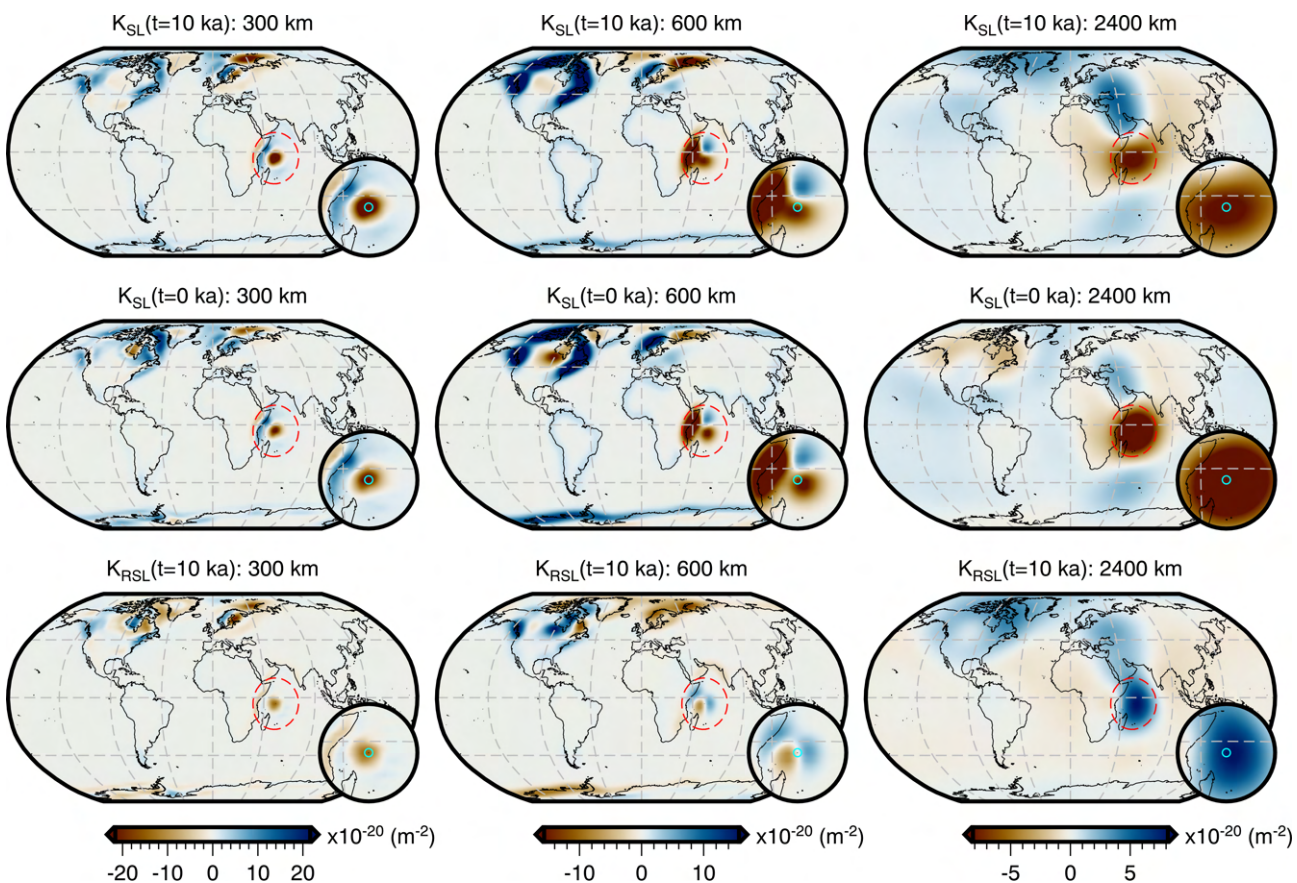


Figure 10: **Comparison of viscosity sensitivity kernels for absolute sea-level and relative sea-level observations at the Seychelles.** Panels same as Figure 8; width of inset map is 40° .

even Earth's long wavelength 3D viscous structure the kernels for both types of sea level observations represent a more realistic quantification of observational sensitivity to viscosity compared to those based on a 1D radial viscosity model (Section 4.3 and Crawford *et al.*, 2018).

In our first example, we consider a relative sea-level observation from the Amundsen Sea Embayment of Antarctica that dates to 2.2 ka (Johnson *et al.*, 2008). In this region, seismically slow mantle wave speeds (Lloyd *et al.*, 2020) and rapid uplift rates recorded by continuous GNSS stations installed on bedrock suggest the presence of a low viscosity ($\sim 10^{18} \text{ Pa}\cdot\text{s}$) upper mantle and transition zone (Barletta *et al.*, 2018). To first order, this feature is present in our filtered and truncated 3D viscosity inference (Figure 2), although it lacks the lowest of viscosities and finer scale structure that has been imaged by regional seismic tomography models (e.g., Lloyd *et al.*, 2015, 2020; Lucas *et al.*, 2020). Nevertheless, it still demonstrates the dramatic influence that even this modest degree of lateral viscosity heterogeneity can have on the structure of the viscosity sensitivity kernel (Figure 11).

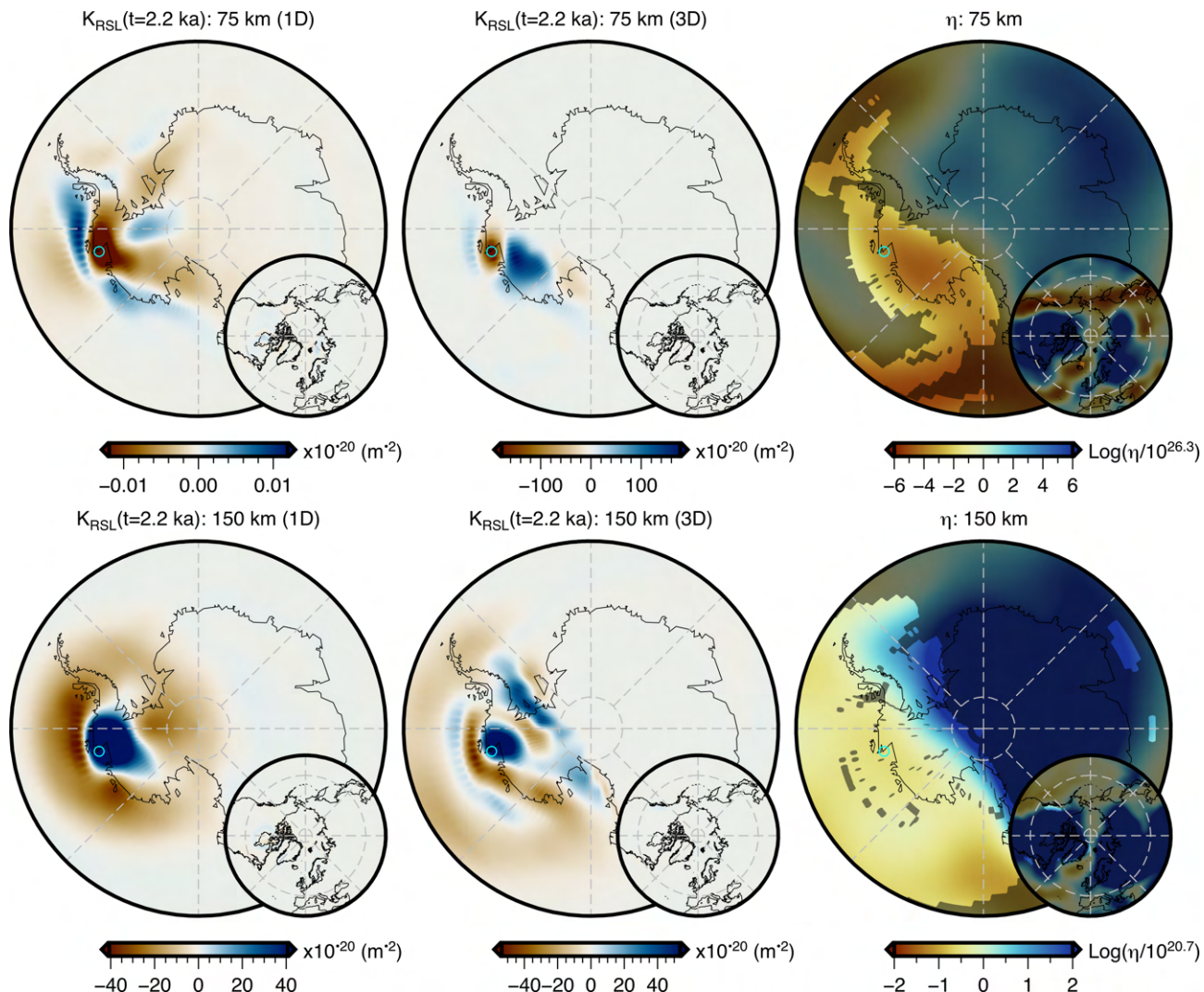


Figure 11: Relative sea-level viscosity sensitivity kernels for 1D and 3D viscosity structure. Slices at 75 and 150 km depth through the viscosity sensitivity kernels for a relative sea-level observation on an unnamed island in the Amundsen Sea Embayment (cyan circle) dating to 2.2 ka (Johnson *et al.*, 2008). The first column shows the sensitivity kernel obtained when assuming our 1D viscosity model (Section 3.5 and Supp. Figure S4) and the second column shows the sensitivity kernel obtained when assuming our filtered and truncated 3D viscosity inference (Figure 2). It is this 3D viscosity structure that is shown in the third column and regions where the amplitude of the sensitivity kernel are less than 10^{-20} m^{-2} are shaded. Finally, in each figure the inset map is centered on the north pole and has a width of 90° . Careful inspection of this inset figures reveals regions of visible sensitivity when adopting our 1D viscosity model.

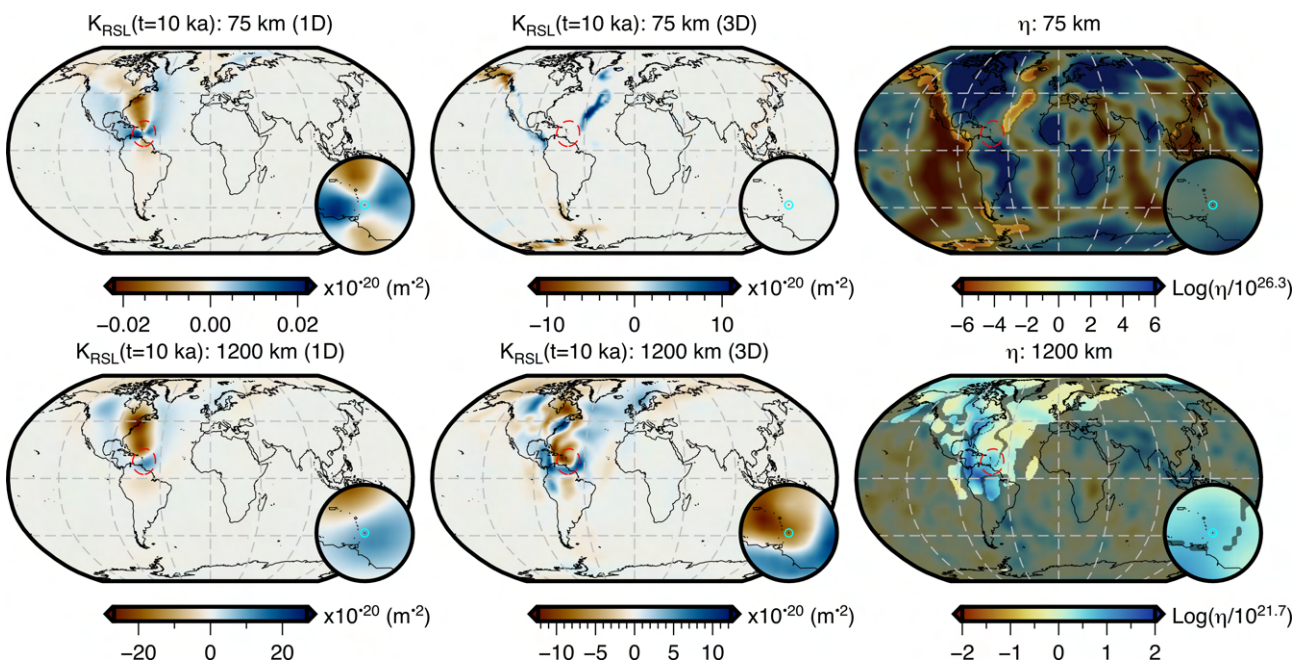


Figure 12: **Relative sea-level viscosity sensitivity kernels for 1D and 3D viscosity structure.** Similar to Figure 11, but for a relative sea-level observation at Barbados dating to 10 ka. Here we show slices at 75 and 1200 km depth in a full global map with an inset map centered on Barbados, identical to Figure 9.

Inclusion of lateral viscosity variability causes a dramatic increase in the amplitude of the sensitivity kernel at shallow depths (e.g., 75 km) from $\pm 0.01 \times 10^{-20}$ to $\pm 180 \times 10^{-20} \text{ m}^{-2}$, which reflects an increase in viscous deformation at this depth due to a weaker regional viscosity structure. In addition, we find that kernels based on the 3D viscosity model are characterized by spatially restricted, more focused features that exhibit greater complexity with depth. This pattern reflects the length scale of deformation present within the simulation and is controlled by interaction between the viscosity structure and the distribution and magnitude of the surface load changes. Furthermore, the nearly pure elastic response of the thick East Antarctic lithosphere strongly zeros out the sensitivity kernel within this region (see Figure 11 at 150 km depth).

In our second example, we consider a hypothetical relative sea-level observation from Barbados that dates to 10 ka. Barbados represents the other end member of the plate tectonic regime, as it lies along the Caribbean subduction zone where cold, high-viscosity oceanic lithosphere is subducted into the mantle. The presence of this slab has previously been argued to suppress local viscous deformation and to reduce sea-level change due to local ocean loading (Austermann *et al.*, 2013). Although our filtered and truncated 3D viscosity model does not have the resolution to fully capture the downgoing South American plate (Figure 2), sufficient structure is present to capture its likely effects on the viscosity sensitivity kernel.

In Figure 12, we see that introduction of 3D structure beneath Barbados results in negligible sensitivity at 75 km depth within high-viscosity regions and indicates that, for these load changes and at these time scales, elastic deformation dominates within this region of the mantle. In contrast, weaker viscosity regions that are located further from the observation site exhibit notably higher sensitivity because they undergo greater viscous deformation. For example, portions of the mid-Atlantic ridge have positive kernel values, indicating that an increase in viscosity here would lead to an increase in relative sea-level at Barbados. This behavior of distal viscous deformation more strongly influencing relative sea level at Barbados than local viscous deformation aligns with ocean loading model for the Caribbean subduction zone proposed by Austermann *et al.* (2013). In this model they suggest that ocean loading at Barbados produces less viscous deformation because of the high viscosity of the subducting South American plate, in contrast to adjacent regions that are underlain by weaker viscosities. At greater depths (e.g., 1200 km), we observe significant and complex changes to the structure of the viscosity sensitivity kernel for 1D versus 3D viscosity models. For example, we observe a switch from negative to positive kernel values beneath the eastern coast of North America, which may be related to presence of the Farallon slab. While the origin of these changes is not always obvious, they demonstrate the importance of 3D viscosity structure in modulating which regions of the Earth any given observation is sensitive to.

5 Conclusions

In part one of our efforts to lay out a robust framework for imaging 3D mantle viscosity using paleo sea-level observations, we have reviewed the rate formulation of the forward and adjoint GIA problem as derived by Al-Attar & Tromp (2013) and Crawford *et al.* (2018). We have extended this work to calculate sensitivity kernels for observations of relative sea level and, in the process, have demonstrated that their adjoint loads are composed of equal but opposite sea-level adjoint loads at t_{obs} and t_p . Moreover, we have shown that these kernels can also be determined by differencing the sensitivity kernels for absolute sea-level observations at t_{obs} and t_p . Although we focus on viscosity sensitivity kernels, the approach can also be used to calculate sensitivity kernels for other model parameters, such as the rate of change in ice thickness.

We have presented an extension to the numerical implementation of the forward and adjoint GIA problem that allows for the inclusion of 3D viscosity, which is a fundamental requirement for 3D imaging. In order to apply this extension sensibly, a new inference of 3D mantle viscosity based on the shear-wave speed of GLAD-M25 (Bozdağ *et al.*, 2016; Lei *et al.*, 2020) has been produced, roughly following the approach of

1
2
3 1053 Austermann *et al.* (2021). Care has been taken during its construction to allow the entire mantle and crust to be
4 viscoelastic. Through this choice, we naturally include lateral variations in lithospheric viscosity and thickness,
5 thereby permitting characteristics of the surface load changes to determine the extent of elastic versus viscous
6 deformation. This new 3D viscosity inference, along with its inferred temperature structure, is included within
7 the supplementary materials.
8
9

10 1058 We have further demonstrated how the adjoint method can be used to determine the initial sea level at t_0 ,
11 such that for any combination of Earth structure, rheology, and ice history, forward GIA simulations accurately
12 predict the observed present-day topography. In so doing, we have shown the importance of a two-step inversion
13 strategy that initially focuses on fitting long-wavelength observations in order to minimise numerical artifacts
14 due to the truncation of the underlying spherical harmonic basis functions, before adding in shorter-wavelength
15 features. This same strategy may be effective in avoiding local minima and has been employed successfully in
16 seismic tomography based on the adjoint method (e.g., Bozdağ *et al.*, 2016; Lei *et al.*, 2020; Lloyd *et al.*, 2020).
17
18 1063 Although a similar iterative approach to this problem is routine (e.g., Kendall *et al.*, 2005), our procedure allows
19 jointly inverting for the initial sea level while also updating other model parameters (e.g., mantle viscosity).
20
21

22 1067 Using 1D Earth structure, we have provided and discussed the characteristics of viscosity sensitivity kernels
23 for both absolute sea-level and relative sea-level observations that are located in near-field, forebulge, and
24 far-field settings. Through these examples, we gain intuition concerning how and what physical processes
25 are encoded within the structure of the kernel. For example, we have explored how the geometry of solid
26 Earth rebound and forebulge collapse influences sea level. We have observed how sea-level observations are
27 influenced by continental levering, by ocean siphoning and expulsion, and by coupling of the weaker viscosity
28 upper mantle with the stiffer viscosity lower mantle. We acknowledge that identification of these processes can
29 be challenging, but doing so provides deeper insight into the behavior of sea level at a particular location and
30 can improve the design of forward modeling experiments.
31
32

33 1076 Although there are many differences amongst the viscosity sensitivity kernels for observations of absolute
34 sea level and relative sea level, there are four general characteristics that are worthy of reiterating. First, kernels
35 for near-field observations have amplitudes $\sim 10\text{-}100$ greater than those that are located on the forebulge or
36 within the far field. Second, the sensitivities for near-field observations are dominated by the closest regions of
37 surface mass change. In contrast, kernels for far-field observations have similar amplitude sensitivity both locally
38 and beneath regions of major surface mass change (e.g., Laurentide ice sheet). This last point conveniently
39 demonstrates why estimates of 1D mantle viscosity based on far-field observations may be biased. Third,
40

1
2
3 far-field viscosity sensitivity kernels fall into two groups that can be differentiated based on whether the region
4 intermediate to the observation site and ice mass change is dominantly continental or oceanic in nature. For
5 the former, the structure of the kernel is more diffuse, while in the latter, a linear and higher amplitude zone
6 of sensitivity develops that is reminiscent of *banana-doughnut* kernels in seismology (Dahlen *et al.*, 2000).
7
8
9
10 Lastly, observations of absolute sea level and relative sea level are uniquely sensitive to viscosity in the deep
11 mantle and the amplitude of their 3D sensitivity kernels are non-negligible, in contrast to what is suggested by
12
13 1D sensitivity kernels (e.g., Mitrovica & Peltier, 1991; Paulson *et al.*, 2005; Wu, 2006; Crawford *et al.*, 2018).
14
15
16 Finally, in the context of relative sea-level observations, we have explored and discussed the impact of 3D
17 mantle viscosity on the structure of the viscosity sensitivity kernels. In general terms, inclusion of 3D viscosity
18 structure leads to greater complexity of the viscosity sensitivity kernel. Using examples from the Amundsen
19 Sea Embayment and Barbados, we have demonstrated that including lower viscosity regions introduces higher
20 amplitude and shorter wavelength structure into the kernel. In high-viscosity regions, the inverse is true and
21 there is a threshold above which elastic deformation dominates and the viscosity sensitivity kernel is zeroed
22 out. This latter effect leads to the greatest sensitivities being concentrated in a lower viscosity region that can
23 be quite distal to the observation site. In a forthcoming companion study, we will use the tools and intuition
24 developed herein to develop strategies for inverting synthetic paleo sea-level observations in order to recover a
25 target 3D mantle viscosity model.
26
27
28
29
30
31
32
33
34
35
36
37
38
39
40
41
42
43
44
45
46
47
48
49
50
51
52
53
54
55
56
57
58
59
60

Acknowledgments

This work has been supported by the National Science Foundation under grants: NSF-EAR-2002352 and OPP-2142592. Support was also provided through the Natural Environment Research Council grant number NE/V010433/1. We acknowledge computing resources from Columbia University's Shared Research Computing Facility project, which is supported by NIH Research Facility Improvement Grant 1G20RR030893-01, and associated funds from the New York State Empire State Development, Division of Science Technology and Innovation (NYSTAR) Contract C090171, both awarded April 15, 2010. MH acknowledges support from Geoscience Australia and the Australian Research Council's Discovery Early Career Researcher Award DE220101519. FDR acknowledges support from the Imperial College Research Fellowship scheme. Figures were created using the Generic Mapping Tools (GMT; (Wessel *et al.*, 2019)).

1110 Data availability

1111 The 3D viscosity and temperature inference based on the shear-wave speeds of GLAD-M25 (Lei *et al.*, 2020;
1112 Bozdağ *et al.*, 2016) are included with the supplementary materials.

1 2 1113 References 3 4 5

- 6 1114 Al-Attar, D. & Tromp, J., 2013. Sensitivity kernels for viscoelastic loading based on adjoint methods, *Geophys-*
7 1115 *ical Journal International*, **196**(1), 34–77.
8
9
10 1116 Andrault, D., Bolfan-Casanova, N., Nigro, G. L., Bouhifd, M. A., Garbarino, G., & Mezouar, M., 2011. Solidus
11 1117 and liquidus profiles of chondritic mantle: Implication for melting of the earth across its history, *Earth and*
12 1118 *Planetary Science Letters*, **304**(1-2), 251–259.
13
14
15
16 1119 Argus, D. F., Peltier, W. R., Drummond, R., & Moore, A. W., 2014. The antarctica component of postglacial
17 1120 rebound model ICE-6g_c (VM5a) based on GPS positioning, exposure age dating of ice thicknesses, and
18 1121 relative sea level histories, *Geophysical Journal International*, **198**(1), 537–563.
19
20
21
22 1122 Argus, D. F., Peltier, W. R., Blewitt, G., & Kreemer, C., 2021. The viscosity of the top third of the lower mantle
23 1123 estimated using GPS, GRACE, and relative sea level measurements of glacial isostatic adjustment, *Journal*
24 1124 *of Geophysical Research: Solid Earth*, **126**(5).
25
26
27
28 1125 Austermann, J., Mitrovica, J. X., Latychev, K., & Milne, G. A., 2013. Barbados-based estimate of ice volume
29 1126 at last glacial maximum affected by subducted plate, *Nature Geoscience*, **6**(7), 553–557.
30
31
32 1127 Austermann, J., Chen, C., Lau, H., Maloof, A., & Latychev, K., 2020. Constraints on mantle viscosity and
33 1128 laurentide ice sheet evolution from pluvial paleolake shorelines in the western united states, *Earth and*
34 1129 *Planetary Science Letters*, **532**, 116006.
35
36
37
38
39 1130 Austermann, J., Hoggard, M. J., Latychev, K., Richards, F. D., & Mitrovica, J. X., 2021. The effect of lateral
40 1131 variations in earth structure on last interglacial sea level, *Geophysical Journal International*, **227**(3), 1938–
41 1132 1960.
42
43
44
45 1133 Bagge, M., Klemann, V., Steinberger, B., Latinović, M., & Thomas, M., 2021. Glacial-isostatic adjustment mod-
46 1134 els using geodynamically constrained 3d earth structures, *Geochemistry, Geophysics, Geosystems*, **22**(11).
47
48
49
50 1135 Bailey, R. C., 2006. Large time step numerical modelling of the flow of maxwell materials, *Geophysical Journal*
51 1136 *International*, **164**(2), 460–466.
52
53
54 1137 Barletta, V. R., Bevis, M., Smith, B. E., Wilson, T., Brown, A., Bordoni, A., Willis, M., Khan, S. A., Rovira-
55
56 1138 Navarro, M., Dalziel, I., Smalley, R., Kendrick, E., Konfal, S., Caccamise, D. J., Aster, R. C., Nyblade, A., &

- 1
2
3 ¹¹³⁹ Wiens, D. A., 2018. Observed rapid bedrock uplift in amundsen sea embayment promotes ice-sheet stability,
4
5 ¹¹⁴⁰ *Science*, **360**(6395), 1335–1339.
6
7 ¹¹⁴¹ Bassin, C., 2000. The current limits of resolution for surface wave tomography in north america, *EOS Trans.*
8
9 ¹¹⁴² *AGU. 81 : Fall Meet. Suppl., Abstract.*
10
11
12 ¹¹⁴³ Bozdağ, E., Peter, D., Lefebvre, M., Komatitsch, D., Tromp, J., Hill, J., Podhorszki, N., & Pugmire, D., 2016.
13
14 ¹¹⁴⁴ Global adjoint tomography: first-generation model, *Geophysical Journal International*, **207**(3), 1739–1766.
15
16
17 ¹¹⁴⁵ Burridge, R., 1969. Spherically symmetric differential equations, the rotation group, and tensor spherical
18 ¹¹⁴⁶ functions, *Mathematical Proceedings of the Cambridge Philosophical Society*, **65**(1), 157–175.
19
20
21 ¹¹⁴⁷ Cammarano, F., Goes, S., Vacher, P., & Giardini, D., 2003. Inferring upper-mantle temperatures from seismic
22 ¹¹⁴⁸ velocities, *Physics of the Earth and Planetary Interiors*, **138**(3-4), 197–222.
23
24
25 ¹¹⁴⁹ Caron, L., Métivier, L., Greff-Lefftz, M., Fleitout, L., & Rouby, H., 2017. Inverting glacial isostatic adjustment
26 ¹¹⁵⁰ signal using bayesian framework and two linearly relaxing rheologies, *Geophysical Journal International*,
27
28 ¹¹⁵¹ **209**(2), 1126–1147.
29
30
31 ¹¹⁵² Cauchy, A., 1847. Méthode générale pour la résolution des systemes d'équations simultanées, *Comp. Rend. Sci.*
32
33 ¹¹⁵³ *Paris*, **25**, 536–538.
34
35
36 ¹¹⁵⁴ Chave, A. D. & Jones, A. G., 2012. *The magnetotelluric method: Theory and practice*, Cambridge University
37
38 ¹¹⁵⁵ Press.
39
40
41 ¹¹⁵⁶ Connolly, J., 2005. Computation of phase equilibria by linear programming: A tool for geodynamic modeling
42 ¹¹⁵⁷ and its application to subduction zone decarbonation, *Earth and Planetary Science Letters*, **236**(1-2), 524–
43
44 ¹¹⁵⁸ 541.
45
46
47 ¹¹⁵⁹ Connolly, J. A. D. & Khan, A., 2016. Uncertainty of mantle geophysical properties computed from phase
48 ¹¹⁶⁰ equilibrium models, *Geophysical Research Letters*, **43**(10), 5026–5034.
49
50
51 ¹¹⁶¹ Crawford, O., 2019. On the viscoelastic deformation of the earth.
52
53
54 ¹¹⁶² Crawford, O., Al-Attar, D., Tromp, J., & Mitrovica, J. X., 2016. Forward and inverse modelling of post-seismic
55 ¹¹⁶³ deformation, *Geophysical Journal International*, **208**(2), 845–876.
56
57
58
59
60

- 1
2
3 1164 Crawford, O., Al-Attar, D., Tromp, J., Mitrovica, J. X., Austermann, J., & Lau, H. C. P., 2018. Quantifying the
4 sensitivity of post-glacial sea level change to laterally varying viscosity, *Geophysical Journal International*,
5 1165 214(2), 1324–1363.
6
7 1167 Creel, R. C., Austermann, J., Khan, N. S., D'Andrea, W. J., Balascio, N., Dyer, B., Ashe, E., & Menke, W.,
8 1168 2022. Postglacial relative sea level change in norway, *Quaternary Science Reviews*, 282, 107422.
9
10 1169 Dahlen, F. A. & Tromp, J., 1999. *Theoretical Global Seismology*, Princeton University Press.
11
12 1170 Dahlen, F. A., Hung, S.-H., & Nolet, G., 2000. Fréchet kernels for finite-frequency traveltimes-i. theory,
13 1171 *Geophysical Journal International*, 141(1), 157–174.
14
15 1172 Dannberg, J., Eilon, Z., Faul, U., Gassmöller, R., Moulik, P., & Myhill, R., 2017. The importance of grain
16 size to mantle dynamics and seismological observations, *Geochemistry, Geophysics, Geosystems*, 18(8),
17 1173 3034–3061.
18
19 1175 Debayle, E., Bodin, T., Durand, S., & Ricard, Y., 2020. Seismic evidence for partial melt below tectonic plates,
20 1176 *Nature*, 586(7830), 555–559.
21
22 1177 Durek, J. J. & Ekström, G., 1996. A radial model of anelasticity consistent with long-period surface-wave
23 1178 attenuation, *Bulletin of the Seismological Society of America*, 86(1A), 144–158.
24
25 1179 Dziewonski, A. M. & Anderson, D. L., 1981. Preliminary reference earth model, *Physics of the Earth and*
26 1180 *Planetary Interiors*, 25(4), 297–356.
27
28 1181 Fichtner, A. & Trampert, J., 2011. Resolution analysis in full waveform inversion, *Geophysical Journal International*,
29 1182 187(3), 1604–1624.
30
31 1183 Fichtner, A., Bunge, H.-P., & Igel, H., 2006. The adjoint method in seismology, *Physics of the Earth and*
32 1184 *Planetary Interiors*, 157(1-2), 86–104.
33
34 1185 Forte, A. M. & Mitrovica, J. X., 1996. New inferences of mantle viscosity from joint inversion of long-wavelength
35 1186 mantle convection and post-glacial rebound data, *Geophysical Research Letters*, 23(10), 1147–1150.
36
37 1187 Gasperini, P., Yuen, D. A., & Sabadini, R., 1990. Effects of lateral viscosity variations on postglacial rebound:
38 1188 Implications for recent sea-level trends, *Geophysical Research Letters*, 17(1), 5–8.
39
40
41
42
43
44
45
46
47
48
49
50
51
52
53
54
55
56
57
58
59
60

- 1
2
3 1189 Gelfand, I. M. & Shapiro, Z. Y., 1956. Representation of the group of rotations in three-dimensional space and
4
5 1190 their application, *Am. Math. Soc. Transl.*, **2**, 207–316.
6
7
8 1191 Gomez, N., Pollard, D., & Holland, D., 2015. Sea-level feedback lowers projections of future antarctic ice-sheet
9
10 1192 mass loss, *Nature Communications*, **6**(1).
11
12 1193 Gomez, N., Latychev, K., & Pollard, D., 2018. A coupled ice sheet–sea level model incorporating 3d earth
13
14 1194 structure: Variations in antarctica during the last deglacial retreat, *Journal of Climate*, **31**(10), 4041–4054.
15
16 1195 Groh, A., Ewert, H., Scheinert, M., Fritsche, M., Rülke, A., Richter, A., Rosenau, R., & Dietrich, R., 2012.
17
18 1196 An investigation of glacial isostatic adjustment over the amundsen sea sector, west antarctica, *Global and*
19
20 1197 *Planetary Change*, **98-99**, 45–53.
21
22 1198 Han, D. & Wahr, J., 1989. Post-glacial rebound analysis for a rotating earth, in *Slow Deformation and Trans-*
23
24 1199 *mission of Stress in the Earth*, pp. 1–6, American Geophysical Union.
25
26 1200 Haskell, N. A., 1935. The motion of a viscous fluid under a surface load, *Physics*, **6**(8), 265–269.
27
28 1201 Ivins, E. R., van der Wal, W., Wiens, D. A., Lloyd, A. J., & Caron, L., 2021. Antarctic upper mantle rheology,
29
30 1202 *Geological Society, London, Memoirs*, pp. M56–2020–19.
31
32 1203 Jackson, I. & Faul, U. H., 2010. Grainsize-sensitive viscoelastic relaxation in olivine: Towards a robust
33
34 1204 laboratory-based model for seismological application, *Physics of the Earth and Planetary Interiors*, **183**(1–
35
36 1205 2), 151–163.
37
38 1206 Johnson, J. S., Bentley, M. J., & Gohl, K., 2008. First exposure ages from the amundsen sea embayment, west
39
40 1207 antarctica: The late quaternary context for recent thinning of pine island, smith, and pope glaciers, *Geology*,
41
42 1208 **36**(3), 223.
43
44 1209 Karato, S.-I., 1993. Importance of anelasticity in the interpretation of seismic tomography, *Geophysical Research*
45
46 1210 *Letters*, **20**(15), 1623–1626.
47
48 1211 Kaufmann, G., Wu, P., & Ivins, E. R., 2005. Lateral viscosity variations beneath antarctica and their implications
49
50 1212 on regional rebound motions and seismotectonics, *Journal of Geodynamics*, **39**(2), 165–181.
51
52 1213 Kendall, R. A., Mitrovica, J. X., & Milne, G. A., 2005. On post-glacial sea level - II. numerical formulation and
53
54 1214 comparative results on spherically symmetric models, *Geophysical Journal International*, **161**(3), 679–706.
55
56
57
58
59
60

- 1
2
3 1215 Khan, N. S., Horton, B. P., Engelhart, S., Rovere, A., Vacchi, M., Ashe, E. L., Törnqvist, T. E., Dutton, A.,
4
5 1216 Hijma, M. P., & Shennan, I., 2019. Inception of a global atlas of sea levels since the last glacial maximum,
6
7 1217 *Quaternary Science Reviews*, **220**, 359–371.
8
9 1218 Kim, A., Crawford, O., Al-Attar, D., Lau, H., Mitrovica, J., & Laty-
10 chev, K., 2022. Ice age effects on the satellite-derived mml:math
11 xmlns:mml="http://www.w3.org/1998/math/MathML" altimg="si1.svg" mml:msubmml:mrowmml:mover
12 accent="true" mml:mrowmml:mij/mml:mi/mml:mrowmml:mrowmml:mo-/mml:mo/mml:mrow/mml:mover/mml:mrowmml:
13 datum: Mapping the sensitivity to 3d variations in mantle viscosity, *Earth and Planetary Science Letters*,
14
15 1222
16 1223
17 581, 117372.
18
19
20 1224 Komatitsch, D. & Tromp, J., 2002. Spectral-element simulations of global seismic wave propagation-i. valida-
21
22 1225 tion, *Geophysical Journal International*, **149**(2), 390–412.
23
24
25 1226 Komatitsch, D. & Tromp, J., 2002. Spectral-element simulations of global seismic wave propagation-II. three-
26
27 1227 dimensional models, oceans, rotation and self-gravitation, *Geophysical Journal International*, **150**(1), 303–
28
29 1228 318.
30
31 1229 Kumazawa, M. & Anderson, O. L., 1969. Elastic moduli, pressure derivatives, and temperature derivatives of
32
33 1230 single-crystal olivine and single-crystal forsterite, *Journal of Geophysical Research*, **74**(25), 5961–5972.
34
35
36 1231 Kustowski, B., Ekström, G., & Dziewoński, A. M., 2008. Anisotropic shear-wave velocity structure of the earth's
37
38 1232 mantle: A global model, *Journal of Geophysical Research*, **113**(B6).
39
40 1233 Latychev, K., Mitrovica, J. X., Tromp, J., Tamisiea, M. E., Komatitsch, D., & Christara, C. C., 2005. Glacial
41
42 1234 isostatic adjustment on 3-d earth models: a finite-volume formulation, *Geophysical Journal International*,
43
44 1235 **161**(2), 421–444.
45
46
47 1236 Lau, H. C. P., Mitrovica, J. X., Austermann, J., Crawford, O., Al-Attar, D., & Latychev, K., 2016. Inferences of
48
49 1237 mantle viscosity based on ice age data sets: Radial structure, *Journal of Geophysical Research: Solid Earth*,
50
51 1238 **121**(10), 6991–7012.
52
53
54 1239 Lau, H. C. P., Mitrovica, J. X., Davis, J. L., Tromp, J., Yang, H.-Y., & Al-Attar, D., 2017. Tidal tomography
55
56 1240 constrains earth's deep-mantle buoyancy, *Nature*, **551**(7680), 321–326.
57
58
59
60

- 1
2
3 1241 Lau, H. C. P., Austermann, J., Mitrovica, J. X., Crawford, O., Al-Attar, D., & Latychev, K., 2018. Inferences of
4 mantle viscosity based on ice age data sets: The bias in radial viscosity profiles due to the neglect of laterally
5 heterogeneous viscosity structure, *Journal of Geophysical Research: Solid Earth*, **123**(9), 7237–7252.
6
7 1244 Lau, H. C. P., Holtzman, B. K., & Havlin, C., 2020. Toward a self-consistent characterization of lithospheric
8 plates using full-spectrum viscoelasticity, *AGU Advances*, **1**(4).
9
10 1246 Lei, W., Ruan, Y., Bozdağ, E., Peter, D., Lefebvre, M., Komatitsch, D., Tromp, J., Hill, J., Podhorszki, N.,
11 & Pugmire, D., 2020. Global adjoint tomography—model GLAD-m25, *Geophysical Journal International*,
12 **223**(1), 1–21.
13
14 1249 Li, T., Wu, P., Wang, H., Steffen, H., Khan, N. S., Engelhart, S. E., Vacchi, M., Shaw, T. A., Peltier, W. R.,
15 & Horton, B. P., 2020. Uncertainties of glacial isostatic adjustment model predictions in north america
16 associated with 3d structure, *Geophysical Research Letters*, **47**(10).
17
18 1252 Lloyd, A. J., Wiens, D. A., Nyblade, A. A., Anandakrishnan, S., Aster, R. C., Huerta, A. D., Wilson, T. J.,
19 Dalziel, I. W. D., Shore, P. J., & Zhao, D., 2015. A seismic transect across west antarctica: Evidence for
20 mantle thermal anomalies beneath the bentley subglacial trench and the marie byrd land dome, *Journal of
21 Geophysical Research: Solid Earth*, **120**(12), 8439–8460.
22
23 1256 Lloyd, A. J., Wiens, D. A., Zhu, H., Tromp, J., Nyblade, A. A., Aster, R. C., Hansen, S. E., Dalziel, I. W. D.,
24 Wilson, T., Ivins, E. R., & O'Donnell, J. P., 2020. Seismic structure of the antarctic upper mantle imaged
25 with adjoint tomography, *Journal of Geophysical Research: Solid Earth*, **125**(3).
26
27 1259 Lloyd, A. J., Crawford, O., Al-Attar, D., Austermann, J., Creel, R., & et al., in prep. Gia imaging of 3d mantle
28 viscosity based on paleo sea-level observations - part 2: Inversion proof of concept, *Geophysical Journal
29 International*.
30
31 1262 Lucas, E. M., Soto, D., Nyblade, A. A., Lloyd, A. J., Aster, R. C., Wiens, D. A., O'Donnell, J. P., Stuart, G. W.,
32 Wilson, T. J., Dalziel, I. W., Winberry, J. P., & Huerta, A. D., 2020. P- and s-wave velocity structure of central
33 west antarctica: Implications for the tectonic evolution of the west antarctic rift system, *Earth and Planetary
34 Science Letters*, **546**, 116437.
35
36 1266 Martinec, Z., 2000. Spectral-finite element approach to three-dimensional viscoelastic relaxation in a spherical
37 earth, *Geophysical Journal International*, **142**(1), 117–141.
38
39
40
41
42
43
44
45
46
47
48
49
50
51
52
53
54
55
56
57
58
59
60

- 1
2
3 1268 Martinec, Z., Klemann, V., van der Wal, W., Riva, R. E. M., Spada, G., Sun, Y., Melini, D., Kachuck, S. B.,
4
5 1269 Barletta, V., Simon, K., A, G., & James, T. S., 2018. A benchmark study of numerical implementations of
6
7 1270 the sea level equation in GIA modelling, *Geophysical Journal International*, **215**(1), 389–414.
8
9 1271 Milne, G. A. & Mitrovica, J. X., 1998. Postglacial sea-level change on a rotating earth, *Geophysical Journal*
10
11 1272 *International*, **133**(1), 1–19.
12
13 1273 Mitrovica, J. & Forte, A., 2004. A new inference of mantle viscosity based upon joint inversion of convection
14
15 1274 and glacial isostatic adjustment data, *Earth and Planetary Science Letters*, **225**(1-2), 177–189.
16
17 1275 Mitrovica, J. X., 1996. Haskell [1935] revisited, *Journal of Geophysical Research: Solid Earth*, **101**(B1),
18
19 1276 555–569.
20
21
22 1277 Mitrovica, J. X. & Milne, G. A., 2003. On post-glacial sea level: I. general theory, *Geophysical Journal*
23
24 1278 *International*, **154**(2), 253–267.
25
26
27 1279 Mitrovica, J. X. & Peltier, W. R., 1991. Radial resolution in the inference of mantle viscosity from observations
28
29 1280 of glacial isostatic adjustment, in *Glacial Isostasy, Sea-Level and Mantle Rheology*, pp. 63–78, Springer
30
31 1281 Netherlands.
32
33 1282 Mitrovica, J. X. & Peltier, W. R., 1993. Present-day secular variations in the zonal harmonics of earth's
34
35 1283 geopotential, *Journal of Geophysical Research: Solid Earth*, **98**(B3), 4509–4526.
36
37 1284 Nakada, M. & ichiro Karato, S., 2012. Low viscosity of the bottom of the earth's mantle inferred from the
38
39 1285 analysis of chandler wobble and tidal deformation, *Physics of the Earth and Planetary Interiors*, **192**–**193**,
40
41 1286 68–80.
42
43 1287 Nakada, M. & Lambeck, K., 1989. Late pleistocene and holocene sea-level change in the australian region and
44
45 1288 mantle rheology, *Geophysical Journal International*, **96**(3), 497–517.
46
47 1289 Nield, G. A., Barletta, V. R., Bordoni, A., King, M. A., Whitehouse, P. L., Clarke, P. J., Domack, E., Scambos,
48
49 1290 T. A., & Berthier, E., 2014. Rapid bedrock uplift in the antarctic peninsula explained by viscoelastic response
50
51 1291 to recent ice unloading, *Earth and Planetary Science Letters*, **397**, 32–41.
52
53 1292 Nield, G. A., Whitehouse, P. L., King, M. A., & Clarke, P. J., 2016. Glacial isostatic adjustment in response
54
55 1293 to changing late holocene behaviour of ice streams on the siple coast, west antarctica, *Geophysical Journal*
56
57 1294 *International*, **205**(1), 1–21.
58
59
60

- 1
2
3 1295 Nolet, G., 2008. *A Breviary of Seismic Tomography*, Cambridge University Press.
4
5 1296 Pan, L., Powell, E. M., Latychev, K., Mitrovica, J. X., Creveling, J. R., Gomez, N., Hoggard, M. J., & Clark,
6 1297 P. U., 2021. Rapid postglacial rebound amplifies global sea level rise following west antarctic ice sheet
7 1298 collapse, *Science Advances*, **7**(18), eabf7787.
8
9
10
11
12 1299 Paulson, A., Zhong, S., & Wahr, J., 2005. Modelling post-glacial rebound with lateral viscosity variations,
13
14 1300 *Geophysical Journal International*, **163**(1), 357–371.
15
16
17 1301 Peltier, W. R., Argus, D. F., & Drummond, R., 2015. Space geodesy constrains ice age terminal deglaciation:
18 1302 The global ICE-6g_c (VM5a) model, *Journal of Geophysical Research: Solid Earth*, **120**(1), 450–487.
19
20
21 1303 Polak, E. & Ribiere, G., 1969. Note sur la convergence de méthodes de directions conjuguées, *ESAIM:*
22 1304 *Mathematical Modelling and Numerical Analysis-Modélisation Mathématique et Analyse Numérique*, **3**(R1),
23
24 1305 35–43.
25
26
27 1306 Pollitz, F. F., 2001. Mantle flow beneath a continental strike-slip fault: Postseismic deformation after the 1999
28 1307 hector mine earthquake, *Science*, **293**(5536), 1814–1818.
29
30
31 1308 Powell, M. J. D., 1964. An efficient method for finding the minimum of a function of several variables without
32 1309 calculating derivatives, *The Computer Journal*, **7**(2), 155–162.
33
34
35 1310 Press, W. H., Flannery, B. P., Teukolsky, S. A., & Vetterling, W., 1986. *Numerical Recipes*, Cambridge University
36
37 1311 Press.
38
39
40 1312 Priestley, K. & McKenzie, D., 2006. The thermal structure of the lithosphere from shear wave velocities, *Earth*
41
42 1313 *and Planetary Science Letters*, **244**(1-2), 285–301.
43
44
45 1314 Priestley, K. & McKenzie, D., 2013. The relationship between shear wave velocity, temperature, attenuation
46 1315 and viscosity in the shallow part of the mantle, *Earth and Planetary Science Letters*, **381**, 78–91.
47
48
49 1316 Richards, F. D., Hoggard, M. J., Cowton, L. R., & White, N. J., 2018. Reassessing the thermal structure of
50
51 1317 oceanic lithosphere with revised global inventories of basement depths and heat flow measurements, *Journal*
52
53 1318 *of Geophysical Research: Solid Earth*, **123**(10), 9136–9161.
54
55
56 1319 Richards, F. D., Hoggard, M. J., White, N., & Ghelichkhan, S., 2020. Quantifying the relationship between
57
58
59
60

- 1
2
3 1320 short-wavelength dynamic topography and thermomechanical structure of the upper mantle using calibrated
4 1321 parameterization of anelasticity, *Journal of Geophysical Research: Solid Earth*, **125**(9).
- 5
6 1322 Russo, R. M., Luo, H., Wang, K., Ambrosius, B., Mocanu, V., He, J., James, T., Bevis, M., & Fernandes, R., 2022.
7 1323 Lateral variation in slab window viscosity inferred from global navigation satellite system (GNSS)–observed
8 1324 uplift due to recent mass loss at patagonia ice fields, *Geology*, **50**(1), 111–115.
- 9
10 1325 Schaeffer, A. J. & Lebedev, S., 2013. Global shear speed structure of the upper mantle and transition zone,
11 1326 *Geophysical Journal International*, **194**(1), 417–449.
- 12
13 1327 Schuberth, B. S. A., Bunge, H.-P., Steinle-Neumann, G., Moder, C., & Oeser, J., 2009. Thermal versus elastic
14 1328 heterogeneity in high-resolution mantle circulation models with pyrolite composition: High plume excess
15 1329 temperatures in the lowermost mantle, *Geochemistry, Geophysics, Geosystems*, **10**(1), n/a–n/a.
- 16
17 1330 Schutt, D. L. & Lesher, C. E., 2006. Effects of melt depletion on the density and seismic velocity of garnet and
18 1331 spinel lherzolite, *Journal of Geophysical Research: Solid Earth*, **111**(B5), n/a–n/a.
- 19
20 1332 Shorttle, O., Maclennan, J., & Lambart, S., 2014. Quantifying lithological variability in the mantle, *Earth and*
21 1333 *Planetary Science Letters*, **395**, 24–40.
- 22
23 1334 Sjöberg, L. E. & Bagherbandi, M., 2017. *Gravity Inversion and Integration*, Springer International Publishing.
- 24
25 1335 Steinberger, B. & Calderwood, A. R., 2006. Models of large-scale viscous flow in the earth's mantle with
26 1336 constraints from mineral physics and surface observations, *Geophysical Journal International*, **167**(3), 1461–
27 1337 1481.
- 28
29 1338 Stixrude, L. & Lithgow-Bertelloni, C., 2011. Thermodynamics of mantle minerals - II. phase equilibria,
30 1339 *Geophysical Journal International*, **184**(3), 1180–1213.
- 31
32 1340 Takei, Y., Karasawa, F., & Yamauchi, H., 2014. Temperature, grain size, and chemical controls on polycrystal
33 1341 anelasticity over a broad frequency range extending into the seismic range, *Journal of Geophysical Research:*
34 1342 *Solid Earth*, **119**(7), 5414–5443.
- 35
36 1343 Tape, C., Liu, Q., & Tromp, J., 2007. Finite-frequency tomography using adjoint methods-methodology and
37 1344 examples using membrane surface waves, *Geophysical Journal International*, **168**(3), 1105–1129.
- 38
39 1345 Tikhonov, A., 1950. On determining electrical characteristics of the deep layers of the earth's crust, Citeseer.

- 1
2
3 ¹³⁴⁶ Tromp, J., 2019. Seismic wavefield imaging of earth's interior across scales, *Nature Reviews Earth & Environ-*
4 ¹³⁴⁷ *ment*, **1**(1), 40–53.
5
6
7 ¹³⁴⁸ Tromp, J. & Mitrovica, J. X., 2000. Surface loading of a viscoelastic planet—III. aspherical models, *Geophysical*
8 ¹³⁴⁹ *Journal International*, **140**(2), 425–441.
9
10
11 ¹³⁵⁰ Tromp, J., Tape, C., & Liu, Q., 2004. Seismic tomography, adjoint methods, time reversal and banana-doughnut
12 ¹³⁵¹ kernels, *Geophysical Journal International*, **160**(1), 195–216.
13
14
15
16 ¹³⁵² van der Wal, W., Whitehouse, P. L., & Schrama, E. J., 2015. Effect of GIA models with 3d composite mantle
17 ¹³⁵³ viscosity on GRACE mass balance estimates for antarctica, *Earth and Planetary Science Letters*, **414**, 134–
18
19 ¹³⁵⁴ 143.
20
21
22 ¹³⁵⁵ Wessel, P., Luis, J. F., Uieda, L., Scharroo, R., Wobbe, F., Smith, W. H. F., & Tian, D., 2019. The generic
23 ¹³⁵⁶ mapping tools version 6, *Geochemistry, Geophysics, Geosystems*, **20**(11), 5556–5564.
24
25
26 ¹³⁵⁷ Whitehouse, P. L., 2018. Glacial isostatic adjustment modelling: historical perspectives, recent advances, and
27 ¹³⁵⁸ future directions, *Earth Surface Dynamics*, **6**(2), 401–429.
28
29
30
31 ¹³⁵⁹ Whitehouse, P. L., Gomez, N., King, M. A., & Wiens, D. A., 2019. Solid earth change and the evolution of the
32 ¹³⁶⁰ antarctic ice sheet, *Nature Communications*, **10**(1).
33
34
35 ¹³⁶¹ Wu, P., 2006. Sensitivity of relative sea levels and crustal velocities in laurentide to radial and lateral viscosity
36 ¹³⁶² variations in the mantle, *Geophysical Journal International*, **165**(2), 401–413.
37
38
39
40 ¹³⁶³ Yamauchi, H. & Takei, Y., 2016. Polycrystal anelasticity at near-solidus temperatures, *Journal of Geophysical*
41 ¹³⁶⁴ *Research: Solid Earth*, **121**(11), 7790–7820.
42
43
44 ¹³⁶⁵ Zhu, H., Bozdağ, E., & Tromp, J., 2015. Seismic structure of the european upper mantle based on adjoint
45 ¹³⁶⁶ tomography, *Geophysical Journal International*, **201**(1), 18–52.
46
47
48
49
50
51
52
53
54
55
56
57
58
59
60

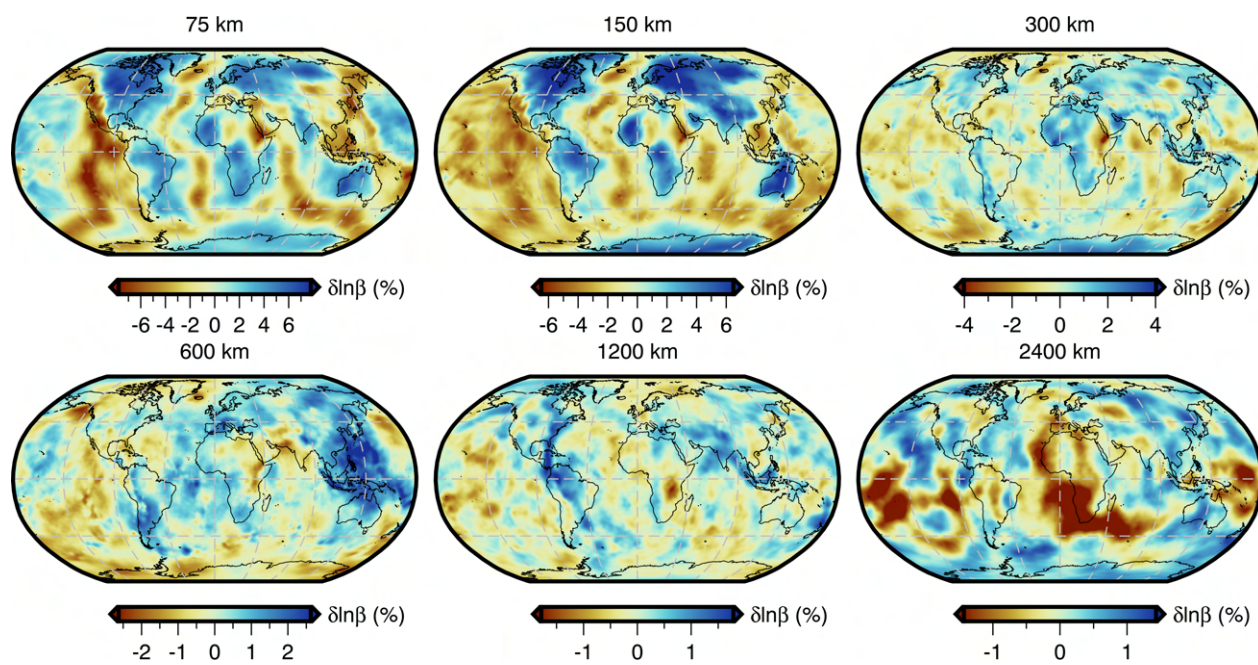
Supplementary Material – GIA imaging of 3D mantle viscosity based on paleo sea-level observations - Part I: Sensitivity kernels for an Earth with laterally varying viscosity

Andrew J. Lloyd^{*,1}, Ophelia Crawford², David Al-Attar², Jacqueline Austermann¹, Mark J. Hoggard³,
Fred D. Richards⁴, Frank Syvret²

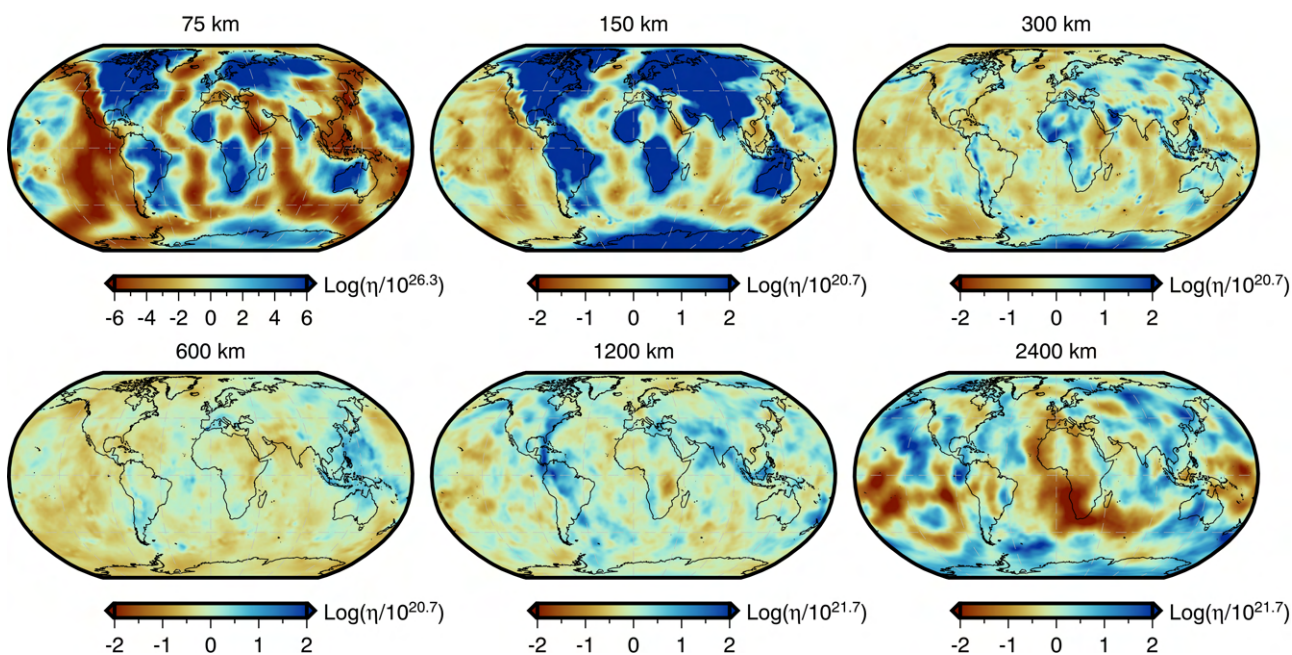
1. Lamont Doherty Earth Observatory, Columbia University, Palisades, NY 10964, USA.
2. Bullard Laboratories, Department of Earth Sciences, University of Cambridge, Madingley Road, Cambridge CB3 0EZ, UK.
3. Research School of Earth Sciences, Australia National University, Acton, ACT 0200, Australia.
4. Department of Earth Science and Engineering, Imperial College London, London SW7 2AZ, UK.

*andrewl@ldeo.columbia.edu

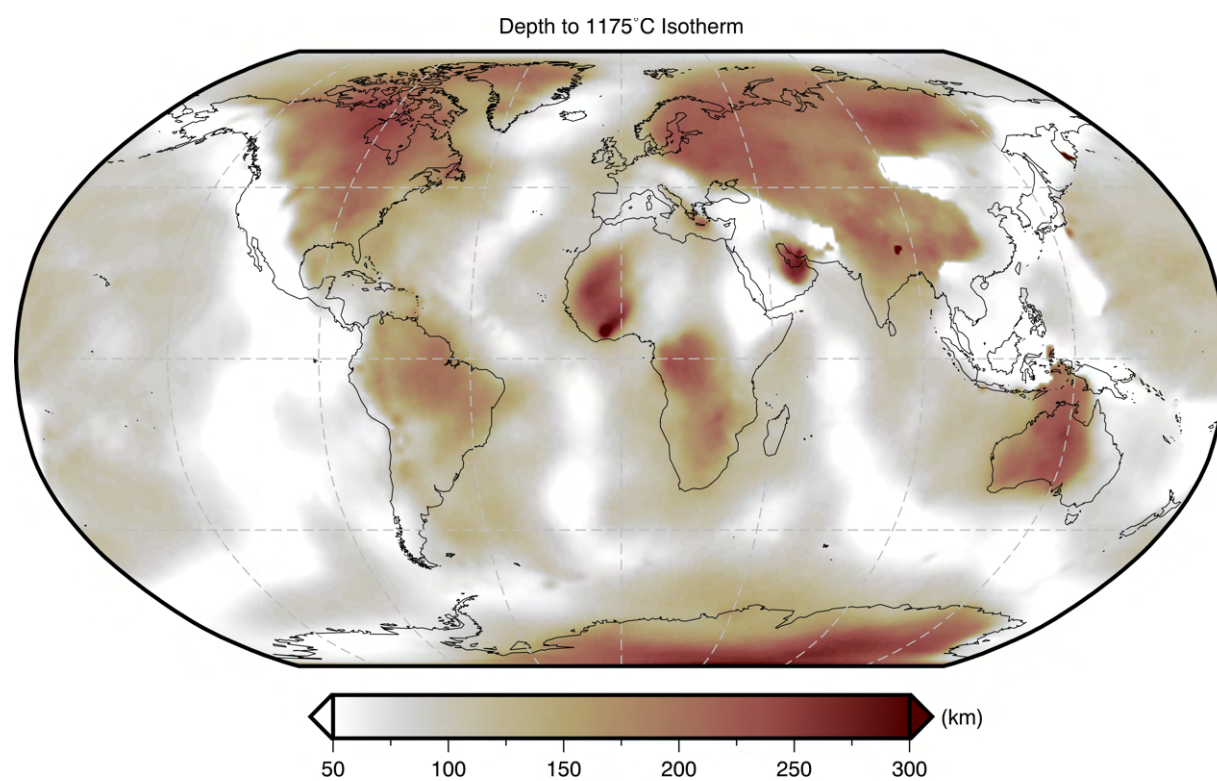
1 2 3 3D Viscosity Inference 4 5



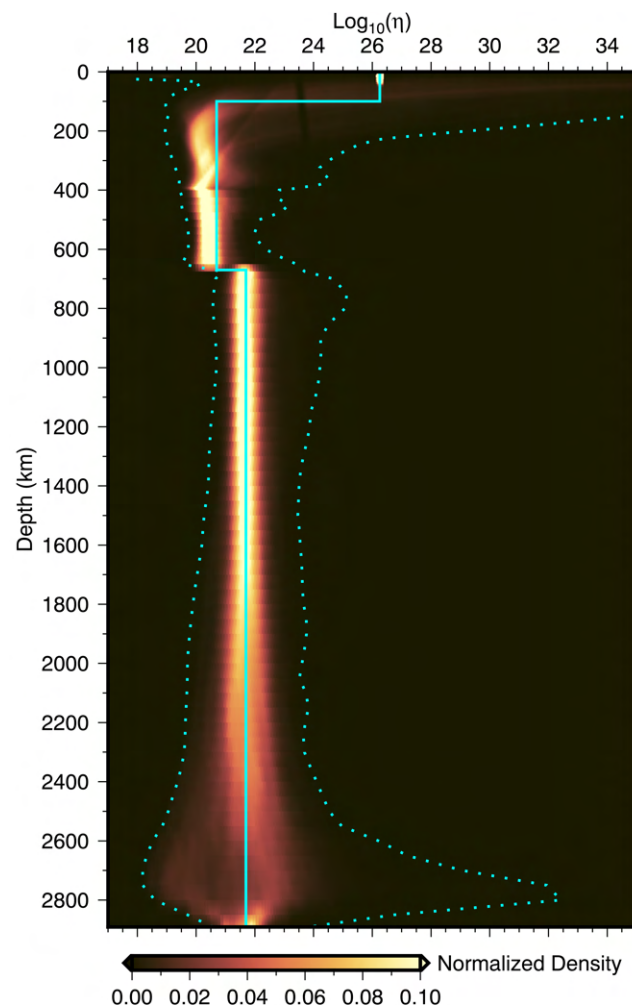
27 Supp. Figure S1: **Voigt average shear-wave speeds from GLAD-M25.** Depth slices through the Voigt average
28 shear-wave speed anomalies of GLAD-M25 (Bozdağ *et al.*, 2016; Lei *et al.*, 2020). Wave speed anomalies are
29 plotted 1D radial average of GLAD-M25.
30



Supp. Figure S2: **Inferred viscosity structure based on GLAD-M25.** Depth slices of the 3D viscosity model inferred from the shear-wave speeds structure of GLAD-M25 (Supp. Figure S1; Bozdağ *et al.*, 2016; Lei *et al.*, 2020). Viscosity anomalies are relative to the 1D radial viscosity model discussed in Section 3.5 and shown in Supp. Figure S4.

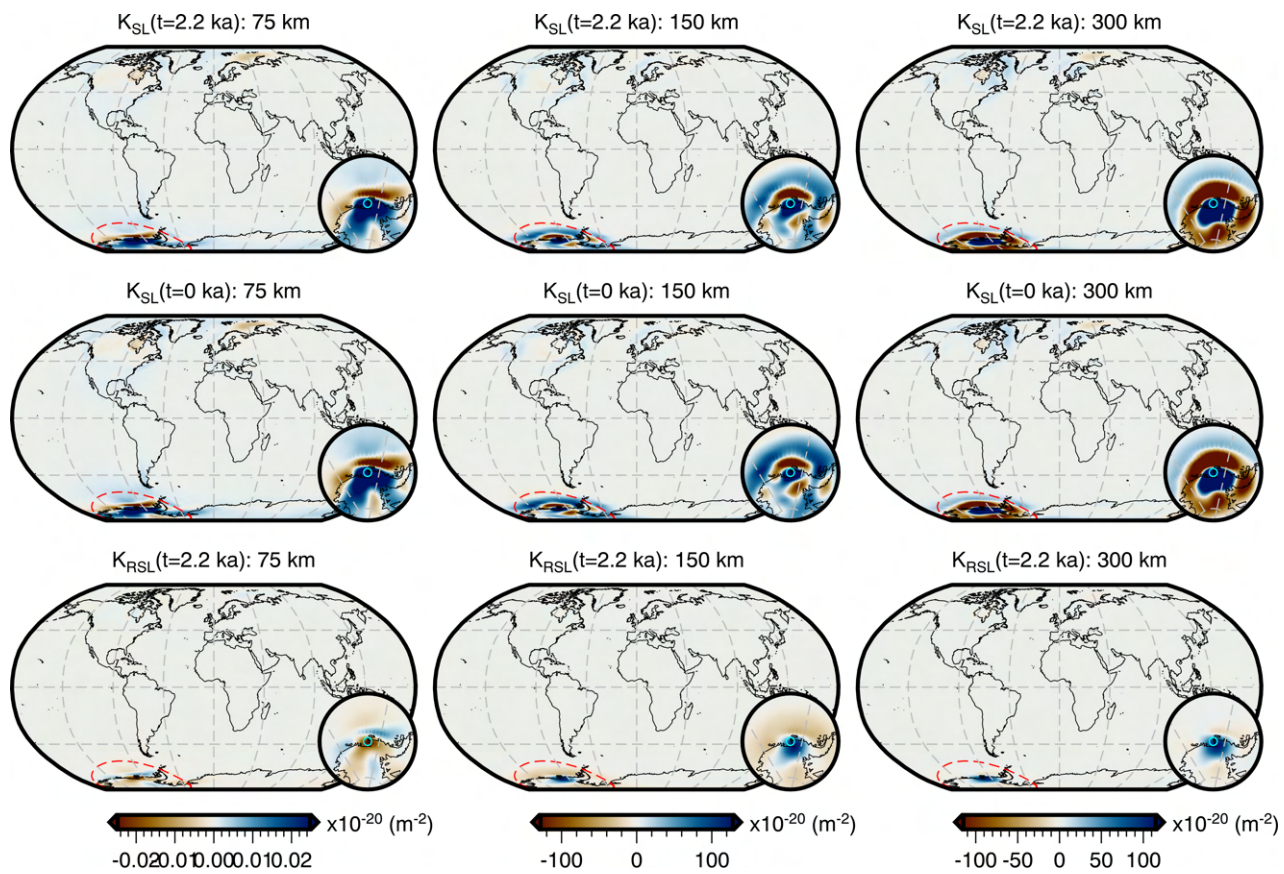


Supp. Figure S3: **Depth to the 1175°C isotherm.** Map showing the depth to the 1175°C isotherm in the intermediate temperature inference based on the shear-wave speeds of GLAD-M25 (Bozdağ *et al.*, 2016; Lei *et al.*, 2020). The 3D temperature inference is provided in the supplementary materials.

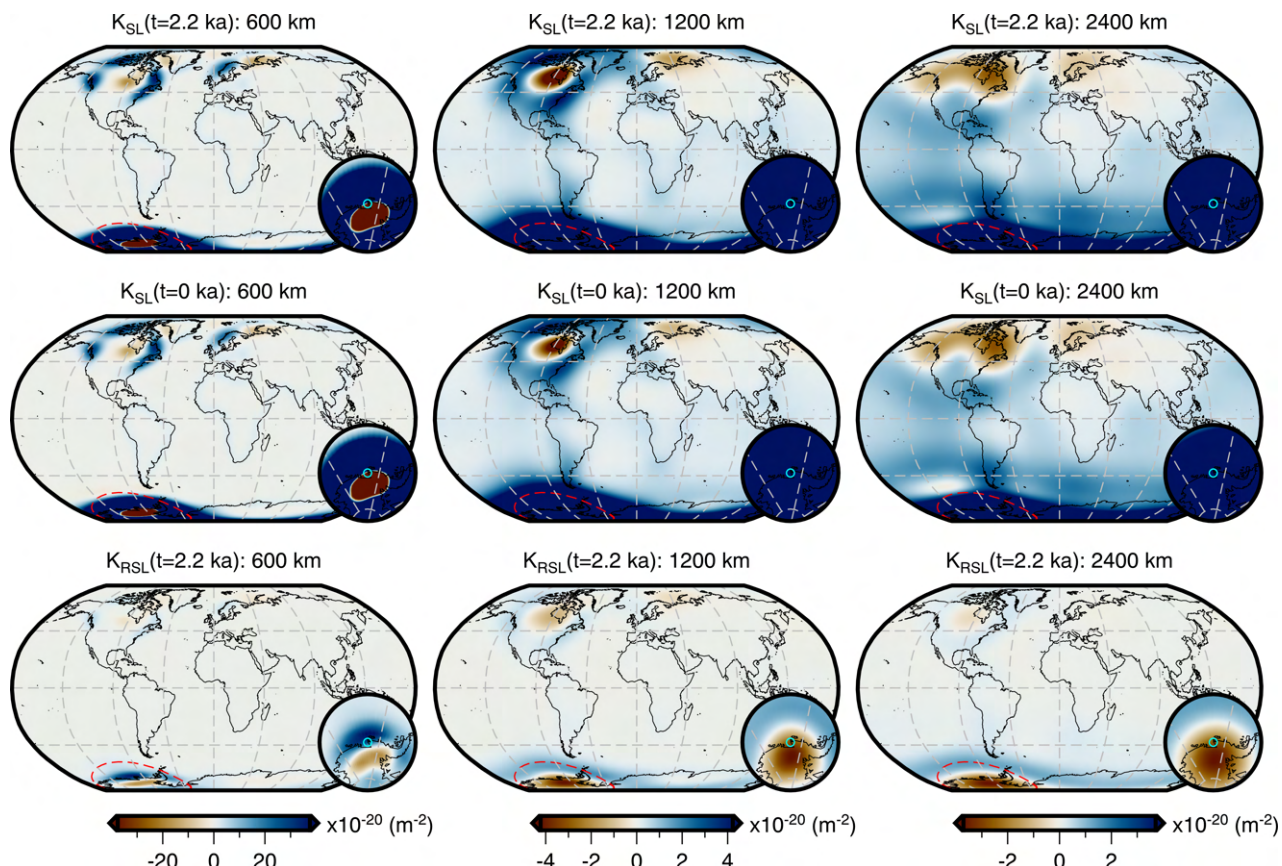


Supp. Figure S4: **Distribution of the inferred 3D viscosity structure and a comparison with our 1D Viscosity model.** Plot of our 1D radial viscosity model (cyan line), which from the surface to the core mantle boundary has viscosities of $\sim 1.8 \times 10^{26}$, 5×10^{20} , and 5×10^{21} Pa·s with discontinuities at 100 and 670 km depth. In the background is a globally normalized 2D density heatmap of the inferred 3D viscosity structure (Supp. Figure S2). When computing the normalized density for each spherical shell, each viscosity element is weighted by the sin of its co-latitude in order to account for the change in element density along each line of latitude. In addition, the cyan dotted line indicates the minimum and maximum of the 3D viscosity model as a function of depth.

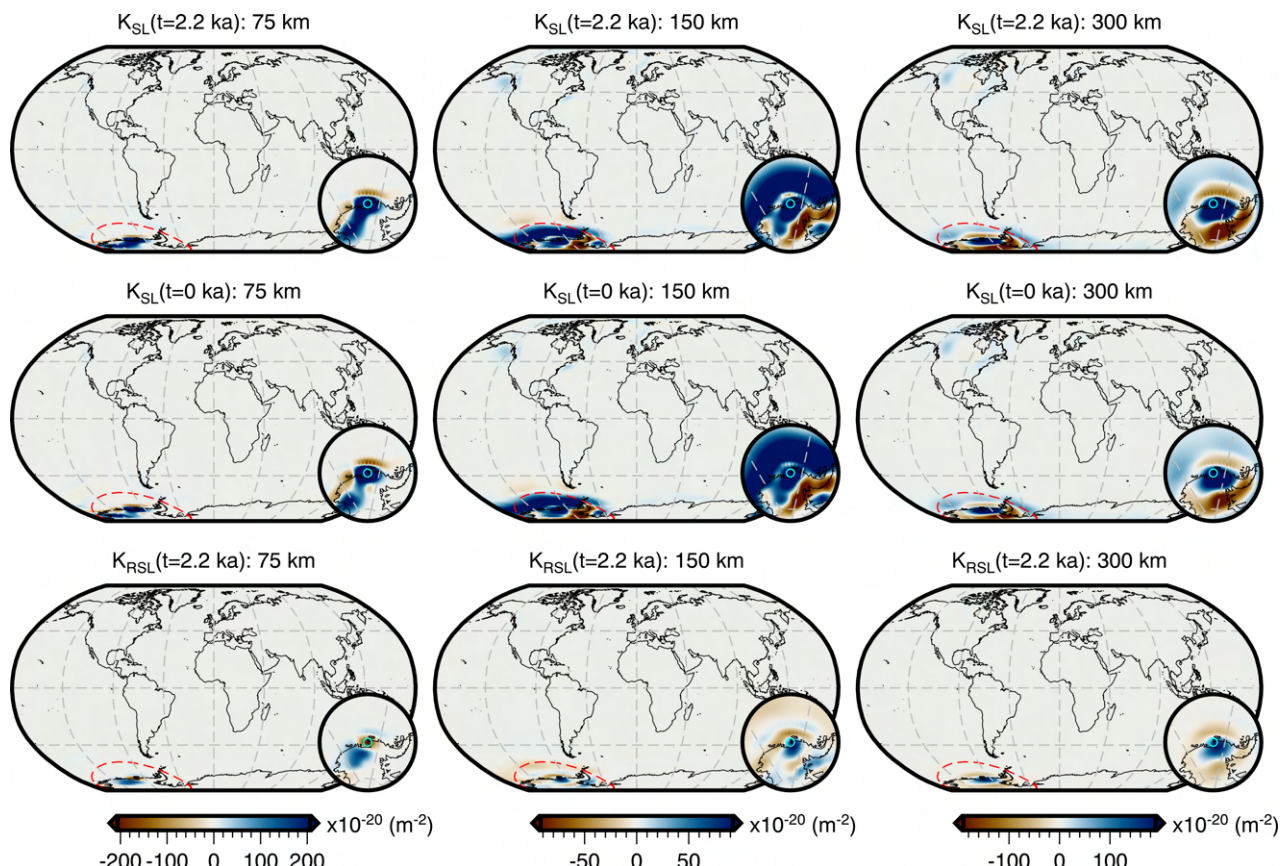
1
2 **Viscosity Sensitivity Kernels**
3
4
5



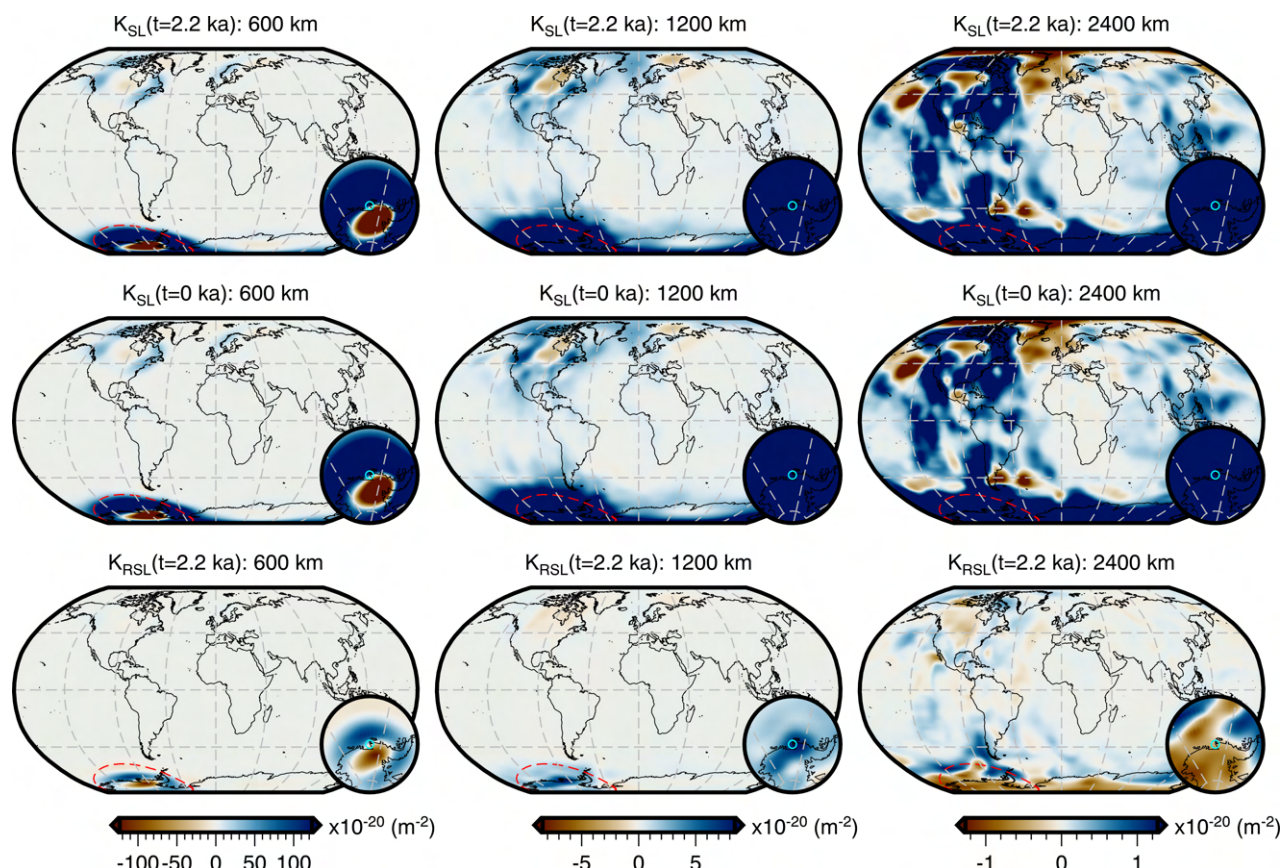
Supp. Figure S5: **Comparison of viscosity sensitivity kernels for sea-level and relative sea-level observations in the Amundsen Sea Embayment for a 1D viscosity structure.** Slices at 75, 150, and 300 km depth through the viscosity sensitivity kernels for (top row) a sea-level observation at 10 ka, (middle row) a sea-level observation at 0 ka, and (bottom row) a relative sea-level measurement at 10 ka. The inset map, centered on the observation site (cyan circle), has a width of 30° and its extent is shown by the red dashed line the main map. The color scale for each column is chosen to symmetrically span the full range of relative sea-level viscosity sensitivity kernel and thus, regions of the sea-level sensitivity kernels may be saturated.



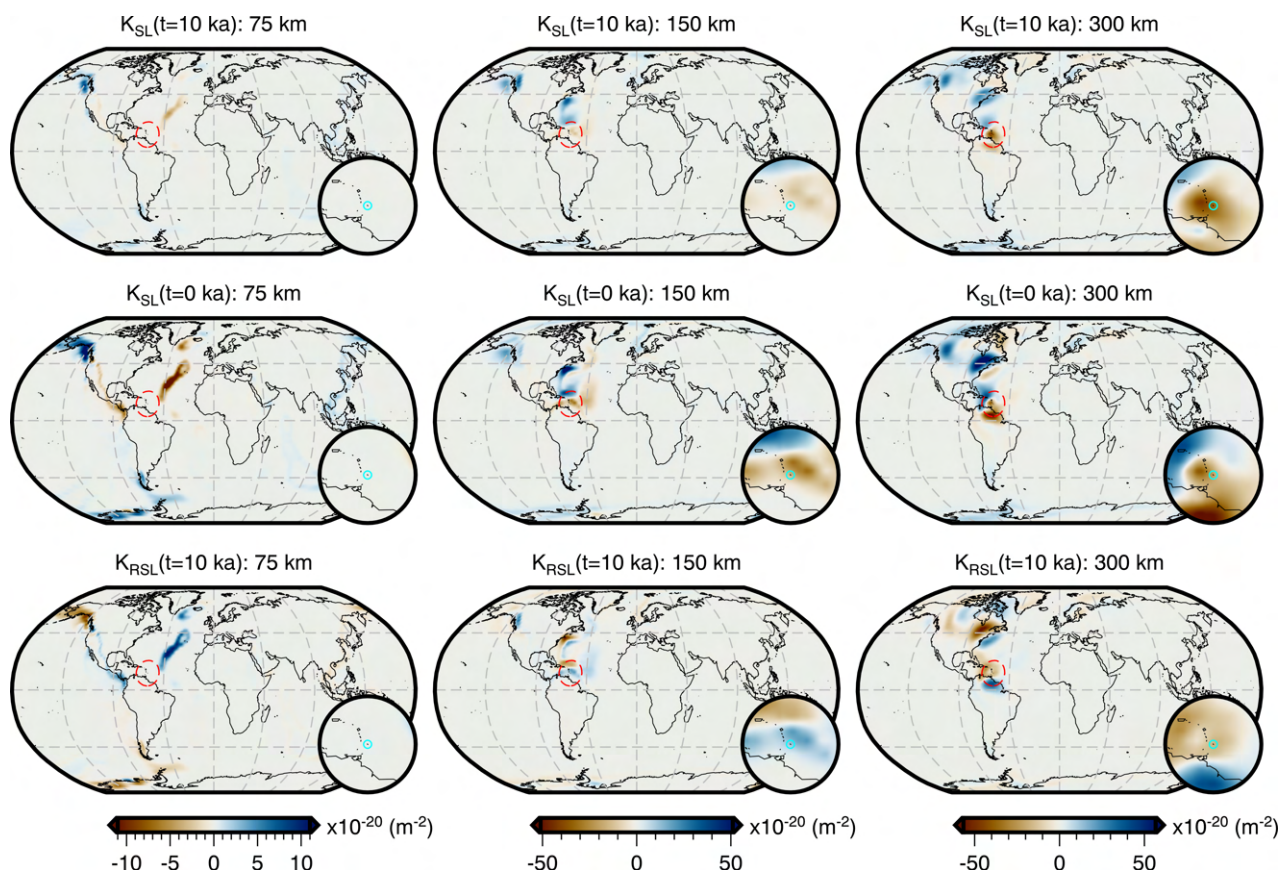
Supp. Figure S6: **Comparison of viscosity sensitivity kernels for sea-level and relative sea-level observations in the Amundsen Sea Embayment for a 1D viscosity structure.** Panels are the same as Figure S5, but for slices at 600, 1200, and 2400 km depth.



Supp. Figure S7: **Comparison of viscosity sensitivity kernels for sea-level and relative sea-level observations in the Amundsen Sea Embayment for a 3D viscosity structure.** Panels are the same as Figure S5, but now we have used our filtered and truncated 3D viscosity inference (Figure 2).

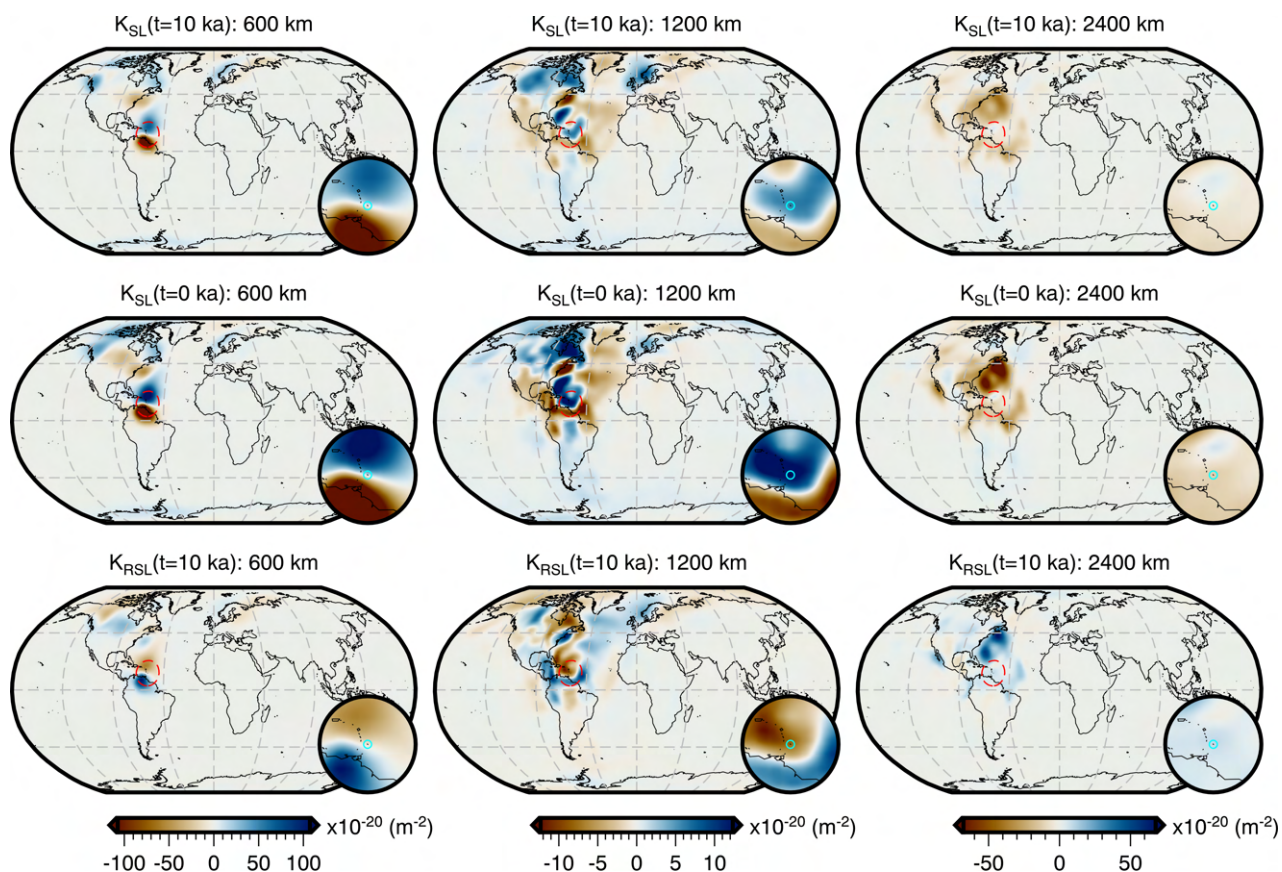
Geophysical Journal International draft from 26th October 2022

Supp. Figure S8: **Comparison of viscosity sensitivity kernels for sea-level and relative sea-level observations in the Amundsen Sea Embayment for a 3D viscosity structure.** Panels are the same as Figure S7, but for slices at 600, 1200, and 2400 km depth.



Supp. Figure S9: **Comparison of viscosity sensitivity kernels for sea-level and relative sea-level observations at Barbados for a 3D viscosity structure.** Panels are the same as Figure S5, but now we have used our filtered and truncated 3D viscosity inference (Figure 2) and the width of inset map is 20° .

Geophysical Journal International draft from 26th October 2022



Supp. Figure S10: **Comparison of viscosity sensitivity kernels for sea-level and relative sea-level observations at Barbados for a 3D viscosity structure.** Panels are the same as Figure S7, but for slices at 600, 1200, and 2400 km depth.

- 1
2
3 **References**
4
5 ⁴ Bozdağ, E., Peter, D., Lefebvre, M., Komatitsch, D., Tromp, J., Hill, J., Podhorszki, N., & Pugmire, D., 2016.
6 Global adjoint tomography: first-generation model, *Geophysical Journal International*, **207**(3), 1739–1766.
7
8 ⁶ Lei, W., Ruan, Y., Bozdağ, E., Peter, D., Lefebvre, M., Komatitsch, D., Tromp, J., Hill, J., Podhorszki, N.,
9 & Pugmire, D., 2020. Global adjoint tomography—model GLAD-m25, *Geophysical Journal International*,
10 **223**(1), 1–21.
11
12
13
14
15
16
17
18
19
20
21
22
23
24
25
26
27
28
29
30
31
32
33
34
35
36
37
38
39
40
41
42
43
44
45
46
47
48
49
50
51
52
53
54
55
56
57
58
59
60